Iron Production by Molten Sulfide Electrolysis

by

Kimaya P. Suryarao

B. Tech Metallurgical and Materials Engineering

National Institute of Technology, Tiruchirappalli, 2022

Submitted to the Department of Materials Science and Engineering in Partial Fulfillment of the Requirements for the Degree of

Master of Science in Materials Science and Engineering

at the

Massachusetts Institute of Technology

May 2024

©2024 Kimaya P. Suryarao. All Rights Reserved.
The author hereby grants to MIT a nonexclusive, worldwide, irrevocable, royalty-free license to exercise any and all rights under copyright, including to reproduce, preserve, distribute and publicly display copies of the thesis, or release the thesis under an open-access license.

Authored by:	Kimaya P. Suryarao Department of Materials Science and Engineering 9 May 2024
Certified by:	Antoine Allanore Professor of Metallurgy, Thesis Supervisor
Accepted by:	Robert J. Macfarlane Professor of Materials Science and Engineering Chair, Departmental Committee on Graduate Studies

Iron Production by Molten Sulfide Electrolysis

by

Kimaya P. Suryarao

Submitted to the Department of Materials Science and Engineering on May 9, 2024,
in Partial Fulfillment of the Requirements for the Degree of
Master of Science in Materials Science and Engineering

Abstract

With greater urgency to combat the detrimental effects of global warming, industries globally have pledged to reach net zero carbon emissions or become carbon neutral by 2050, the iron and steel industry included. With exponential increase in the production and the demand of steel, the carbon footprint of the industry has also been rising at a high rate, accounting ~ 10 -11% of the global carbon emissions. Present state-of-art steel production technologies have not been environmentally benign due to their inextricable dependence on carbon, making complete elimination of GHG emissions challenging. As renewable energy becomes a reality for industrial usage, efforts to decarbonize steel manufacturing motivate a key need to search for technologies solely using electricity for iron ore reduction. Herein, the electrolytic production of molten iron using a novel sulfide route, molten sulfide electrolysis (MSE) is investigated. Experimental evidence for electrolysis and the key attributes and underlying thermodynamics of MSE for iron production are investigated and discussed, along with sulfidation; the feedstock preparation step for the MSE process.

Thesis Supervisor: Antoine Allanore
Title: Professor of Metallurgy

Acknowledgements

"None of us got to where we are alone. The least one can do to acknowledge that support is say Thank you!"

I have been extremely fortunate to have been gifted with such incredible people in this journey of mine. First of all, I would like to thank my parents for their unwavering support throughout. Though, thank you is a very small word to acknowledge the myriad of efforts my mom (Mrs. Minal P. Suryarao) has taken for me, I would like to take this opportunity to imprint it on one of the most impactful works I have done till date. A very big thank you to my dad for being an ever-inspirational figure and for introducing me to the world of metals, in a way that I genuinely feel the urge to contribute to this industry that has given us our everything. And thank you to my little brother for being my youngest mentor!

Finding the right mentor is not something everyone is fortunate to have. I was. I am profoundly grateful to my advisor, Prof. Antoine Allanore for providing me with this amazing opportunity to work as a part of the Allanore group and for all his guidance and support in patiently nurturing and molding the researcher in me.

A very big thank you to all former and present members of the Allanore group, Caspar, Charles, Ethan, Katie, Gen, Ava, Nathan, Zach and Jonathan, for creating a fun learning atmosphere within the group. Right from training me on every single equipment in lab, to introducing me to the sulfur chemistry and literally melting rocks, to the numerous scientific discussions and our impromptu visits to pick up 'Oh, that's useful for the lab' stuff from the hallways, I cannot thank you enough for the incredible experience you have given me.

And a final thank you to my best buddies in town: Sahana, Anish for sharing the fun of countless highs and lows as experimental researchers and Rachit, Vallabh, Anant and Akash for being my all-time stressbusters. Thank you to all my other friends for gifting me this fun-filled experience at MIT.

Table of Contents

List of abbreviations and symbols

MSE	*Molten Sulfide Electrolysis*
MOE	*Molten Oxide Electrolysis*
BF-BOF	*Blast Furnace – Basic Oxygen Furnace*
EAF	*Electric Arc Furnace*
DRI	*Direct Reduced Iron*
GHG	*Green-house gases*
XRD	*X-Ray Diffraction*
SEM	*Scanning Electron Microscopy*
EDS	*Energy - Dispersive X-Ray Spectroscopy*
WDS	*Wavelength - Dispersive X-Ray Spectroscopy*
ICP – MS	*Inductively Coupled Plasma – Mass Spectroscopy*
LECO	*Light Element Carbon/Oxygen*
TIF	*Thermal Imaging Furnace*
EDM	*Electrical Discharge Machining*
CO_2	*Carbon Dioxide*
OD	*Outer Diameter*
ID	*Inner Diameter*

Fig.	*Figure*
rpm	*Revolutions per minute*
CI	*Cast iron*
Fe	*Iron*
W	*Tungsten*
Re	*Rhenium*
Xe	*Xenon*
Ar	*Argon*
Cu	*Copper*
Ba	*Barium*
La	*Lanthanum*
S	*Sulfur*
S_2	*Sulfur gas*
Mo	*Molybdenum*
Ti	*Titanium*
BaS	*Barium sulfide*
La_2S_3	*Lanthanum sulfide*
FeS	*Iron (II) sulfide*
$CuFeS_2$	*Chalcopyrite*
Fe_2O_3	*Iron (III) oxide*

ΔH^o	*Change in Standard state Enthalpy*
ΔG^o	*Change in Standard Gibbs Energy*
ΔH_{mix}	*Change in the Enthalpy of mixing*
ΔG_{mix}	*Change in the Gibbs energy of mixing*
ΔH_{rxn}	*Change in the Enthalpy of reaction*
ΔG_{rxn}	*Change in the Gibbs energy of reaction*
U_{cell}	*Cell Potential/ Cell Voltage*
U_{ohm}	*Voltage due to Ohmic contribution*
U_{chem}	*Potential/Voltage due to chemical work contribution*
$U_{over\ voltage}$	*Contribution due to over potential*
S^o	*Standard state Entropy*
T_o	*Temperature*
C^P	*Specific heat capacity at constant pressure*
F	*Faraday's Constant*
M_xY_z	*Representative of a compound; M and Y representing metal and non-metal*
mm	*Millimeters*
cm	*Centimeters*
''	*Inches*
C	*Coulombs*
mA	*Milli Amperes*
A/cm^2	*Amperes per centimeter square*
I	*Current*

V	*Voltage*
IR	*Ohmic drop*
n	*Number of electrons transferred*
℃	*Degree Celsius*
mins	*Minutes*
sec	*Seconds*
℃/min	*Degree Celsius per minute*
Mt	*Metric tons*
Kg	Kilograms
gms	*Grams*
mg	*Milligrams*
mol	*Moles*
J/mol	*Joules per mole*
KW	*Kilo Watt*
J	*Joule*
KWh	*Kilo Watt hour*
KWh/ton Fe	*Kilo Watt hour per ton of iron*
sccm	*Square Cubic Centimeters*
atm	*Atmosphere*
Wt. %	*Weight percentage*
L	*Liquid phase*
s	*Solid phase*

g	*Gas phase*
ref	*reference*
aka	*also known as*
v/s	*versus*
$P_{S_2(g)}/P_{So_2(g)}$	*Partial pressure ratio of $S_2(g)$ to $SO_2(g)$*
$\boldsymbol{\eta}$	*Faradaic Efficiency*
∴	*therefore*
~	*approximately*
&	a*nd*
µ	*Microns*
>	*greater than*
@	*at*

List of Figures

CHAPTER 5

CHAPTER 6

APPENDIX 1

APPENDIX 2

APPENDIX 3

APPENDIX 4

List of Tables

CHAPTER 1

CHAPTER 5

APPENDIX 4

Chapter 1

Introduction

Quoting a recent World Bank publication, **"the clean energy transition will be significantly mineral intensive".**[1]

Metals have been an integral resource for humanity for centuries and are the structural framework of the global economy[2–8], beginning with the stone age and eventually transitioning to the bronze age and the iron age[5,9]. Their unique and advantageous properties combined with affordability result in the ubiquitous use of metals in numerous applications. From construction to automobiles and aerospace to energy systems, health care and common household appliances, metals are increasingly being used in every sphere of society due to their high performance to cost ratio as compared to any other material[2–4]. For instance, modern society has heavily relied on steel for construction and automobiles,

copper in the electrical grid, aluminum in aviation and packaging, rare earths in magnets and alloys[3]. The potential of infinite recyclability of metals (no loss in properties or performance upon repeated recyclability in case of pure metals; however not true for alloys, e.g. presence of residual Cu in steel scrap[10,11] or tramp elements in diverse variety of Al alloys[12] is detrimental to their performance and reduces their value) makes them an attractive candidate for any potential sustainable material use. Apart from day-to-day applications, metals are increasingly in demand for their use in the clean-energy transition for a low-carbon future[1,13]. Since, all carriers of the climate revolution[1,14] are dependent on minerals, e.g. solar panels needing aluminum, silicon, silver, cadmium, germanium; electric vehicle batteries needing lithium, nickel and cobalt; wind turbines needing rare-earth metals like neodymium, praseodymium and iron[15]; the demand for these metals is going to exponentially rise[16].

With such a heavy reliance of society on metals, it is not surprising to conclude the demand for metals is increasing proportionally to the rise in population[17]. This trend has been clearly observed in the case of primary production of commodity metals, such as Fe, Al and Cu whose production has doubled over the last 3 decades with a population increase of 2 billion[3]. The total metal production as of 2019 was 3.248 billion tons (from steel to rare earths), with approximately 58% being steel (1. 88 billion tons) followed by Aluminum, Copper, zinc, and other metals[18]. **Table 1.1** below list the production of the commodity metals as of 2021[19-22].

Commodity Metals	**Production (in tons)**
Steel	1.95 billion
Aluminum	69 million
Copper	22 million
Zinc	13.3 million

Table 1.1 Commodity metal production as of 2021

1.1 Current Steel production

Of all metals, as seen from the production statistics, steel (major component iron) is the most widely used engineering and infrastructural material[22]. The transition from the bronze to iron age[5,9] has been especially important due to the natural abundance of iron ore as compared to copper and tin, which otherwise had to be transported over long distances. However, ore was not the first source of iron. Humans discovered small chunks of metallic substances which were brought along with heavenly bodies such as meteorites[9]. Since there is no oxygen in space, meteoric iron often existed as pure metal, unlike on the earth surface where its oxide is the most stable form. Soon after discovering its excellent properties, smelting of iron especially for weapons (daggers, spikes, arrow heads), tools(knives), ornament and utensils (spoons and saucepans) began. Egypt is known to have been the pioneers in iron production, eventually spreading to the rest of the world[5,9].

Historically iron ore was smelted in a bloomery with charcoal with air being forced through using bellows[5,23]. The charcoal reacted with the oxygen from the ore to form CO (g) which reduced the iron ore further to metallic iron. However, since the temperature was not hot enough, the iron produced would be a porous solid which needed to be worked with a hammer to remove the excess impurities. However, large scale production did not begin until the advent of the blast furnace[5,23,24], in which iron was heated enough to absorb excess carbon. As this product (called molten iron) was not in a usable form, it needed further treatment to reduce the carbon content to produce steel.

From automobiles, cargo ships to household appliances like washing machines and refrigerators, framework of buildings[25], biomedical devices, utensils and heavy industrial machinery, steel serves its purpose in every industry due to its versatile range of properties[2,22]. Its ability to provide desirable mechanical properties like high strength and ductility over a range of application temperatures and environments[26,27], from sub-zero to ~ 600-700 ◦ C and terrestrial to deep sea to space, at relatively low costs; ease of processability and ability to control and improve properties by various chemical and thermal treatments like alloying additions and controlled thermomechanical processing, makes it a remarkable

material[26,28]. With an annual production of over 1.98 billion metric tons as of 2022[22], steel production continues to rise as infrastructural demand increases and as steel becomes an indispensable part of our lives.

However, it was not until 1855, when the Bessemer converter was invented[5,9,23,24], that massive quantities of steel began being produced commercially. This was done by blowing oxygen through a lance at the bottom. Though this technology did not last long enough, the same principle was applied in the till-date widely used Basic-Oxygen-furnaces[29].

The current state-of-the-art steel making is reliant mainly on two technologies[30], serving different markets:

1. ***Blast furnace-Basic Oxygen furnace route (BF-BOF):*** Accounting for over 72% [30,31] of the global steel produced, this route has a vital capacity to meet the increasing steel demand at a competitive price. Years of technological expertise and continual improvements[32,33] have led it to produce high-quality, high-performance steels for say, automotive applications, while also bringing down the energy and reductant requirements close to optimal. However, integrated BF-BOF steelmaking is carbon (1.1- 1.9 t CO_2 eq/ton steel)[31] and energy intensive[34], as it uses carbon in the form of metallurgical coke as a fuel (temperatures in the hottest zones of the blast furnace are higher than 1600° C) as well as a reductant of iron oxide (usually hematite)[30,34]. Due to a miniscule change in the entropy for the reaction in carbon, higher amounts are carbon are needed to maintain the heat balance in the furnace. The integrated steel plant consumes about 5000 kWh/ ton steel and accounting for the massive production volume, the iron and steel industry in the whole comes off as among one of the highest energy consuming plants[31,34–36]. The massive production volume of steel adds to the heavy carbon footprint (~7% of the global GHG emissions)[35] the iron and steel industry has as compared to any other metal extractive industry[31,36]. **Figure 1.1** depicts a schematic of the process flowsheet of the conventional BF-BOF steel making.

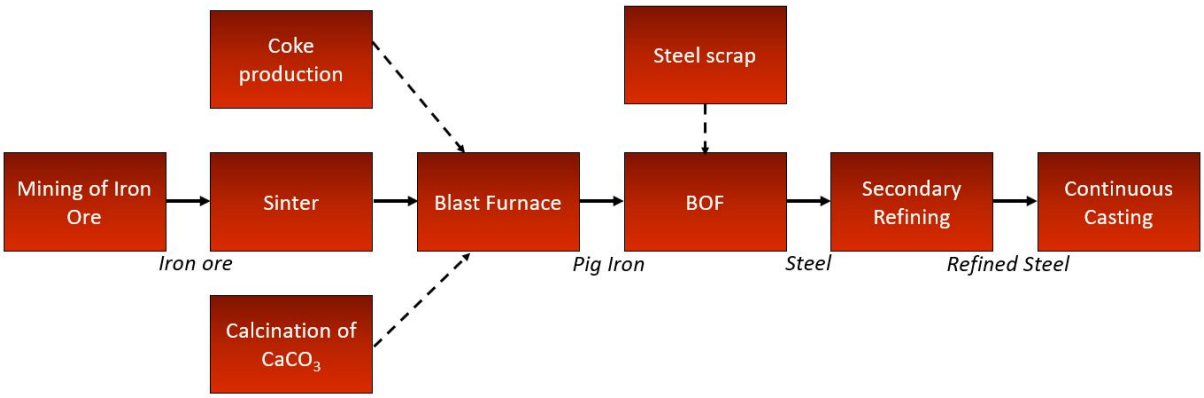

Figure 1.1 Process flowsheet for conventional BF-BOF steel making

2. ***Scrap/DRI melting in an Electric-arc-furnace:*** This technology accounts for 28%[34] (scrap melting accounting 23% and DRI -EAF accounting a mere 5%[22,37]) of the global steel produced, making steel one of the most recycled material on planet earth[31]. Since the EAFs only melt scrap[34] and/or DRI and no reduction process takes place, it is a low energy and low CO_2 intensive process[32]. However, steel produced by scrap melting is not of remarkably high quality due to the presence of impurities (especially residual copper) which are difficult to remove from scrap. Thus, scrap based EAF is only used to manufacture long products for structural purposes.

1.2 Impact on the environment

As the world population continues to grow, the demand for high quality steels is foreseen to only increase, making the environmental impact alarming. As of 2020, the total direct emissions of the steel industry were about 2.6 billion tons[31], accounting for 11% of the global CO_2 emissions. As a reference, the Amazon Forest (earlier known to be the world sink of CO_2 emissions), also can absorb only 1.2 billion tons of carbon dioxide emissions in a year[38]. However, scientists believe that even the largest carbon sink of the planet is a net

carbon emitter[39–41]. Hence, this massive volume of CO_2 in the atmosphere contributes to global warming by increasing the average temperature of the earth[42,43].

With the temperature of the earth steadily rising[43], the situation for us and the future generations is alarming. Climate change is already having catastrophic impacts on the environment with increase in global temperatures, sea level[43] and an increased frequency and extremity of weather changes such as unseasonal showers, extreme heat and cold, etc. The Paris agreement in 2015[42] set climate goals for the entire world to combat the alarming effects of global warming. Limiting the global temperature increase to pre-industrial levels of 1.5 - 2 ◦ C [42] is no easy task especially with the explosion in population density over the last half century and with the subsequent rise in the demand for essentials and energy[17,44]. **Figure 1.2** shows a plot comparing the rate of CO_2 emissions decrement in different scenarios.

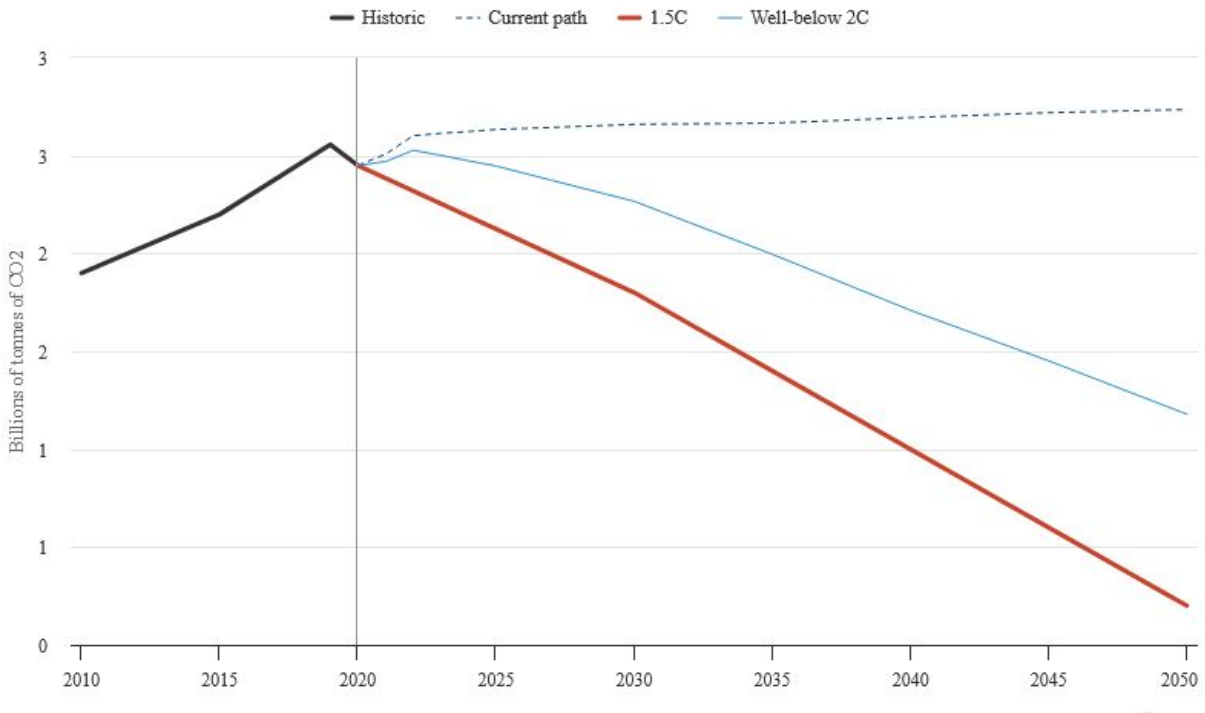

Figure 1.2 Chart [i] comparing rate of decrement of CO_2 emissions by Carbon Brief [45]

[i] The chart depicts the direct CO_2 emissions from the iron and steel sector during 2010-2050. The various plots (explained in the legend) represent emissions for the IEA's stated policy scenarios. Indirect emissions (electricity generation and imported heat) add a third to the total emissions, in 2019: 2.6 Gt CO_2 direct emissions and 1.1 Gt CO_2 indirect.

Additionally, in making the transition in the energy landscape, the demand for fossil fuels will drastically decrease, however it will need a boom in the production of minerals essential for the low-carbon economy[1,13,46,47], most of whose extraction and refining are highly energy and emission intensive industrial processes[15,48]. Thus, we are dealing with a fine trade-off between increased metal production for low-carbon technologies while generating an initial carbon 'debt.'

Given the circumstances, the metals and mining industry already accounts for over 10% of the global greenhouse gas emissions[46]. Over the years, there has been a decline in the high-grade ore deposits [46] (this excludes the untapped ore reserves or resources). And in the quest to fulfil our increasing demand, this trend will extrapolate as resources become scarcer. The decline in the ore grades directly translates to the multiplication in the energy intensity needed to process minerals critical to a low-carbon society[1,13,46]. And since most of this energy presently is realized through fossil fuel sources, the carbon emissions will continue to increase aggressively if metal producers do not act briskly. The metal manufacturing sector is an industry heavily reliant on legacy extractive technologies built on carbon. The well-established and capital-intensive infrastructure makes it increasingly challenging for the industry to replace or make a paradigm shift. However, to minimize the threat of climate change, metal producers need to achieve net-zero emissions by 2050[47].

Given the massive production volume of steel, the highest impact on the environment is of the steel industry, as it contributes to over 70% of the total GHG emissions of the metal sector[34]. The source of these emissions is due to the heavy reliance of steel making process of coal. There are multiple primary unit operations in the BF-BOF route[30,34] such as coke making in coke ovens (endothermic, releases CO, SO_2, particulate matter and other noxious volatile compounds), reduction of the iron ore to molten iron in the blast furnace (releasing CO, CO_2, iron ore fines as dust) and steel making in the BOF (releasing CO_2). Apart from these operations, multiple auxiliary operations take place, for instance pellet/ sinter making, calcination of $CaCO_3$, air separation unit to produce oxygen (used in the blast in the BF and BOF). Each of these operations are very energy intensive and usually this energy is produced by the combustion of fossil fuels, resulting in severe environmental consequences. Since

years, the iron and steel industry has called for efforts towards decarbonizing the steel industry.

Technological improvements have definitely increased the efficiency and productivity of the current blast furnace and BOF route and have brought it closer to thermodynamic efficiency[32,44]. Other techniques like use of coke instead of coal; partial replacement with natural gas as a fuel; carbon capture; effective recirculation of the blast furnace and flue gases from the coke oven and other places of the integrated steel plant, have definitely brought the carbon emissions down. However, since carbon is at the heart of the process, complete elimination has not been possible yet. Hence, a paradigm shift is needed in steel making technology, without severely impacting the capital-intensive investments made in state-of-art Basic-Oxygen furnaces over the world.

1.3 Focus of the present work

As illustrated above, a paradigm shift in steel making technology needs to be introduced to eliminate carbon from the process. Various incentives are being provided to cut down CO_2 emissions, alongside the increasing demand for higher quality steel. This is one the biggest advantages electricity can offer in metal manufacturing; the ease of process control to produce high purity metal products without incurring heavy capital costs, while significantly bringing down energy consumption. As the world marches towards clean energy transition[1], there will be no dearth of clean, emission-free electricity in the future. Integrating this low GHG electricity as a source of heat and thermodynamic work for reducing the ions would make modern metal manufacturing cost effective ($0.05 per kWh, aligns with energy consumption and cost of production for Al in present day) and sustainable[32]. Hence, there is a key need for technologies that use solely electricity for iron ore reduction. At the present cost of steel (produced through the BF-BOF route), our electrical energy requirements to produce steel electrolytically should not exceed 3900 kWh/ ton Fe[44]. Moreover, to be competitive in terms of productivity of existing technologies,

the specific productivity (per unit time and per unit area) of an electrolysis cell for Fe should be twice that of Al[44].

This work will focus on a novel electrolytic route to produce emission-free steel, through a sulfide pathway, Molten Sulfide electrolysis (MSE). The electrolytic decomposition of iron sulfide into iron and elemental sulfur gas operates in a molten sulfide electrolyte. The process operates using sulfide and sulfur chemistry, conditions well known from non-ferrous metallurgy where the exclusion of oxygen supports a virtual elimination of GHG emissions from the reduction step.

In the following chapter, a literature review of the various steel making technologies will be presented and arguments will be made that molten sulfide electrolysis for iron production is a promising candidate for decarbonization efforts of the steel industry. Further, in chapter 3, the thermodynamic framework of the process will be established, including the mass and energy balance. In chapter 4, iron production via molten sulfide electrolysis will be explored experimentally along with a discussion of the characterization techniques used to analyze the experimental samples. Later, in chapter 5, results of the experiments and characterization studies are presented and discussed. Finally, chapter 6 draws important conclusions from the work and explores future scope of the work.

1.4 Summary

The urgency of reducing the environmental impact in the metal processing industry[42,43,47], specifically the iron and steel industry comes at a time when there is a surge in the demand of steel to satiate the increasing demands of energy and essentials for the growing population[17,22]. With steel production approaching 2 billion metric tons[22], the iron and steel industry takes the blame for contributing 11% of the global CO_2 emissions[31,35,36]. As the temperature of the earth increases at an alarming rate[42,43], it is high time the industry makes a paradigm shift in its decarbonization efforts in steel making technology. However, the challenge that comes along is the capital-intensive investments made in state-of-art

current BOF technology, which would pose a financial loss in the event of their potential premature retirements.

This work presents a novel sulfide-based pathway, molten sulfide electrolysis (a process which can potentially reduce up to 88% of the CO_2 emissions from steel making), to produce molten iron electrolytically, while still utilizing the unsurpassed productivity and refining ability of the BOFs in steel making. The following chapters discuss the scientific and experimental framework of the novel route to produce emission-free steel.

1.5 References

(1) *Climate-Smart Mining: Minerals for Climate Action*. World Bank. https://www.worldbank.org/en/topic/extractiveindustries/brief/climate-smart-mining-minerals-for-climate-action

(2) Alloys, E. *The Importance of Metal in Our Society*. Eagle Alloys Corporation. https://www.eaglealloys.com/the-importance-of-metal-in-our-society/

(3) *The Growing Importance of Base Metals in the Global Economy | ETF Central*. https://www.etfcentral.com/news/the-growing-importance-of-base-metals-in-the-global-economy

(4) *The Importance of Metals And Minerals*. Colorado Business Roundtable (COBRT). https://www.cobrt-archive.com/archived-blog/2011/07/the-importance-of-metals

(5) Steel, S. *The History of Iron and Steel*. Superior Steel Fabrication. https://superiorsteelfab.com/precision-metal-fabrication/history-iron-steel-production/

(6) *Economic Growth*. Minerals Make Life. https://mineralsmakelife.org/economic-growth/

(7) *Minerals and Energy - Raw Materials Report*. https://researcher.guide/journals/1404-1049/Minerals%20and%20Energy%20-%20Raw%20Materials%20Report

(8) *Metals use tied to economic upswings*. Industrial Ecology Blogs. https://blog.indecol.no/will-more-expensive-metals-impede-economic-growth-in-the-us/

(9) *The Incredible History of Iron and Steel | An Expert Guide from history to production*. https://wisconsinmetaltech.com/the-incredible-history-of-iron-and-steel/

(10) Ramadan, A.; Shash, A.; El Mahallawi, I.; Senk, D.; Mattar, T. Studying the Effect of Tramp Elements in Scrap on Industrial Recycled Steel Processing and Quality; 2014.

(11) Daehn, K. E.; Serrenho, A. C.; Allwood, J. Finding the Most Efficient Way to Remove Residual Copper from Steel Scrap. *Metall Mater Trans B* **2019**, *50* (3), 1225–1240. https://doi.org/10.1007/s11663-019-01537-9.

(12) Raabe, D.; Ponge, D.; Uggowitzer, P. J.; Roscher, M.; Paolantonio, M.; Liu, C.; Antrekowitsch, H.; Kozeschnik, E.; Seidmann, D.; Gault, B.; De Geuser, F.; Deschamps, A.; Hutchinson, C.; Liu, C.; Li, Z.; Prangnell, P.; Robson, J.; Shanthraj, P.; Vakili, S.; Sinclair, C.; Bourgeois, L.; Pogatscher, S. Making Sustainable Aluminum by Recycling Scrap: The Science of "Dirty" Alloys. *Progress in Materials Science* **2022**, *128*, 100947. https://doi.org/10.1016/j.pmatsci.2022.100947.

(13) Timperley, J. *Explainer: These six metals are key to a low-carbon future*. Carbon Brief. https://www.carbonbrief.org/explainer-these-six-metals-are-key-to-a-low-carbon-future/

(14) *Renewable Energy*. Energy.gov. https://www.energy.gov/eere/renewable-energy

(15) Jones, A. G. Mining for Net Zero: The Impossible Task. *The Leading Edge* **2023**, *42* (4), 266–276. https://doi.org/10.1190/tle42040266.1.

(16) Anonymous. Charging Ahead: Moving Toward the Net-Zero Mine. *Engineering and Mining Journal* **2023**, *224* (3), 54–55.

(17) Ritchie, H.; Rodés-Guirao, L.; Mathieu, E.; Gerber, M.; Ortiz-Ospina, E.; Hasell, J.; Roser, M. Population Growth. *Our World in Data* **2023**.

(18) *This is how much metal we mine every year | World Economic Forum*. https://www.weforum.org/agenda/2021/10/all-tonnes-metals-ores-mined-in-one-year/

(19) *Zinc: global metal production 2022*. Statista. https://www.statista.com/statistics/264878/world-production-of-zinc-metal/

(20) *Copper mine production worldwide total 2023*. Statista. https://www.statista.com/statistics/254839/copper-production-by-country/

(21) *Primary Aluminium Production - International Aluminium Institute*. https://international-aluminium.org/statistics/primary-aluminium-production/

(22) *World Steel in Figures 2022*. worldsteel.org. https://worldsteel.org/steel-topics/statistics/world-steel-in-figures-2022/

(23) *History_of_ferrous_metallurgy*. https://www.chemeurope.com/en/encyclopedia/History_of_ferrous_metallurgy.html

(24) *World Iron & Steel History Timeline*. https://steelmuseum.org/timelines/world_timeline.cfm

(25) *Benefits of Structural Steel | American Institute of Steel Construction*. https://www.aisc.org/why-steel/just-curious/

(26) Media, C. N.; cnmAdmin2030. *6 Reasons Steel is One of the Most Used Metals Today*. Industry Today - Leader in Manufacturing & Industry News. https://industrytoday.com/6-reasons-steel-is-one-of-the-most-used-metals-today/

(27) *4 Main Types of Steel Used in Manufacturing*. https://eziil.com/types-of-steel

(28) Steel. *Wikipedia*; 2024.

(29) *Basic Oxygen Furnace Steelmaking*. https://www.steel-technology.com/articles/oxygenfurnace

(30) World Steel Association. Fact Sheet | Raw Materials in the Steel Industry, 2023. https://worldsteel.org/wp-content/uploads/Fact-sheet-raw-materials-2023.pdf.

(31) *Iron and Steel Technology Roadmap – Analysis*. IEA. https://www.iea.org/reports/iron-and-steel-technology-roadmap

(32) Allanore, A. Contribution of Electricity to Materials Processing: Historical and Current Perspectives. *JOM* **2013**, *65* (2), 130–135. https://doi.org/10.1007/s11837-012-0538-3.

(33) Sadoway, D. R. New Opportunities for Metals Extraction and Waste Treatment by Electrochemical Processing in Molten Salts. *Journal of Materials Research* **1995**, *10* (3), 487–492. https://doi.org/10.1557/JMR.1995.0487.

(34) World Steel Association. Energy Use in the Steel Industry, 2021. https://worldsteel.org/wp-content/uploads/Fact-sheet-energy-in-the-steel-industry-2021-1.pdf.

(35) *Steel Climate Impact - An International Benchmarking of Energy and CO2 Intensities*. Global Efficiency Intelligence. https://www.globalefficiencyintel.com/steel-climate-impact-international-benchmarking-energy-co2-intensities

(36) *Climate change policy paper - worldsteel.org*. https://worldsteel.org/publications/policy-papers/climate-change-policy-paper/

(37) Benavides, K.; Gurgel, A.; Morris, J.; Mignone, B.; Chapman, B.; Kheshgi, H.; Herzog, H.; Paltsev, S. Mitigating Emissions in the Global Steel Industry: Representing CCS and Hydrogen Technologies in Integrated Assessment Modeling. *International Journal of Greenhouse Gas Control* **2024**, *131*, 103963. https://doi.org/10.1016/j.ijggc.2023.103963.

(38) *Carbon sink: Where is the world's most important rainforest?* euronews. https://www.euronews.com/green/2023/03/31/first-lung-this-rainforest-could-be-the-worlds-most-important-carbon-sink

(39) Taylor, C. *The Amazon rainforest is now releasing more carbon than it can absorb, study finds*. CNBC. https://www.cnbc.com/2021/07/15/amazon-rainforest-now-releasing-more-carbon-than-it-absorbs-study.html (accessed 2024-03-15).

(40) The Brazilian Amazon Has Been a Net Carbon Emitter since 2016. *The Economist*. https://www.economist.com/interactive/graphic-detail/2022/05/21/the-brazilian-amazon-has-been-a-net-carbon-emitter-since-2016

(41) *New study offers latest proof that Brazilian Amazon is now a net CO2 source*. Mongabay Environmental News. https://news.mongabay.com/2021/09/new-study-offers-latest-proof-that-brazilian-amazon-is-now-a-net-co2-source/

(42) *The Paris Agreement | UNFCCC*. https://unfccc.int/process-and-meetings/the-paris-agreement

(43) Nations, U. *What Is Climate Change?* United Nations. https://www.un.org/en/climatechange/what-is-climate-change

(44) Allanore, A. Electrochemical Engineering for Commodity Metals Extraction. *Electrochem. Soc. Interface* **2017**, *26* (2), 63. https://doi.org/10.1149/2.F05172if.

(45) Staff, C. B. *Guest post: These 553 steel plants are responsible for 9% of global CO2 emissions*. Carbon Brief. https://www.carbonbrief.org/guest-post-these-553-steel-plants-are-responsible-for-9-of-global-co2-emissions/

(46) Lezak, S.; Cannon, C.; Blank, T. K. *Low-Carbon Metals for a Low-Carbon World: A New Energy Paradigm for Mines*. A New Energy Paradigm for Mines, Rocky Mountain Institute. https://rmi.org/wp-content/uploads/2019/12/Low-Carbon_Metals_for_a_Low-Carbon_World.pdf

(47) *Net Zero by 2050 – Analysis*. IEA. https://www.iea.org/reports/net-zero-by-2050

(48) Alam, S. Energy-Saving Green Technologies in the Mining and Mineral Processing Industry. In *Energy Technology 2023*; Alam, S., Guillen, D. P., Tesfaye, F., Zhang, L., Hockaday, S. A. C., Neelameggham, N. R., Peng, H., Haque, N., Liu, Y., Eds.; Springer Nature Switzerland: Cham, 2023; pp 89–96. https://doi.org/10.1007/978-3-031-22638-0_9.

Chapter 2

Literature Review

As illustrated in the previous chapter, the steel industry is both capital and energy intensive, along with a significantly large share of carbon footprint. Its massive carbon emission share comes from the industry's heavy reliance on coke (carbon), both as a reductant and fuel. As of 2019, the total carbon dioxide emissions were 3.6 Gt for a steel production of over 1.95 billion tons[1] annually to meet the growing demand. Thus, as efforts towards decarbonization intensify owing to the stricter guidelines the iron and steel industry must abide by, there is an urgent need to make a shift in the present iron and steel making technology. This is done by exploring different routes eliminating the use of carbon from the reduction process. The previous chapter motivated the use of electricity to be a key component in alternative steel making technologies, especially in terms of reduction in energy consumption. This chapter will discuss the features and challenges of some of the prominent electrochemical alternatives practiced, followed by a discussion of historical

evidence with electrolysis of other metal sulfides and why molten sulfide electrolysis is a potential candidate for sustainable iron making.

2.1 The transition of the use of electricity in materials processing

Materials processing, especially in the context of metal manufacturing/ processing requires high temperatures (several hundred degree Celsius). Usually, these temperatures are achieved using fossil fuels or reactants leading to highly exothermic reactions, e.g., oxidation of carbon to CO_2 in both iron and steel making. It was not until the early 19th century[2], that electricity was used both as a source of heat (to achieve extremely high temperatures, otherwise difficult to achieve) and chemical work (supplying the required minimum chemical energy to reduce ions) to produce metals. The underlying principle is driving a non-spontaneous and usually endothermic reaction by providing an external electric potential. The use of electricity simplified the process flowsheet, in terms of both cost and technology - e.g., Aluminum (Al), for several metals and in some cases enabled production of a elements like sodium, magnesium, chlorine, etc. The associated Joule effect (due to the resistance for the movement of charge through the electrolyte) resulted in the simultaneous release of heat, needed to maintain temperatures to run the reaction along with enabling liquid metal production for higher productivity. Indeed, "with respect to energy and raw material efficiency, electrochemistry offers unique possibilities which in very few cases have been realized to a satisfactory extent.[3]" At present, Al produced globally is entirely via electrolysis[2] , thanks to the independent and simultaneous pioneering work of Charles Hall and Paul Heroult in 1866. The metallurgical industry thus already has a benchmark set for primary extraction in the form of bauxite electrolysis to produce Al.

The use of electricity in the steel industry is not new and has been in use for several decades, especially in the form of electric arc furnaces (EAFs) to process the increasing

amount of scrap being generated. Evidence states that the United States has witnessed a notable decrease in the emissions as well as the energy consumption as it increasingly made the timely shift to EAFs[2]. Although, melting of scrap in the EAFs cannot be directly compared to reduction from iron ore while discussing the energy consumption and emission generation, it is a good measure to justify that use of electricity is nevertheless beneficial and is already a reality. As the present state-of-art BF-BOF route is optimized enough to be working close to the thermodynamic limit, any further significant reduction in energy or coke consumption is nearly impossible[2].

This emphasizes the development of breakthrough and incremental steel making technology, especially those using electricity to directly reduce iron ore. And with the recent surge in the development and deployment of renewable technologies for decarbonized electricity generation, using electrical energy for primary metal production comes across as a sustainable alternative. However, the inability of renewable energy sources to provide steady current (usually electrolytic facilities need steady high currents for operation) prevents their widespread adoption. Previous work on the techno-economic analysis of Cu production by MSE of chalcopyrite[4] (see L. Rush thesis for reference), concluded the ability of the MSE reactors to benefit from the intermittent nature of the renewable sources.

The performance and ability to balance the energy conditions of the electrochemical route is a function of the electrolytic cell design and the electrolyte composition. The thermodynamic advantage of using an electrolytic process comes from a practical characteristic of irreversibility: Joule's effect. At high temperature, the reactor of a certain size can maintain the process temperature by self-heating. This heat is generated as a source of resistivity in the electrolyte. Additionally, electrolytic production route opens new avenues for utilizing low-grade ores that were uneconomical to mine and process via the BF route. The following sections will discuss the low temperature and the high temperature electrochemical routes for iron production.

2.2 Aqueous Electrochemistry – low temperature route for iron production

One of the alternatives for decarbonized steel making is the alkaline electrowinning of iron from hematite[3–7]. The aqueous electrochemical iron making route is a technique which involves the electrolysis of a suspension of finely milled iron oxide particles (hematite) in a highly concentrated alkaline electrolyte (pH =15) at a temperature of 100° C.[5] This not only allows ore fines to be processed but also works well with red mud[6] (by-product of bauxite beneficiation). This sustainable process offers several advantages: benign by-products (oxygen gas; uses an inert Pt/Ni anode), reduction of CO_2 generation (87%), low working temperature (as compared to temperature higher than 1600° C in the conventional route) and an energy consumption[5] of ~2600 kWh/ ton Fe, equivalent to the thermodynamic minimum of the chemical energy needed to produce Fe from hematite.

2.2.1 Process Mechanism

The aggregation of the fine hematite particles is prevented by the stability of these particles in the concentrated alkaline solution. The reaction occurs in the following steps:

1. Adsorption of the hematite particles[7–9] to the cathodic surface (Ni or Fe) owing to the electrostatic interactions (spontaneous adsorption)
2. Electrolytic reduction facilitated by the formation of a Fe_3O_4 intermediate[7,9] serving as the electronic conducting phase while the reduction occurs in a shrinking core mechanism; metal deposition occurs from the surface to the core

Although hematite is an electrical insulator, the reaction proceeds due to the formation of Fe_3O_4 and subsequently Fe that increases the electrochemically active area[9]. Thus, the efficiency of the process depends on the size of the particle (large particles may not achieve

full conversion) and the electrical contact established. The governing reactions are postulated to be as follows:

Reaction of the dissolved Fe^{+2} particles with hematite[9]:

$$Fe_2O_3 + Fe(OH)_3^- \rightarrow Fe_3O_4 + H_2O + OH^- \quad (2.1)$$

$$Fe_3O_4 + 2e^- + 4\,H_2O + OH^- \rightarrow 3\,Fe(OH)_3^- \quad (2.2)$$

Thermodynamic favorability of reduction reaction due to increase in [Fe^{+2}]

$$Fe(OH)_3^- + 2e^- \rightarrow Fe + 3\,OH^- \quad (2.3)$$

The process observes an energy efficiency of 80% in highly concentrated suspensions, thanks to the high conductivity of NaOH, with current densities[8] of up to 0.11 A/cm^2 even at low temperatures and close to the minimum required thermodynamic potentials. The usual valency shift between Fe^{+2} and Fe^{+3} does not occur in this method, as it only involves the reduction of the particles adsorbed to the cathode. In a bulk electroreduction, iron ore lumps are used as the cathodes by mechanically connecting them to Ni or steel current collectors.

However, one of the biggest contributors to lowering the faradaic efficiency is the HER[6] (hydrogen evolution reaction). Not only does it compete electrochemically with the Fe^{+2} reduction but also hinders the electrical contact[9] of the particle and the electrode. The other challenge comes in the form of the extremely selective nature of the feedstock. Other iron ores such as goethite (highly viscous slurry resulting in mass transport limitations) and magnetite (HER being more favorable, possibility of back oxidation reactions) do not offer the same faradaic yield and are extremely poor performers (current density at cell voltage = 1.66 V: 0.07 A/cm^2 and 0.015 A/cm^2 respectively)[8], which makes only pure hematite suitable for the process. In fact, the current yield gets affected due to impurities[6], as observed in the lower efficiencies reported for titanomagnetite (natural iron sands) used as feedstock.

2.2.2 Challenges

Although the process serves as a direct electrochemical reduction of iron ore at low temperatures, the following are the challenges which create hindrance in its widespread adoption:

1. Since the volume of suspension to be handled is high (low solubility of the hematite particles in the electrolyte; 0.002 mol/L)[7], the specific energy consumption of the process is high, low productivity
2. The current density is low implying low productivity[8] (incomparable to the present steel manufacturing capacity in a typical facility ~ 4 - 6 Mt/annum)
3. The deposited iron is solid in the form of plates (5mm) as a columnar deposit. With solid deposits, additional downstream facilities for rinsing, compaction and melting (EAFs) will be needed in comparison to liquid metal that is easy to process (refining, alloying, casting, etc.). Additionally, electrodeposition at limiting current density may result in uneven growth of the metal dendritic deposit.
4. Possibility of precipitate formation upon interaction[5] of the solid hematite particles at the air/electrolyte interface.

2.3 Molten Oxide Electrolysis: high temperature route for electrolytic production of iron

One of the biggest drawbacks of aqueous/ low temperature iron production is the final product being in the solid state[5], requiring additional facilities to melt and process the iron. Metal processing (refining, alloying, casting) has higher productivity in liquid state by ensuring homogeneity in composition while avoiding phases difficult to perform any operations on. To produce steel or iron in liquid form, the operating temperatures must

exceed the melting point of iron (1539^{o}C). To sustain such exceedingly high temperatures, the electrolyte must possess certain characteristics[10]:

- Thermally stable at such high temperatures
- Good solubility of the molten oxide feedstock
- Ionic conductor, with minimal electronic conductivity
- Should allow high mass transport rate of the ions through the electrolyte
- Chemical stability against Fe-O_2 chemical potential gradient

The aluminum industry has set a benchmark for high temperature electrolytic processes and their mature technology has proved molten salts to be ideal electrolyte candidates. The primary production of aluminum relies on the electrolytic process, wherein after separating alumina (Al_2O_3) from bauxite, it is dissolved in an ionic melt of fluoride salts called cryolite (Na_3AlF_6, AlF_3 and CaF_2) to yield liquid Al at the cathode and CO_2 at the anode (from consumption/ oxidation of the carbon anodes) upon electrolysis[11]. The current density is about 1 A/cm^2 resulting in high productivity of the liquid metal; this limit is set by the maximum allowable concentration of Al_2O_3 in the ionic melt[12] (although the cryolite can dissolve more amount of alumina). Fluorides were chosen as they depicted a high enough solubility for alumina as well as formed a eutectic composition in the operating temperature range for superheated liquid Al (to ensure a low viscous product, that is easy to flow) production.

Building on the same concept, the Molten Oxide Electrolysis (MOE) process[12] for steelmaking was developed for direct reduction of the iron ore to produce liquid metal, using electricity as its primary energy input, to reduce emissions, energy consumption as well as cost (by reducing number of unit operations). In this process, iron ore is dissolved in a molten oxide[12] electrolyte to produce pure liquid Fe at the cathode and O_2 at the anode in an endothermic reaction (consuming heat), upon passing current at a temperature higher than 1600° C. Carbon anodes, though stable at this operating temperature, are not a suitable choice due to the generation of CO/ CO_2 and subsequent consumption upon interaction with the oxygen gas released at the anode. Hence, to eliminate carbon emissions, an inert anode is required. The electrolytic decomposition requires a thermodynamic minimum[10] of 2600

kWh/ ton of liquid Fe (as derived from the enthalpy balance of the oxide decomposition reaction at 1600° C . However, accounting for the heat losses from the system (assumed at 40%, reference of the industrial Al electrolysis process), a minimum of 3600 kWh/ton liquid Fe[10,12] is needed to do the chemical work of reducing the ions while maintaining the temperature in the electrolytic cell.

Since the role of carbon is eliminated, there is no means for carbon or sulfur (usually enters steel through coke used in the BF) to get into the liquid Fe, thereby leading to the production of liquid iron with equilibrium amount of dissolved oxygen[12]. This is beneficial in producing extremely high-quality steel, devoid of any carbon impurities or nitrogen interstitials in fewer unit operations. The present industrial route utilizes a sophisticated although expensive technology of Argon oxygen decarburization (AOD)/ vacuum degassing for carbon removal to achieve ultra-low carbon concentrations, re-melting, alloying, etc.) of producing special steel grades. Starting with pure Fe, it is relatively very simple to achieve any composition by just an addition of the required elements in the required quantity., e.g., carbon can be added to attain the desired steel composition by adding scrap steel, coal or biogenic carbon)[12].

MOE for steel making is attractive and advantageous due to the following reasons:

- Environmentally benign: Since the process eliminates coal entirely, there are no CO_2 or SO_2 emissions (from the coke making or iron making process)[2,10,12]
- Less capital intensive: The direct reduction process reduces the number of unit operations[12], e.g., coke ovens, BF, BOFs, secondary refining, etc.)
- High solubility of the oxide: Higher concentrations of the iron oxide (up to 10 – 20%)[12] in the molten salt electrolyte (as compared to aqueous electrolyte[7]) resulting in high achievable current densities and hence higher productivity. The reason for the high solubility is due to the electrolyte being a mixture of other oxides such as calcia, silica, iron oxides.
- High temperature process facilitates liquid metal production in a semi-continuous manner to be periodically cast; additionally, faster reaction in the electrolytic cell due to enhanced kinetics and mass transport.

- High limiting current density[12] (2 A/cm^2): results in higher productivity necessary for meeting growing demands of commodity metal extraction. The reactant transport kinetics to the electrode surface and the bubble-induced convection influence the limiting current densities of the cathode and anode.

2.3.1 Electrolytic design/ setup

High temperature processes impose many functional requirements for the various components of the electrolytic cell, especially in terms of thermal and chemical stability. To check material compatibilities, Ellingham diagrams come in handy, as they depict reactivity of the oxide compounds with respect to temperature. The following section describes the design of the electrolytic cell including functional and material requirements of the cathode, anode and the electrolyte.

2.3.1.1 Cathode

The cathode is where the ions get reduced, in this case, reduction of Fe^{+3} cations to liquid Fe metal. Usually, the cathode material is conductive (if not, a conductive material is used as a current collector, preferably metals) while being less reactive than the metal to be deposited to avoid a metallothermic reaction[10]. Some alloying of the cathode substrate and the metal product occurs due to dissolution of the depositing elements (minimum solubility). This may also change the composition of the metal product (alloyed with the cathode substrate) and/or the surface of the cathode substrate thereby altering the deposition thermodynamics of the target metal[10]. With respect to thermal stability and electrical and thermal conductivity, carbon is a suitable candidate. However, C is a reductant for iron oxide and will spontaneously react (carbothermic reduction) with the electrolyte to form Fe-C alloy. The whole purpose of steel production without C is lost as a spontaneous carbothermic reaction occurs when the cell is not polarized[10]. Usually (as followed in the Al industry), a

pool of liquid metal (same as the target metal to be deposited) is maintained as the cathode, while having a solid conductive bottom plate as the current collector.

2.3.1.2 Electrolyte

The electrolyte serves as the solvent for the target metal oxide (in this case iron oxide). Factors such as conductivity, density, composition, viscosity, stability are important to be considered[10,13]. Since it serves as a medium of transport for the ions between the two electrodes, it is supposed to be a good ionic conductor (dissociate to ions). This is an important characteristic since low ionic conductivity[10,12–14] would lead to very high ohmic drop and too high cell voltage. Electronic conductivity of the electrolyte would reduce the efficiency of the electrolytic process as charge would flow directly as electrons rather than ions participating in faradaic reactions.

Most oxides (including oxides of iron) are electrically conducting at high temperatures[12], and above their melting points they exhibit high ionic conductivity[15]. With the addition of certain other oxides like calcia, alumina, silica, etc., their ionic character further increases[12]. These oxides exhibit high melting points and transition-metal oxide solubility, and a large range of thermal stability[10]. Thus, these oxides are key components of the electrolyte in MOE. These are good ionic conductors as compared to silicates (covalent due to the network structure) or the semi-conducting transition metal oxides. The latter show a higher share of electronic conductivity than ionic conductivity. FeO cannot be directly used as an electrolyte due to such high electronic conductivity. This is because upon melting, all charge gets transferred as electrons and not as ions; molten oxide mixtures rich in FeO have been shown to exhibit a transport number close to null[10].

Other physicochemical properties of the electrolyte are important. A low vapor pressure helps reduce molten electrolyte losses. The density of the oxide electrolyte mix, though higher than other molten salt electrolytes, is still less than the Fe (target metal), resulting in sinking of the metal deposit at the bottom, while the electrolyte floats atop. A high viscosity may hinder the mass transport of the ions, increasing the electrolyte resistance

and limiting the reaction rate. Thus, such processes are operated at high superheats, with an optimized melt composition to control the viscosity as reactions proceed. Additionally, the electrolyte should not contain more noble species than Fe (elements having a less negative reduction potential than Fe), as they may compete for reduction.

The high melting and corrosive/ solubilizing oxide melt are held in a container formed by freezing the electrolyte[10,12,16] at the sides forming a frozen/solid wall (similar to the Hall-Heroult process).

2.3.1.3 Anode

The anode is the other electrode in the electrochemical circuit and hence should also be electrically conductive, chemically inert to electrolyte, mechanically robust and electrochemically stable. It should be thermally stable (operating temperatures higher than 1600° C) and resistant to attack by the oxygen generation at the anode[14]. This is because the reaction at the anode encompasses the release of oxygen gas (oxidation of O^{2-} to O_2) thus, any metal used as the anode is subjected to get consumed due to corrosion under anodic polarization[14]. The oxide melt used as the electrolyte has a high solubility for other oxides, thus ends up dissolving most passivating oxide layers on the anode surface, exposing virgin metal for further oxidization.

Iridium initially serves as an inert oxygen evolving anode[14] in iron-bearing alumino-silicate melts. The mechanism through which the anode material sustained without significant consumption was surface reconstruction by chemically combining with an electrolyte constituent to form an intermediate compound. This was referred to as oxide mediated inert anode[14]. Parameters like temperature, electrolyte and alloy composition can be tuned to adjust the rate of the reactions[13,14] (dissolution, decomposition, etc.) that deplete the oxide layer over the anode. For example, the consumption of the anode is about 20 times higher in a basic electrolyte[13] (high calcia), than in an acidic electrolyte containing more silica. This is because electrolytes with higher basic (calcia) content dissociate easily into ions providing a path for iridium to transfer between the electrodes (resulting in anode

consumption), as compared to those with high silica content which polymerize to form a network to allow direct transfer of electrons. It is for this reason that considering physicochemical properties, a basic electrolyte composition is desirable in terms of ionic conductivity and low viscosity but challenging to be compatible with the anode[10,13,16].

Even though the stability of the iridium anode is proved to be good in several electrolytes, it cannot be deployed on an industrial scale especially given the tight economics of steel production, as it is extremely expensive and rare in abundance[14,16] (not sufficient to meet the demands of the industry).

Thus, a new anode material, $Cr_{1-x}Fe_x$ alloy (Fe varying from 0- 30%)[16], was recently developed as a more affordable anode. The Fe-rich limit of the alloy composition is due to the Fe-Cr melting point. The stability of this material as an anode is attributed to the in-situ formation of a stable, electronically conductive oxide layer and the limited internal alloy oxidation. The oxide layer is a solid solution of Al, not present in the alloy but coming from the electrolyte, and Cr oxides in a corundum structure[16]. Use of the Cr alloy as anode exhibits similar performance in terms of faradaic efficiencies when compared to the iridium anodes, resulting in a pure liquid Fe with very little dissolved Cr and O.

2.3.2 Challenges

Due to the anode material compatibility issues[10,12–14,16], implementation of MOE was challenging, before the development of the $Cr_{1-x}Fe_x$ alloy as anode . Electrolytic Al production becoming commercial served as motivation for researching about the challenges in material selection for the electrodes, cell wall, etc. Other challenges in the process are as follows:

1. One of the biggest drawbacks affecting the faradaic efficiency is the presence of multiple valences[10] of Fe in their oxides (Fe^{+2}, Fe^{+3}). Thus, upon passing current, there is always a possibility of back oxidation of the associated ions or partial reduction.

2. A fine compositional balance needs to be achieved between controlling the conductivity (affects the faradaic efficiency) and viscosity of the electrolyte (affects the mass transport of the ions)[10,13,16]
3. Affordable anode material: the proposed inert anode has a finite lifetime due to consumption (corrosion) owing to release of the oxygen at the anode[14,16].
4. Electrolyte design optimization for low energy consumption and high productivity is a challenge, in part due to the limited physicochemical understanding of molten systems.[10,16]
5. The liquid iron product contains a residual solubility of 3000 ppm[16] of oxygen (minimum solubility of O in Fe at 1600°C) requiring further refining at the low available superheat.

Despite these challenges, there is active research going on in the area to make this sustainable steel making alternative technologically and economically feasible. Moreover, this technology has the potential to be exploited for use on the moon and Mars to produce oxygen as well as structural metals[14].

2.4 Electrochemical reduction of sulfides

As discussed in the previous sections, there have been some challenges with electrolytic processes resulting in their limited adoption. The foremost one being competing against the well-established and mature carbon-based extractive technology in terms of its cost competitiveness, productivity, leveraged by the operational economies of scale[17]. The level of technology refinement in the BF-BOF steel making process does not allow any operational inefficiency in other steel making alternatives[17]. With MOE, there are challenges with respect to an affordable inert anode being used on commercial scale (though Cr alloys are shown are sustain in lab scale)[13,14]. This is where technology involving the electrochemical reduction of sulfides is promising, because it involves the release of S_2 gas in place of O_2. If not compromising the stability of the anode, the released S_2 gas can be

condensed and stored for future use, e.g., energy generation or pretreatment processes like sulfidation[18,19].

The concept of electrolytic reduction of sulfides has been discussed in literature since 1906[20], although for non-ferrous chalcolithic ores like Pb, Cu, etc. This is because conventional metal extraction from sulfides has been one of the largest emitters of SO_2 and these minerals cannot be reduced carbo-thermically due to the higher stability of sulfides over CS_2.[21] Furthermore, conventional smelting incurs handling difficulties with the increased concentrations of impurity elements like As, Sb and Bi in the Cu deposits[22]. Due to its release into gas and condensed streams, it requires more stringent management of the hazardous waste generated. Electrolysis of sulfides not only reduces the energy consumption (sulfides have lower thermodynamic decomposition voltages as compared to oxides and chlorides)[23] but also could support the selective recovery (as in any other electrolytic process) of multiple elements present in the ore at various sequences of electrolysis[24]. Additionally, electrifying metals production offers avenues for integrating it with renewable energy and reducing the cost of production; lesser number of unit operations, hence low capital. The following sections discuss the sulfide electrolysis in halide and sulfide electrolytes.

2.4.1 Sulfide electrolysis in halide electrolytes

Aqueous electrolytes have been unsuitable for reduction of sulfides[20] due to low solubility of sulfides in such media. Even under severely harsh leaching conditions, metal reduction may not be complete, and the sponge obtained usually contains impurities making it unusable. In 1906, it was discovered that molten alkali or alkaline earth metal halides exhibited a decent solubility (more than aqueous electrolytes) for sulfide ores, and they could be electrolytically reduced in the melt to produce liquid metal[20]. The high solubility of the sulfides allowed higher current densities and the high operating temperatures and molten states enhanced the transport and hence the kinetics. The discovery was initially for

Pb ores (galena) using it as the cathode due to its high electrical conductivity and a graphite anode to produce liquid Pb which was siphoned off while simultaneously adding fresh ore to the electrolyte to keep the cell functioning. The graphite anode was observed to be non-consumable, indicating that the S_2 gas did not react with the anode to produce CS_2.[20]

The reason why sulfides were not directly electrolytically decomposed was due to the high electronic conductivity of transition metal sulfides[25], most of them behaving like semiconductors. The long-range directional order resulting in the sulfide network[26] allows for electron transfer. Due to this, either it is impossible to electrolytically decompose them directly, or the faradaic efficiency of the process is extremely low. It was found that the addition of certain compounds, especially metal chlorides, can make the solution ionic. They lower the electronic conductivity by breaking this structure down to small monomers or dimers and isolating them into the halide solvent[26]. Since the energy gap for the electron to jump from the valence to the conduction band increases, the electronic conductivity decreases. Thus, if the concentration of the sulfides is low in the metal chloride solvent, the solution behaves as an ionic conductor. However, with increasing temperature they behave more like semiconductors. This is due to the increasing electronic conductivity at elevated temperatures, due to more probability of the electron to jump to conduction band, along with impurity type mechanisms carrying the electrons. Also with increasing sulfide concentration, the solution starts behaving like pure sulfides with increased electronic conductivity, reducing the faradaic efficiency[26]. Thus, a fine balance needs to be observed while balancing the electronic conductivity and productivity (dilute concentrations lowering the mass transport). Several variations of sulfide electrolysis in halide electrolytes have been tried. Initially, using $CuCl_2$ or KCl and NaCl electrolytes[27] at an operating temperature of 450 – 700 °C, lower efficiencies were incurred due to the non-uniform dendritic deposits, hard to recover from the cathode. In another chloride system[26], copper was selectively recovered from a synthetic equivalent of chalcopyrite (Cu-Fe-S matte) in excess molten CuCl. Upon dissolution, the FeS reacted with the CuCl to form soluble $FeCl_2$, while the Cu_2S stayed as it is, thus selectively producing large dendritic Cu crystals at the cathode upon electrolytic decomposition[26].

A different technique referred to as anode electrolysis[21] is also being researched using LiCl and KCl as the electrolyte at 500° C. In this process the sulfide feedstock is used as the anode, oxidizing to form S_2 gas. The metal ions, which are smaller size of ions as compared to S^{2-} get transferred through the electrolyte to the cathode where they get reduced. Though the energy consumption is low, since the product is a dendritic deposit, it is not a viable route for commercial scale production.

At times, growth of these dendrites has also resulted in short-circuiting of the cells[25]. To avoid dendritic deposit at the cathode, Mingsheng et.al, demonstrated electrochemical sulfur removal in a NaCl – KCl melt[27] at 700° C with a solid cathode of $CuFeS_2$. The S^{2-} ions from the cathode, oxidized at the inert graphite anode to S_2 gas, while the metal stayed in the solid. The mechanism[27] included insertion of the cations (Na^+, K^+) from the electrolyte into the cathode partially reducing the Fe^{+3} to Fe^{+2}, followed by complete reduction to a mixture of Cu and Fe with a current efficiency of 85% at a comparatively higher cell voltage of 2.4 V.

However, to improve productivity and have a high throughput, a molten product is preferred. This necessitates the availability of an electrolytic melt in the temperature range of the melting point of the target metal (Cu in this case, 1100 – 1200° C). Thus, using $BaCl_2$ as the supporting electrolyte[25] for Cu_2S (periodic feeding), molten Cu was tapped at the cathode with S_2 gas released as the anode at a current efficiency of 90%. CS_2 formation was avoided by maintaining the cell head temperature above the boiling point of S_2 to ensure it was carried away by the carrier gas stream into the filter to condense. The maximum efficiency was recorded at a temperature just above the melting point of Cu_2S, however it was dependent on the cell design. The disadvantage however was generation of cuprous ions at the anode leading to the precipitate of Cu_2S in a back reaction[25].

In all the above processes using halide electrolytes[20,25–27], a competing reaction of oxidization of Cl^- ions occurs at the anode, not only creating problems of reduced anodic efficiency but complicating by-product handling streams to now handle Cl_2 gas as well. Hence, other electrolytes such as borax[23] were also tried to eliminate this issue. However, though the process could directly produce copper from its sulfide using an inexpensive and reusable electrolyte, there were disadvantages such as consumption of the graphite leading

to carbon emissions, low current densities leading to low productivity as well as competition between the electrolyte compounds and the target elements resulting in them co-depositing at higher current densities.[23]

Recently, Sadoway et. al demonstrated production of liquid Sb from stibnite (sulfide) in molten salt electrolysis process[28]. Capitalizing on molten transition metal sulfides behaving like semiconductors, molten halide electrolytes being S^{2-} ion conductors, and the molten form of deposited metal, alkali-metal halide as well as transition metal sulfide being immiscible with each other, this process, using a secondary electrolyte to block the transfer of electrons, produced high purity molten metal. The S^{2-} ions get transported through the molten halide electrolyte to get oxidized to S_2 gas at the graphite anode. Differences in density segregate (in increasing order of density) the halide electrolyte, molten sulfide and molten metal reduced at the cathode with an efficiency of 88%, in the electrolytic cell.[28]

2.4.2 Towards sulfide electrolysis in sulfide-based electrolytes

To solve some of the challenges of the previous approaches, especially the solubility restrictions of sulfides in chlorides[20,21,26,27,29] (directly impacts the productivity) and their vulnerability to impurities in the melt, alkali and alkaline-earth metal sulfides[30–32] were studied as potential candidates for electrolytes. Due to the large electronegativity difference of these elements with sulfur[24], they are ionically bonded with each other. Adding these sulfides suppressed the electronic conducting behavior of transition metal sulfides, stipulating their use as supporting electrolytes. BaS was chosen due to its large bandgap (3.92eV)[33] as compared to Cu_2S (1.21 eV)[24,34], resulting in an electrical conductivity (0.01/ ohm-cm) 7000 times smaller than Cu_2S[35], its partially ionic nature and significantly higher decomposition voltage as compared to the target metal sulfide. The BaS-Cu_2S binary phase diagram was studied to choose the electrolyte composition to result in a homogeneous liquid. Thus, at a temperature of 1105^{o}C (higher than melting point of Cu), high purity liquid Cu was electrolytically extracted from a sulfide electrolyte composing 43.2 wt.% Cu_2S and

56.8 wt.% BaS, while simultaneously evolving S_2 gas at the graphite anode. The liquid Cu produced was ascertained to be a product of electrolytic reduction as no spontaneous decomposition occurred in the absence of electrochemical signals. Though the measured cathode efficiency was limited to <30% due to challenges in metal dispersions on the small cathode used (mm size cathode), this served as a successful demonstration of sulfide electrolytes being used for faradaic applications[24]. To maintain the efficiency of the electrolysis process over time, continuous feeding of Cu_2S was envisioned to prevent a BaS rich phase from precipitating around the cathode (due to depletion of feedstock) that obstructs further progress.

Sahu et.al demonstrated increased faradaic efficiency of 59% for the same process by modifying the electrolyte composition by the addition of La_2S_3 contributing to the increased ionic conductivity[36]. The addition of the rare-earth metal sulfide reduced the vapor pressure of the electrolyte, further increasing the operational temperature range[36]. Condensed elemental sulfur was obtained as the anodic product, along with gas evolution evidence also observed in the form of voids in the electrolyte. The unavailability of a ternary phase diagram was a limiting factor in the empirical choice of the electrolyte composition. Moreover, due to the unknown solution effects of molten sulfides, any thermodynamic assumption in a multi-component system may not be valid.

Recently, Cu and Fe were selectively recovered from chalcopyrite by molten sulfide electrolysis[22] (with preferential Fe deposition). Though Cu_2S demonstrates high solubility in BaS, to keep the electronic conductivity minimal, only 10 wt.% of chalcopyrite was dissolved in 90% of the supporting electrolyte (55.8 wt.% BaS, 34.2 wt.% La_2S_3). The electrolysis sequentially produced molten iron and liquid Cu. The productivity of the process exceeded industrial standards with current densities as high as 1.5 A/cm^2 being recorded. The interaction between Cu-Fe-C[37] ternary and the unique composition of the supporting electrolyte facilitated the separation of iron and copper due to differential solvation resulting in reduced activity of Cu_2S. Once the local depletion of Fe occurred due to its deposition, the Cu rich phases started precipitating, following the reaction mentioned below[22]:

$$CuFeS_2 \rightarrow Fe\ (l) + S_2(g) + Cu_2S \tag{2.4}$$

$$Cu_2S \rightarrow Cu(l) + S_2(g) \quad (2.5)$$

To ensure that the supporting electrolyte is not degraded due to formation of any oxysulfides, and can be reused, the feedstock was treated in a sulfidation reaction[19] to convert any oxygen containing species to sulfides. Before this 'sulfidised' feedstock was fed to the cell, the immiscible residual gangue phases were separated.

Along with the reduction of GHG emissions from metal production, MSE also shows promise in reducing the production of low-value slags as demonstrated by the co-reduction of Cu and Fe from chalcopyrite as well as the reduction of Mo and Re[36]. However, due to the massive production scales and capital investment of these legacy extractive industries, the emerging technology needs to be economically competitive with the current paradigm.

Previous work by L. Rush in the Allanore research group details the techno-economic analysis of the MSE process for Cu production by the use of probabilistic discounted cash flows[4]. Analyzing the key performance indicators - Net Present Value (NPV), payback period and Internal rate of return (IRR), the use of MSE for Cu production was beneficial as compared to the traditional smelting techniques in the United States in most cases. Additionally, it was proven that the MSE facility could be integrated with intermittent power sources (renewable energy) and could leverage the high supply of low-cost electricity. The MSE facility shows potential to be selectively kept idle during periods of high-cost electricity and operate when the production exceeds the peak demand, to produce a low-cost product. This trade-off with the lower operating costs (cheap electricity) was observed to be beneficial despite the high capital costs required for larger capacity. This is especially attractive at a time when electricity sources are undergoing a paradigm shift with the increased adoption of variable, although clean power sources, e.g., wind and solar.

A similar analysis was performed for the heat produced in the cell due to the ohmic drop. The study revealed that there was always enough excess heat to maintain the cell temperature, melt the new cell feedstock and the higher levels of gangue (this would be tapped off as a slag layer to separate from the molten sulfides). This results in the capability to process low grade ores directly, while reducing the costs associated with mineral

processing. However, the amount of heat generated increases as the faradaic efficiency reduces. Hence, there is a trade-off between the grade of ore to be processed (low grade ore requiring more heat) versus the costs associated (lower faradaic efficiency would result in higher capital and operating expenses to maintain productivity).

Furthermore, it was concluded that continuous charging of the feedstock would yield better results in terms of operational time and feedstock depletion from the electrolyte.

Along with the techno-economic analysis, the MSE process has also been successfully demonstrated at laboratory scale for sulfides of Cu and high value impurities that occur in Cu ore such as molybdenum and rhenium sulfide. With the potential benefits observed in the case of non-ferrous metals, it can be hypothesized that MSE comes across as being a potential candidate for iron production.

2.4.3 Molten Sulfide Electrolysis for Fe production

As discussed with halide electrolytes being used to dissolve sulfides of copper or lead, FeS is an unsuitable feedstock due to its high electronic conductivity[24,38] and the inability of chloride systems to sustain ionic conduction for feedstock compositions as high as in Cu systems[26]. With the discovery of alkaline-earth metal and rare-earth metal sulfide electrolytes supporting ionic conduction[24,36], it was elucidated that these could be used as supporting electrolytes to perform faradaic reactions. Due to the underlying concept of 'like dissolves like', these sulfides have been observed to have high solubilities of the target metal sulfide feedstock as compared to their halide or aqueous counterparts[7,26]. Molten sulfide electrolysis for Fe is especially attractive due to the following reasons:

1. Unlike oxides[10,17], at the electrolysis conditions (high temperature and low partial pressure of oxygen) Fe is stable only in its +2 valence state as a sulfide[22]. This is expected to solve the multi-valency issue incurred in other electrolytic processes for Fe production.

2. The S_2 gas (thermodynamically the most stable form of sulfur at the operating temperatures of MSE) released at the anode (by the oxidation of the S^{2-} ion) can be captured and condensed and graphite serves as an inexpensive inert anode material[20,22,28,36].
3. Molten iron production at the cathode allows for a smooth integration into the present disruptive state-of-art BOFs utilising their high refining capabilities, without requiring their premature retirement.

Due to the high electrical conductivity of molten FeS[24,38] (1500 /ohm-cm) an appropriate amount of FeS is dissolved into the supporting electrolyte (BaS – La_2S_3) to mitigate the electronic conductivity[36]. The small electrical conductivity of BaS (0.01/ohm-cm) results in the ternary exhibiting a non-trivial amount of ionic conduction, as a function of composition and temperature. Although, exact measurement studies related to the share of ionic and electronic conduction in the above-mentioned electrolyte system are yet to be done.

The high decomposition potentials and thermal stability of the compounds of the supporting electrolyte (as studied previously with Cu_2S) make it resistant to degradation upon electrolysis at high temperatures. With necessary feedstock pre-treatments, oxygen contamination can be avoided, enabling compositional control of electrolyte for recirculation. The feedstock for Fe production using MSE could be either naturally present FeS[39,40] (abundant in shales, pyrite in igneous rocks, etc.) or oxide ores (e.g., hematite, magnetite) treated with sulfur in an exothermic 'sulfidation[19]' reaction. This process would thus allow the usage of lean Fe ores or low value Fe containing sources which have traditionally not been used (e.g., pyrite). Thus, the MSE route for iron production using oxide ores would involve two steps:

1. Conversion of the oxide ore to a sulfide feedstock in a sulfidation treatment
2. Molten sulfide electrolysis of iron sulfide dissolved in a supporting sulfide electrolyte to produce molten iron.

Figure 2.1 illustrates the process flowsheet for iron production via MSE in a Sankey diagram.

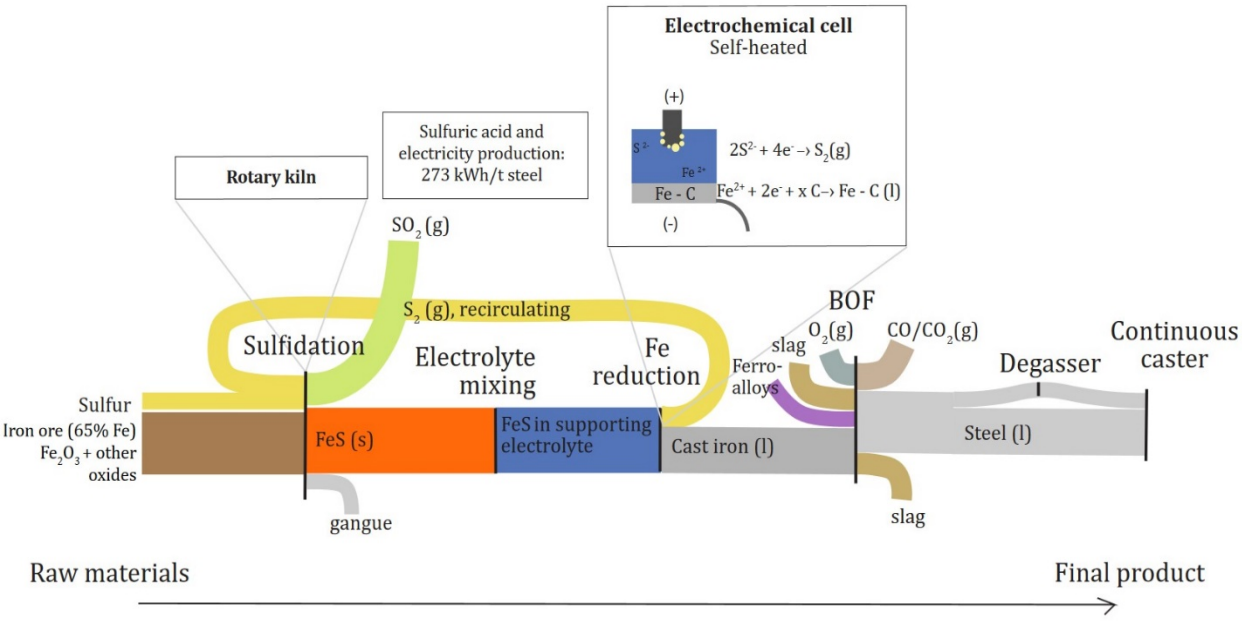

Figure 2.1 Sankey diagram depicting the process flowsheet for iron production via MSE

Once the FeS feedstock is prepared by treating the oxide ore with sulfur gas, it is then fed into the MSE cells containing a molten sulfide supporting electrolyte. As demonstrated earlier, the supporting electrolyte, a mixture of barium sulfide and lanthanum sulfide is found to support faradaic reactions as they are ionically conducting in nature, as compared to other sulfides which are semiconducting in nature[22,24]. About 10 wt.% of FeS is dissolved into the support electrolyte as equivalent ions of Fe^{+2} and S^{2-}. According to the sulfide Ellingham diagram[22] depicted below in **Figure 2.2**, both lanthanum and barium sulfides have exceedingly high decomposition potentials as compared to FeS. Thus, only FeS dissolved in the electrolyte gets electrolytically decomposed into Fe (deposited at the cathode) and elemental sulfur gas (evolved at the anode) according to the following reaction:

$$FeS\ (l) \rightarrow Fe\ (l) + \frac{1}{2}\ S_2(g) \quad \text{(in case of pure Fe production)} \qquad (2.6)$$

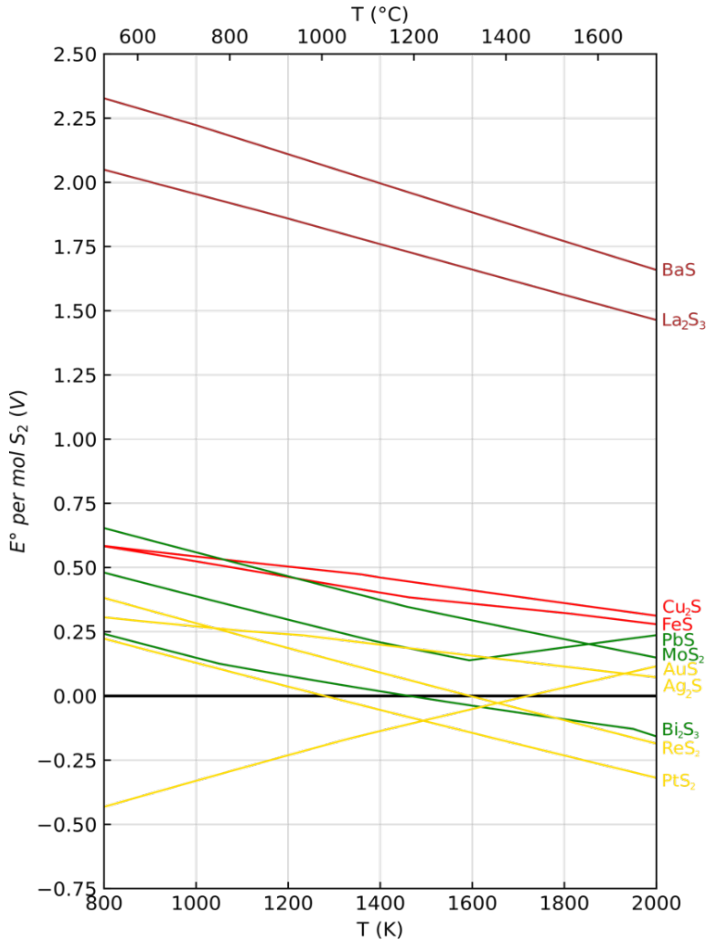

Figure 2.2 Sulfide Ellingham diagram with standard state decomposition voltage (adapted from K. Daehn) [22]

The following chapters discuss the mass-energy balance for molten and liquid Fe production via molten sulfide electrolysis starting from an oxide (i.e., hematite), experimental design to investigate the practical feasibility at lab scale and finally the results obtained.

2.5 References

(1) *World Steel in Figures 2022*. worldsteel.org. https://worldsteel.org/steel-topics/statistics/world-steel-in-figures-2022/ (accessed 2024-02-23).

(2) Contribution of Electricity to Materials Processing: Historical and Current Perspectives. *JOM* **2013**, *65* (2), 130–135. https://doi.org/10.1007/s11837-012-0538-3.

(3) Budevski, E. B. "Potentialities of New Technologies." Electrochemistry in Research and Development. **1984**.

(4) Rush, L. T. Integrative Approach to Metal Extraction and Electrification, 2021. https://hdl.handle.net/1721.1/140135.

(5) Allanore, A.; Lavelaine, H.; Valentin, G.; Birat, J. P.; Lapicque, F. Electrodeposition of Metal Iron from Dissolved Species in Alkaline Media. *J. Electrochem. Soc.* **2007**, *154* (12), E187. https://doi.org/10.1149/1.2790285.

(6) Lopes, D.; Quina, M.; Frade, J.; Kovalevsky, A. Prospects and Challenges of the Electrochemical Reduction of Iron Oxides in Alkaline Media for Steel Production. *Frontiers in Materials* **2022**, *9*, 1010156. https://doi.org/10.3389/fmats.2022.1010156.

(7) Allanore, A.; Feng, J.; Lavelaine, H.; Ogle, K. The Adsorption of Hematite Particles on Steel in Strongly Alkaline Electrolyte. *Journal of The Electrochemical Society* **2010**, *157*, E24–E30. https://doi.org/10.1149/1.3273198.

(8) Feynerol, V.; Lavelaine, H.; Marlier, P.; Pons, M.-N.; Lapicque, F. Reactivity of Suspended Iron Oxide Particles in Low Temperature Alkaline Electrolysis. *Journal of Applied Electrochemistry* **2017**, *47*, 1–12. https://doi.org/10.1007/s10800-017-1127-5.

(9) Allanore, A.; Lavelaine, H.; Valentin, G.; Birat, J. P.; Delcroix, P.; Lapicque, F. Observation and Modeling of the Reduction of Hematite Particles to Metal in Alkaline Solution by Electrolysis. *Electrochimica Acta* **2010**, *55* (12), 4007–4013. https://doi.org/10.1016/j.electacta.2010.02.040.

(10) Allanore, A. Features and Challenges of Molten Oxide Electrolytes for Metal Extraction. *Journal of the Electrochemical Society* **2014**, *162*, E13–E22. https://doi.org/10.1149/2.0451501jes.

(11) Sadoway, D. R. The Electrochemical Processing of Refractory Metals. *JOM* **1991**, 15–19.

(12) Sadoway, D. R. New Opportunities for Metals Extraction and Waste Treatment by Electrochemical Processing in Molten Salts. *Journal of Materials Research* **1995**, *10* (3), 487–492. https://doi.org/10.1557/JMR.1995.0487.

(13) Kim, H.; Paramore, J.; Allanore, A.; Sadoway, D. Electrolysis of Molten Iron Oxide with an Iridium Anode: The Role of Electrolyte Basicity. *Journal of The Electrochemical Society* **2011**, *158*, E101. https://doi.org/10.1149/1.3623446.

(14) Wang, D.; Gmitter, A.; Sadoway, D. Production of Oxygen Gas and Liquid Metal by Electrochemical Decomposition of Molten Iron Oxide. *Journal of The Electrochemical Society* **2011**, *158*. https://doi.org/10.1149/1.3560477.

(15) Yarlagadda, V. R. CONDUCTIVITY MEASUREMENTS OF MOLTEN METAL OXIDE ELECTROLYTES AND THEIR EVALUATION IN A DIRECT CARBON FUEL CELL (DCFC). **2011**.

(16) Allanore, A.; Yin, L.; Sadoway, D. A New Anode Material for Oxygen Evolution in Molten Oxide Electrolysis. *Nature* **2013**, *497*, 353–356. https://doi.org/10.1038/nature12134.

(17) Allanore, A. Electrochemical Engineering for Commodity Metals Extraction. *Electrochem. Soc. Interface* **2017**, *26* (2), 63. https://doi.org/10.1149/2.F05172if.

(18) Stinn, C.; Allanore, A. Selective Sulfidation of Metal Compounds. *Nature* **2022**, *602*. https://doi.org/10.1038/s41586-021-04321-5.

(19) Allanore, A.; Stinn, C. R. Selective Sulfidation and Desulfidation. US20210277531A1, September 9, 2021. https://patents.google.com/patent/US20210277531A1/en (accessed 2024-02-23).

(20) Townsend, C. P. Process for the Reduction of Ores. US815881A, March 20, 1906. https://patents.google.com/patent/US815881A/en (accessed 2024-02-23).

(21) Qu, J.; Chen, X.; Xie, H.; Gao, S.; Wang, D.; Yin, H. Anode Electrolysis of Sulfides. *Proceedings of the National Academy of Sciences* **2022**, *119* (31), e2202884119. https://doi.org/10.1073/pnas.2202884119.

(22) Daehn, K.; Stinn, C.; Rush, L.; Benderly-Kremen, E.; Wagner, M. E.; Boury, C.; Chmielowiec, B.; Gutierrez, C.; Allanore, A. Liquid Copper and Iron Production from Chalcopyrite, in the Absence of Oxygen. *Metals* **2022**, *12*, 1440. https://doi.org/10.3390/met12091440.

(23) Kartal, L.; Timur, S. Direct Electrochemical Reduction of Copper Sulfide in Molten Borax. *Int J Miner Metall Mater* **2019**, *26* (8), 992–998. https://doi.org/10.1007/s12613-019-1821-x.

(24) Sokhanvaran, S.; Lee, S.-K.; Lambotte, G.; Allanore, A. Electrochemistry of Molten Sulfides: Copper Extraction from BaS-Cu 2 S. *Journal of The Electrochemical Society* **2015**, *163*, D115–D120. https://doi.org/10.1149/2.0821603jes.

(25) Hoar, T. P.; Ward, R. G. The Production of Copper and Sulfur by the Electro-Decomposition of Cuprous Sulfide. *Trans. Inst. Min. Met. (London)* **1958**, No. 67, 393–410.

(26) Garbee, A. K.; Flengas, S. N. Electrical and Structural Properties of Metal Sulfides in Chloride Melts. *J. Electrochem. Soc.* **1972**, *119* (5), 631. https://doi.org/10.1149/1.2404276.

(27) Tan, M.; He, R.; Yuan, Y.; Wang, Z.; Jin, X. Electrochemical Sulfur Removal from Chalcopyrite in Molten NaCl-KCl. *Electrochimica Acta* **2016**, *213*. https://doi.org/10.1016/j.electacta.2016.07.088.

(28) Yin, H.; Chung, B.; Sadoway, D. R. Electrolysis of a Molten Semiconductor. *Nat Commun* **2016**, *7* (1), 12584. https://doi.org/10.1038/ncomms12584.

(29) Ge, X.; Wang, X.; Seetharaman, S. Copper Extraction from Copper Ore by Electro-Reduction in Molten CaCl2–NaCl. *Electrochimica Acta* **2009**, *54* (18), 4397–4402. https://doi.org/10.1016/j.electacta.2009.03.015.

(30) *Polarization Behavior of the Nickel Electrode in Molten Sulfides - IOPscience*. https://iopscience.iop.org/article/10.1149/1.2115557 (accessed 2024-02-23).

(31) Bruce, P. G.; Freunberger, S. A.; Hardwick, L. J.; Tarascon, J.-M. Erratum: Li–O2 and Li–S Batteries with High Energy Storage. *Nature Mater* **2012**, *11* (2), 172–172. https://doi.org/10.1038/nmat3237.

(32) Bruce, P. G.; Hardwick, L. J.; Abraham, K. M. Lithium-Air and Lithium-Sulfur Batteries. *MRS Bulletin* **2011**, *36* (7), 506–512. https://doi.org/10.1557/mrs.2011.157.

(33) Lv, T.; Chen, D.; Huang, M. Quasiparticle Band Structures of BaO and BaS. *Journal of Applied Physics* **2006**, *100* (8), 086103. https://doi.org/10.1063/1.2358413.

(34) Wu, Y. *Am. Chem. Soc.* **2008**, *8*, 2551.

(35) Enderby, J. E.; Barnes, A. C. A Theory for the Electrical Conductivity of Molten Mixtures of Sulfides and Halides. *J. Electrochem. Soc.* **1987**, *134* (10), 2483. https://doi.org/10.1149/1.2100226.

(36) Sahu, S.; Chmielowiec, B.; Allanore, A. Electrolytic Extraction of Copper, Molybdenum and Rhenium from Molten Sulfide Electrolyte. *Electrochimica Acta* **2017**, *243*. https://doi.org/10.1016/j.electacta.2017.04.071.

(37) Kaptay, G. The Conversion of Phase Diagrams of Solid Solution Type into Electrochemical Synthesis Diagrams for Binary Metallic Systems on Inert Cathodes. *Electrochimica Acta* **2012**, *60*, 401–409. https://doi.org/10.1016/j.electacta.2011.11.077.

(38) Savelsberg, W. *Ztschr. Elektrochem.* **1940**, No. 46, 379.

(39) Hu, G.; Dam-Johansen, K.; Wedel, S.; Hansen, J. P. Decomposition and Oxidation of Pyrite. *Progress in Energy and Combustion Science* **2006**, *32* (3), 295–314. https://doi.org/10.1016/j.pecs.2005.11.004.

(40) Bhargava, S.; Garg, A.; Subasinghe, N. In Situ High-Temperature Phase Transformation Studies on Pyrite. *Fuel* **2009**, *88*, 988–993. https://doi.org/10.1016/j.fuel.2008.12.005.

Chapter 3

Thermodynamic framework for iron sulfide electrolysis

As described in the previous chapter, the process flow for molten sulfide electrolysis to produce iron from a primary feedstock, predominantly an oxide ore, (usually hematite), consists of two important steps:

1. Feedstock preparation through sulfidation of the iron oxide ore

$$4\ Fe_2O_3\ (s) + 7\ S_2(g)\ \rightarrow 8\ FeS\ (s) + 6\ SO_2(g) \tag{3.1}$$

2. Molten sulfide electrolysis to produce molten iron

$$FeS\ (l) + x\ C \rightarrow Fe - 4.3\ wt.\%\ C\ (l) + \frac{1}{2}\ S_2(g) \tag{3.2}$$

Once the scientific feasibility of a process is realized, it is important to determine the amount of energy needed for driving the reaction and get an insight of the efficiency governing parameters to realize the benefits of the process. This chapter discusses the mass – energy balance for 1-ton of the product and compares it to the energy requirements of the conventional and alternative steel making technologies, specifically molten oxide electrolysis[1,2]. The calculation presented here is based of the work of Fonseca et. al[3], which provides a theoretical framework for estimating the minimum energy requirements in an electrolytic cell along with including the effect of inefficiencies in the real industrial world. No kinetic considerations are made for building the thermodynamic model. It is assumed that there are no kinetic limitations in the electrolysis due to the high temperatures involved. It also explains thermodynamically why reduction to produce metal from a sulfide is energetically favorable as compared to an oxide, especially in the case of iron, with the help their Gibbs energy values for reduction[16]. A detailed calculation of the cell potentials for the molten sulfide electrolysis is carried out and presented for different conditions. Furthermore, the factors affecting the choice of the supporting electrolyte's composition are also discussed in terms of the electrolytic decomposition diagram.

3.1 Mass - Energy Balance

Prior similar work done for Fe production from Fe_2O_3 at 1600° C via the MOE process results in an energy requirement of ~3600 kWh/ton Fe, including up to 40% practical heat losses at high temperature. The MOE process yields energy savings as compared to the BF-BOF route which requires ~4800 kWh/ton steel. However, this energy balance is highly dependent on the faradaic inefficiencies. In an electrochemical system, faradaic inefficiencies can be resulted due to the following:

1. Re-oxidation of the metallic species: This reaction results in a release of energy (also known as the enthalpy of re-oxidation) in the cell, contributing positively to the heat

balance. However, it is offset by the energy (thermal and chemical) which was initially spent to reduce the oxidized compound, which is lost upon reversal to metal product.

2. Electronic conduction: Some electrons may electronically conduct through the electrolyte without taking part in faradaic reactions.
3. Partial reduction of the metallic ions: This is a common phenomenon observed in metallic species which exist in multiple valence states. In the case of Fe_2O_3 reduction, this partial reduction affects the heat balance as with Fe^{+3} reduced to Fe^{+2} to form FeO, there is a decrement in the chemical energy required for charge to flow.

Each of the above inefficiencies negatively affect the cell potential, however, the effect of faradaic inefficiency due to re-oxidation is the highest[3]. Thus, having knowledge of the possible inefficiencies in the systems allows us to optimize the energy consumption by controlling the required parameters.

A key contributor of the heat balance of an electrolysis cell arises from the relation:

$$U_{ohm} = \frac{jg}{k} \tag{3.3}$$

where j is the current density, g is the inter-electrode gap and k is the conductivity of the electrolyte, the levers to control the ohmic voltage drop.

The required production rate determines the current density; the inter-electrode gap needs to be optimized in order to limit the ohmic drop while also facilitating efficient removal of the products. Hence, the electrical conductivity of the electrolyte becomes a significant parameter to control the ohmic drop and hence the heat generated. The MOE process exploits this parameter in using the high ohmic drop (generated by the low conductivity of the oxide electrolyte) to maintain the electrolyte in the molten state and produce liquid Fe at temperatures around 1600° C.

Heat management at such high temperatures already is extremely challenging, however, the liquid Fe, with 3000 ppm oxygen[4](minimum solubility limit at 1600° C), only contains limited superheat required for further refining.

The C-Fe interaction not only results in the increased strength of steel but also is fundamental to the processing and refining of steel. The presence of carbon is critical in

controlling the chemistry of iron, as the solubility of oxygen in molten iron increases with reducing carbon. Moreover, at such high temperatures, the refractory wear is much higher while the operational flexibility is lower due to the requirement of maintaining the reactor temperature to avoid electrolyte freeze-out.

Molten sulfide electrolysis not only eliminates any direct carbon emissions from the iron ore reduction process, but results in producing a molten iron product. The production of molten iron significantly reduces the operating temperature requirements down to 1300° C. Depending on the carbon content, molten iron exists between 1147° C and 1538° C. The operating temperature proposed above assumes the carbon content to be 4.3 wt.%., similar to BF hot metal composition, including a 100° C superheat for further processing. This lower temperature enables in principle, easier heat management, refractory performance, and operational flexibility. The direct production of molten iron at 1600°C is not feasible via MOE without carbo-thermically reducing the iron oxide in the electrolyte.

Additionally, apart from lower operating temperatures, molten sulfide electrolysis of FeS offers more rationale to electrifying Fe production.

1. At 1300° C, the only stable valence state of Fe as a sulfide is the Fe^{+2}. This eliminates the issue of partial reduction of the target ions.
2. The Gibbs energy for decomposition is less for the sulfide than the oxide due to the requirement of only 2 electrons to be reduced in FeS as compared to 3 in Fe_2O_3. Moreover, the sulfur-iron bond is weaker as compared to the oxygen-iron bond. As evidence, the Gibbs energy values for reduction from oxide and sulfide are given below. At 1600° C, the amount of chemical work required to decompose FeS to pure liquid Fe is 300kWh/ ton Fe as compared to 900 kWh/ ton Fe.
3. No side reactions such as reduction of sulfides of La or Ba[ii] were seen in previous experimental work with the molten sulfide electrolysis of chalcopyrite to yield copper and molten iron, along with high faradaic efficiencies.

Along with the benefits to process electrochemically, MSE offers other advantages such as:

[ii] Decomposition potential of BaS and La_2S_3 at 1300 ° C is 1.9 V and 1.5 V respectively as compared to 0.36 V for FeS

1. Inert, stable, cheap, readily available graphite anode[5]
2. Ability to process low-grade oxide ores after sulfidation treatment[iii] and low-value feedstock such as pyrite or shale for iron production.
3. Possibility of carbon additions to the Fe produced at the molten iron cathode (graphite as the current collector), to lower the melting point of the product. The production of molten iron would facilitate the smooth integration with the existing, highly productive BOF and continuous caster.
4. S_2 being the only by-product of the reaction could be reused in the sulfidation, while the $SO_2(g)$ released in the sulfidation possesses potential for sulfuric acid production (highly exothermic processes) and subsequent electricity generation (210 kWh/ MT of acid[7])

The techno-economic analysis performed previously for Cu production via MSE[7] (see L. Rush thesis for reference) explores the different by-product handling alternatives. Sulfur could be sold directly or combusted to generate revenue, in the form of sulfuric acid and electricity generation from the heat released. It was concluded, in agreement with the current S_2 - H_2SO_4 market dynamics that in the USA, directly selling sulfur was more cost efficient than combusting it. Based on the techno-economic conclusions of the previous work by L. Rush for Cu production by MSE, it can be anticipated that when directly starting with a sulfide feedstock such as FeS, producing iron and sulfur can lead to cost and energy saving benefits while producing no direct carbon emissions[7]. When starting from the oxide feedstock, such as hematite, the sulfur produced in MSE can be recirculated in the sulfidation circuit.

In the section below, detailed mass and energy calculations are performed specific to the system discussed in this work, iron production by MSE. The underlying assumptions are stated below. It should be noted that the effect of reaction kinetics and impurities/gangue handling are out of scope presently and would need a highly detailed and dedicated framework.

[iii] Selective sulfidation of iron oxide from bauxite residue [6] (or) red mud demonstrated by Marden and Stinn et.al

For the mass balance calculations, the following assumptions are made:

1. Production = 1 ton of molten iron
2. Continuous operation of both, the sulfidation reactor and the MSE cells
3. Composition of the molten iron = Fe - 4.3 wt.% carbon, a composition similar to that of the hot metal [8], the current product of the blast furnace.

To prepare the feedstock for molten sulfide electrolysis, iron ore (primarily hematite ore) is treated with sulfur in a sulfidation reaction[9,10] at 1000°C to convert the Fe_2O_3 present in the ore into FeS (from **equation 3.1**) in a spontaneous exothermic process.

$$4\ Fe_2O_3\ (s) + 7\ S_2(g)\ \rightarrow 8\ FeS\ (s) + 6\ SO_2(g) \qquad \text{(from equation 3.1)}$$

$$\Delta H^\circ{}_{1000\,^\circ C} = -131.9\ KWh\ /ton\ Fe \quad ;\ \Delta G^\circ{}_{1000^\circ C} = -192.82\ KWh/\ ton\ Fe$$

0.96 tons of sulfur would be needed to convert 1.47 tons of iron ore (65wt.% Fe), i.e. 1.37 tons of Fe_2O_3 and 0.1 tons of gangue which is generally composed of silica, alumina, etc. into 1.5 tons of FeS. This is the required amount to produce one ton of molten iron, Fe containing 4.3 wt.% carbon. The gangue is unreactive with sulfur in the above-mentioned conditions[10,11]. The SO_2 (g) along with the excess amount of heat released from the reactor is captured and utilized to produce sulfuric acid in an acid plant and generate electricity, a minimum of 210 kWh/ ton of acid. The excess heat in the reactor will also be used to heat the reactants to the reaction temperature, thus minimizing the fuel requirement. **Figure 3.1** depicts the mass balance to produce 1 metric ton of molten iron through MSE starting from an oxide feedstock.

The FeS feedstock is then fed into the MSE cells (up to 10 wt.%) containing a molten sulfide electrolyte, a mixture of barium sulfide and lanthanum sulfide, to support faradaic reactions[5,12]. The high decomposition potentials of lanthanum and barium sulfides as compared to FeS leads to the electrolytic decomposition of only the dissolved FeS. As a result, Fe is deposited at the cathode and elemental sulfur gas evolved at the anode according to the final reaction:

$$FeS\ (l) \rightarrow Fe\ (l) + \frac{1}{2}\ S_2(g)\ \text{(in case of pure Fe production)} \qquad (3.4)$$

$\Delta H°_{1600\,℃} = 691.47\ kWh\ /ton\ Fe$; $\Delta G°_{1600℃} = 294.91\ kWh\ /ton\ Fe$

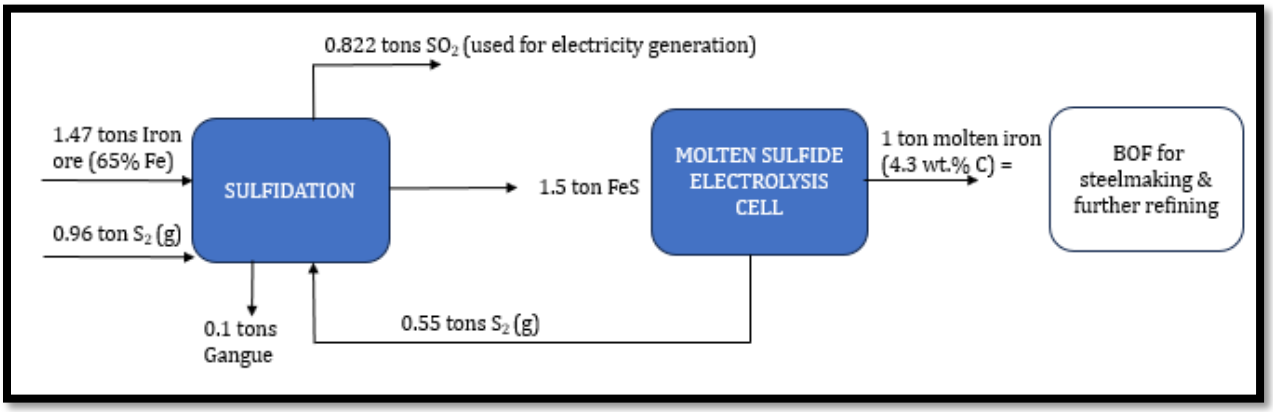

Figure 3.1 Process flow chart depicting the mass balance to produce 1 metric ton molten iron

In comparison, the enthalpy, and Gibbs energy change for reduction of iron oxide directly to metallic Fe, as is carried out in the molten oxide electrolysis process, is higher than reduction from sulfides. Moreover, energetically, due to the stability of Fe^{+2} ion, FeS offers fundamental advantages for the electrification of iron production.

$$Fe_2O_3\ (s)\ \rightarrow 2Fe(l) + \frac{3}{2}O_2(g)\ \text{(in case of pure liquid Fe production)}\quad (3.5)$$

$\Delta H°_{1600\,℃} = 2077.9\ kWh\ /ton\ liquid\ Fe$;

$\Delta G°_{1600℃} = 865.6\ kWh/ton\ liquid\ Fe$

$$FeS\ (l) + x\ C \rightarrow Fe - 4.3\ wt.\%\ C\ (l) + \frac{1}{2}\ S_2(g)\ \text{; molten iron}\quad \text{(from equation 3.2)}$$

$\Delta H°_{1300\,℃} = 776.99\ kWh/ton\ molten\ iron$; $\Delta G°_{1300℃} = 316.61$ kWh/ton $molten\ iron$

The sulfur released is recirculated into the sulfidation circuit, forming a closed loop system. Since the S_2 released in the MSE process is captured and fed back into the system, an additional of only 0.4 tons will be needed by the system in consecutive cycles in comparison to the 0.96 ton of sulfur required for the initial sulfidation of iron oxide. As shown in **Figure 3.1,** the process generates at least 0.1 tons of gangue from the iron ore (considering high quality iron ore with 65% Fe). However, the impact of gangue minerals and their subsequent handling is at present out of scope of this work.

For the energy calculations of the electrolysis, the following assumptions are made:

1. The reactor (MSE cell) is assumed to be isothermal and in equilibrium state.
2. The electrolytic cell is considered as an autothermal reactor.
3. The MSE cell is an open system. This is ensured by the flow of a carrier gas to transport the product S_2 gas away from the anode to prevent any back reaction.
4. The cell is assumed to be at steady state, i.e., the composition at the electrolyte and electrode is assumed to be constant throughout the electrolysis. This ensures a stable decomposition potential, hence simplifies the calculation of the energy requirement.
5. The decomposition potential is unaffected by -
    5.1 *Anode:* Graphite is found to be stable and inert in sulfide melts and hence is used as the anode material in the MSE cell.
    5.2 *Components of the supporting electrolyte:* Effect of the interaction between the different ionic species present in the electrolyte are ignored for the sake of this work. This assumption is partially justified considering the large difference in the decomposition potential of La and Ba sulfides relative to FeS.
6. The faradaic efficiency of the electrolysis process is taken to be 90 % (from previous MSE experiments for Cu production[5,13,14]). The possibility of electronic conduction in the electrolyte resulting in some electrons not participating in faradaic reactions could explain the faradaic inefficiency.
7. Since the reactor is close to the melting point of molten iron, heat losses owing to the loss of hot gases and effect of conduction, convection and radiation result in heat inefficiencies. These heat losses are highly contingent upon the reactor temperature of operation. In the calculations below, a conservative 40% heat loss as in any advanced high temperature electrolysis cell is assumed, similar to MOE energy calculations[15].
8. Any kinetic limitations, such as mass transfer limitations in the bulk electrolyte are ignored, assuming a high concentration of the reactant species at the electrodes due to increased level of mixing, as also done in previous studies by L. Rush[7].
9. Any impurity present in the feedstock is assumed not to affect the thermo-energetic balance.

At an operating temperature of 1300° C, the practical heat efficiency for a hypothetical electrolytic reactor is assumed to be 66.8% (see Maria Paula Fonseca's work for reference[3]). The logarithmic relation (given below, used directly from the work of Angarita Fonseca et.al) to calculate the heat efficiency is derived by fitting practical industrial data for different electrolytic processes in operation.

$$Heat\ efficiency = 26.064 \ln(T\ in\ K) - 125 \tag{3.6}$$

The model considers the current technological thermal limitations in industrial electrolytic metal extraction. However, for the case of making realistic assumptions of heat loss, a 40% loss of the heat (as in industrial Al electrolysis) resulting from the ohmic (IR) drop (Joule heat generated) is considered in the calculations below. It should be noted that the loss of heat should be accounted only for the heat generated by the IR drop, as is done in the calculations presented below.

3.1.1 Enthalpy and energy balance for pure liquid Fe production at 1600 °C

The following calculation[3] depicts the enthalpy and energy balance to produce pure liquid Fe at 1600 °C. For reference, the melting point of Fe is 1539° C[16], so at 1600° C, we can expect a superheated liquid iron product, ensuring ability to cast the product out of the cell.

$$Enthalpy\ of\ FeS\ (s\ at\ 25\ °C) = -104560\ J/mol \tag{3.7}$$

$$Enthalpy\ of\ FeS\ (l\ at\ 1600\ °C) = 29990.9\ J/mol \tag{3.8}$$

$$\Delta H°\ FeS\ (s\ at\ 25\ °C\ ) \rightarrow FeS\ (l\ at\ 1600\ °C) = 134550.9\ J/mol \tag{3.9}$$

$$\Delta H°_{rxn@1600°C}\ FeS\ (l) \rightarrow Fe\ (l) + \frac{1}{2}\ S_2\ (g) = 139014.1\ J/mol\ Fe \tag{3.10}$$

$$Total\ enthalpy\ needed\ per\ ton\ of\ liquid\ Fe\ produced\ = \mathbf{1360.74}\ \frac{\boldsymbol{kWh}}{\boldsymbol{ton\ Fe}} \tag{3.11}$$

$$U_{cell} = U_{chem} + U_{ohmic} + U_{over\ voltage}$$[iv] (3.12)

$$\Delta G°_{rxn\ @1600°C} = 59295.1\ J\ /mol\ Fe \quad (3.13)$$

$$U_{chem} = \frac{-\Delta G}{nF}\ ; F = Faraday's\ constant\ , n = no.of\ electrons\ transferred \quad (3.14)$$

$$U_{chem} = -0.307\ V \quad (3.15)$$

$$Amount\ of\ chemical\ work = \Delta G°_{rxn\ @1600°C} = 294.94\ kWh/ton\ Fe \quad (3.16)$$

$$\Delta G = \Delta H - T\Delta S \quad (3.17)$$

$$Amount\ of\ energy\ supplied\ to\ provide\ heat = \Delta H - \Delta G = 1065.8\ kWh/ton\ Fe \quad (3.18)$$

$$U_{ohmic} = \frac{-(\Delta H - \Delta G)}{nF} = -1.11\ V \quad (3.19)$$

$$U_{cell} = \mathbf{-1.417V} \quad (3.20)$$

$$Total\ electrical\ energy\ (for\ chemical\ work\ and\ heat) = 1360.74\ kWh/ton\ Fe \quad (3.21)$$

$$Electrical\ energy\ required\ including\ 40\%\ heat\ loss = \mathbf{1787.06\ kWh/ton\ Fe} \quad (3.22)$$

Figure 3.2 and **3.3** below depict the variation of enthalpy and Gibbs energy change respectively, with the temperature for sulfidising iron oxide to FeS. The sulfidation is performed at a 1000°C to overcome any kinetic and mass transport limitations, while also keeping the enthalpy requirements low.

[iv] $U_{over\ voltage}$ is neglected in this calculation for simplicity

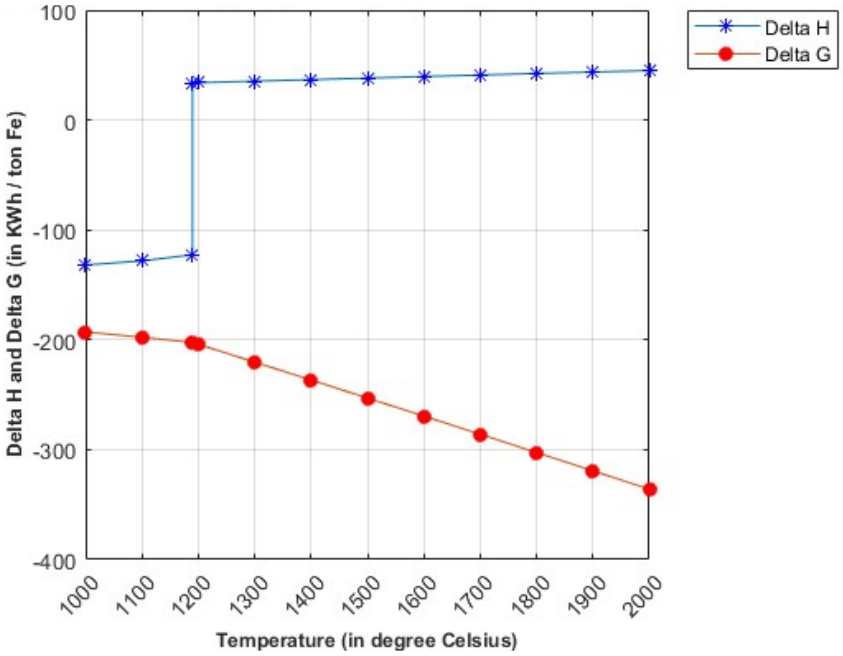

Figure 3.2 Plot depicting the variation of enthalpy and Gibbs energy change with the temperature for sulfidising iron oxide to FeS to electrolytically produce one ton of Fe[v]

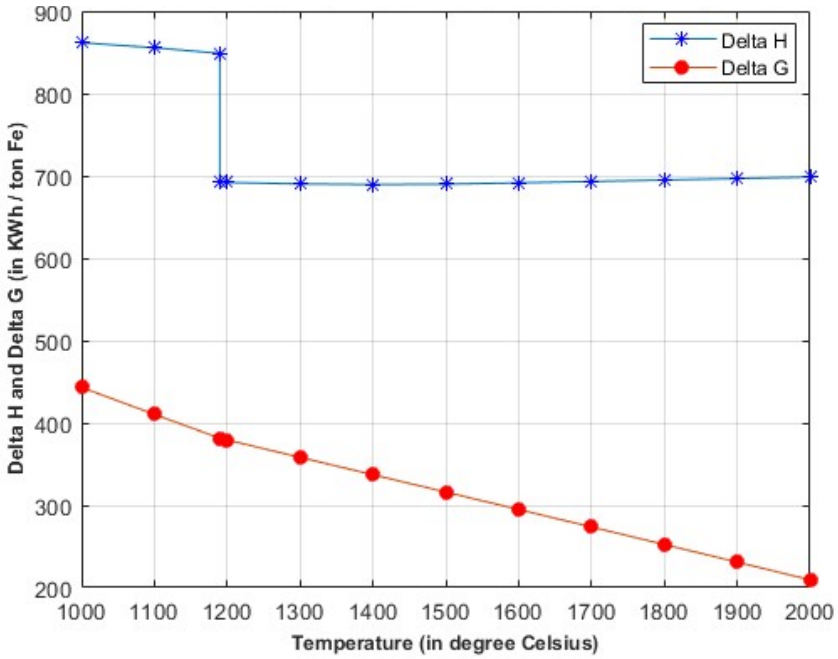

Figure 3.3 Plot depicting the variation of enthalpy change and Gibb's free energy change with the temperature in kWh/ ton of Fe produced

v The change of slope indicates the fusion of FeS at 1194 °C

3.1.2 Enthalpy and energy balance for pure Fe production at 1300°C

The following depicts the enthalpy and energy balance to produce pure Fe at 1300° C. However, this calculation is also meant for comparison of the effect of temperature and composition, as at 1300 °C, without any alloying element, the product expected is pure solid iron.

$$Enthalpy\ of\ FeS\ (l\ at\ 1300\ °C) = 11225.6\ J/mol \quad (3.23)$$

$$\Delta H°\ FeS\ (s\ at\ 25\ °C) \rightarrow FeS\ (l\ at\ 1300\ °C) = 115785.6\ J/mol \quad (3.24)$$

$$\Delta H°_{rxn\ @1300°C}\ FeS\ (l) \rightarrow Fe\ (s) + \frac{1}{2}\ S_2\ (g) = 124955.9\ J/mol\ Fe \quad (3.25)$$

$$Total\ enthalpy\ needed\ per\ ton\ of\ Fe\ produced\ = \mathbf{1197.47\ kWh/ton\ Fe} \quad (3.26)$$

$$\Delta G°_{rxn\ @1300°C}\ = 70207.4\ J\ /mol\ Fe \quad (3.27)$$

$$U_{chem}\ =\ -0.364\ V \quad (3.28)$$

$$U_{ohmic}\ =\ -0.88\ V \quad (3.29)$$

$$U_{cell}\ =\ \mathbf{-1.24\ V} \quad (3.30)$$

$$Total\ electrical\ energy\ (for\ chemical\ work\ and\ heat) =\ 1197.47\ kWh/ton\ Fe \quad (3.31)$$

$$Electrical\ energy\ required\ including\ 40\%\ heat\ loss =\ \mathbf{1536.77\ kWh/ton\ Fe} \quad (3.32)$$

3.1.3 Enthalpy and energy balance for molten iron (Fe – 4.3 wt.% C) production at 1300°C

The following is the enthalpy and energy balance to produce molten iron at 1300° C. For reference, the melting point of molten iron of the given composition (Fe – 4.3 wt.% C) is 1147° C[8], so at 1300° C, we can expect a superheated molten iron product, with very good flowability. The advantage of producing molten iron comes with significantly reduced processing temperature, which decreases the complexity of heat management and prevents

excessive refractory wear. Apart from reducing the melting point of iron by alloying, carbon also behaves as a powerful agent to control the chemistry of iron, e.g., the solubility of O in Fe increases as C decreases[17]. This is especially crucial for refining the molten iron in the BOF for steel making.

$$Enthalpy\ of\ C\ (s\ at\ 25\ ℃) = 0\,\frac{J}{mol} \tag{3.33}$$

$$Enthalpy\ of\ C\ (s\ at\ 1300\ ℃) = 24977.8\,\frac{J}{mol} \tag{3.34}$$

$$\Delta H°\ C\ (s\ at\ 25\ ℃) \rightarrow\ C\ (s\ at\ 1300\ ℃) = 24977.8\,\frac{J}{mol} \tag{3.35}$$

$$\Delta H_{mix@1300℃}\,95.7\ g\ Fe\ (s) + 4.3\ g\ C\ (s) \rightarrow 100g\ Fe - 4.3\ wt.\%\ C\ (l) = 33778.5\ J \tag{3.36}$$

$$Total\ enthalpy\ per\ ton\ of\ molten\ iron = \mathbf{1264.44\ kWh\ /\ ton\ molten\ iron} \tag{3.37}$$

$$\Delta G°_{rxn\ @1300℃}\ FeS\ (l) \rightarrow Fe\ (l) + \frac{1}{2}\ S_2\ (g) = 70207.4\ J/mol\ Fe \tag{3.38}$$

$$\Delta G_{mix@1300℃}\,95.7\ g\ Fe\ (s) + 4.3\ g\ C(s) \rightarrow 100g\ Fe - 4.3\ wt.\%\ C\ (l) =\ -6299.17\ J \tag{3.39}$$

$$\Delta G_{rxn@1300℃}\,FeS + 4.3\ wt.\%\ C \rightarrow Fe - 4.3\ wt.\%\ C + \frac{1}{2}S_2(g) = 316.7\,\frac{kWh}{ton\ molten\ iron} \tag{3.40}$$

$$U_{chem}\ =\ -0.345\ V \tag{3.41}$$

$$U_{ohmic}\ =\ -1.03\ V \tag{3.42}$$

$$U_{cell}\ =\ \mathbf{-1.376V} \tag{3.43}$$

$$Total\ electrical\ energy\ (for\ chemical\ work\ and\ heat) =\ 1264.44\,\frac{kWh}{ton\ molten\ iron} \tag{3.44}$$

$$Electrical\ energy\ required\ including\ 40\%\ heat\ loss =\ \mathbf{1643.53}\,\frac{\mathbf{kWh}}{\mathbf{ton\ molten\ iron}} \tag{3.45}$$

$$Electrical\ energy\ required\ including\ 40\%\ heat\ loss^{vi} =\ \mathbf{1717.38\ kWh/ton\ Fe} \tag{3.46}$$

It can be observed that addition of carbon does not lead to any reduction in the energy required, i.e., producing solid pure Fe at 1300° C requires less energy than producing molten

[vi] Per ton Fe (1.045-ton molten iron) calculation only to compare with pure Fe production calculation in section 3.1.1 and 3.1.2

iron (Fe-C alloy) production. This is because the enthalpy of mixing Fe and C is not sufficient enough to offset the enthalpy of fusion of Fe and that required to heat up the carbon to reaction temperature. Nevertheless, direct production of molten iron is better than solid Fe production, as this allows semi-continuous metal recovery from the cell and avoids an additional facility to melt the solid product. Additionally, with respect to integration within the existing steel making facilities, production of molten iron is the most suitable.

Figure 3.4 below depicts the variation of enthalpy change and Gibbs energy change with the temperature for the electrolysis reaction to produce one ton of molten iron.

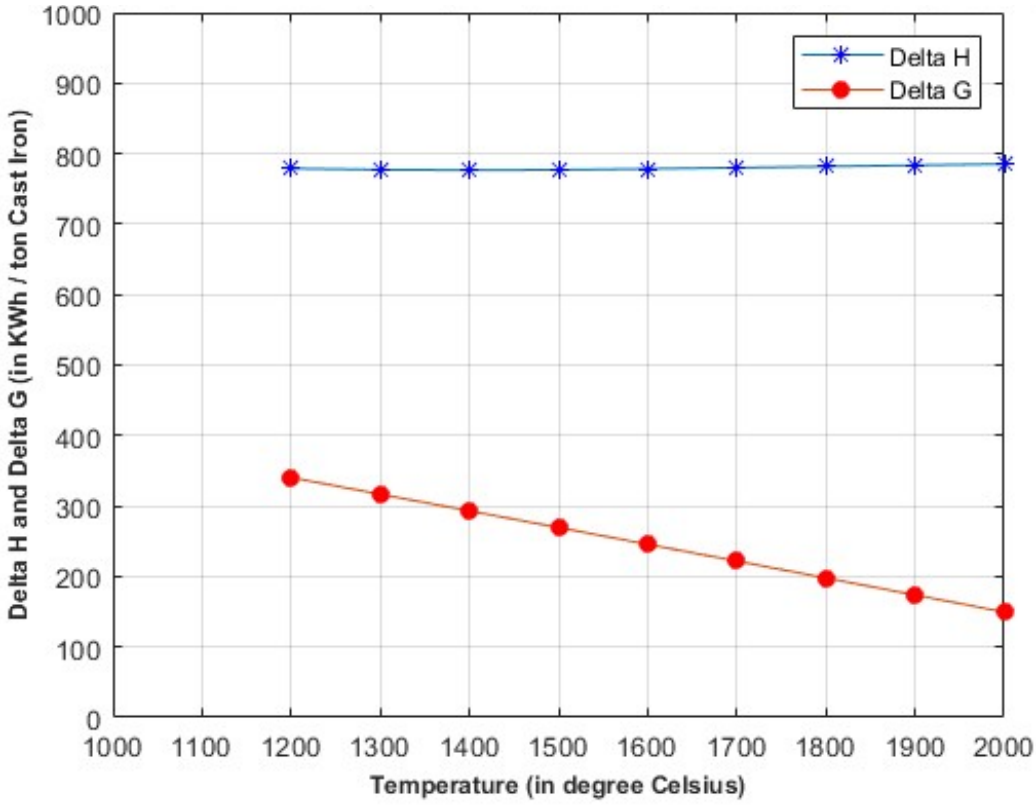

Figure 3.4 Plot depicting the variation of enthalpy change and Gibbs energy change with the temperature in kWh/ ton of molten iron produced

3.1.4 Enthalpy and energy balance for molten iron (Fe – 4.3 wt.% C) production at 1600°C

The following depicts the enthalpy and energy balance to produce molten iron (Fe – 4.3 wt.% C) at 1600° C. Given, the melting point of molten iron of the given composition (Fe – 4.3 wt.% C) is 1147° C, we can expect at 1600° C a highly superheated molten iron product. However, this calculation is also meant only for comparison of the effect of temperature and composition, as at 1600° C, the molten iron has a super heat higher than 400° C, which is completely unnecessary and a waste of energy.

$$Enthalpy\ of\ C\ (s\ at\ 1600\ ℃) = 32323.7 \frac{J}{mol} \quad (3.47)$$

$$\Delta H°\ C\ (s\ at\ 25\ ℃)\ \rightarrow\ C\ (s\ at\ 1600\ ℃)\ = 32323.7 \frac{J}{mol} \quad (3.48)$$

$$\Delta H_{mix@1600℃}\ 95.7\ g\ Fe\ (s) + 4.3\ g\ C\ (s) \rightarrow 100g\ Fe - 4.3\ wt.\%\ C\ (l) = 10702.4\ J \quad (3.49)$$

$$Total\ enthalpy\ to\ produce\ molten\ iron\ \ at\ 1600℃ = \mathbf{1363.88} \frac{\boldsymbol{kWh}}{\boldsymbol{ton\ molten\ iron}} \quad (3.50)$$

$$\Delta G°_{rxn\ @1600℃}\ FeS\ (l) \rightarrow Fe\ (l) + \frac{1}{2}\ S_2\ (g) = 59288.7\ J/mol\ Fe \quad (3.51)$$

$$\Delta G_{@1600℃}\ 95.7\ g\ Fe\ (s) + 4.3\ g\ C(s) \rightarrow 100g\ Fe - 4.3\ wt.\%\ C\ (l) = -13{,}159.7\ J \quad (3.52)$$

$$\Delta G_{rxn@1600℃}\ FeS + 4.3\ wt.\%\ C \rightarrow Fe - 4.3\ wt.\%\ C + \frac{1}{2} S_2(g) = 245.67 \frac{kWh}{ton\ molten\ iron} \quad (3.53)$$

$$U_{chem}\ =\ -0.267\ V \quad (3.54)$$

$$U_{ohmic}\ =\ -1.217\ V \quad (3.55)$$

$$\boldsymbol{U_{cell}\ =\ -1.484\ V} \quad (3.56)$$

$$Total\ electrical\ energy\ (for\ chemical\ work\ and\ heat) =\ 1363.88 \frac{kWh}{ton\ molten\ iron} \quad (3.57)$$

$$Electrical\ energy\ required\ including\ 40\%\ heat\ loss =\ \mathbf{1811.164} \frac{\boldsymbol{kWh}}{\boldsymbol{ton\ molten\ iron}} \quad (3.58)$$

$$Electrical\ energy\ required\ including\ 40\%\ heat\ loss^{vii} = \mathbf{1892.54\ kWh/ton\ Fe} \quad (3.59)$$

3.2 Summary

Using a thermodynamic framework, including the mass and energy balance for the MSE process, allows one to understand the expected influence of temperature and composition of the liquid metal on the minimum energy requirements. In this chapter, detailed calculations for both, pure liquid iron and molten iron (alloy of Fe and 4.3 wt.% carbon) are presented. It is found that MSE has lower enthalpy and electrical energy requirement as compared to other electrolytic processes for steel production, specifically molten oxide electrolysis, and is an especially attractive option for molten iron production. This is because of the lower temperature requirements for molten iron production (~ 1300° C), as compared to pure liquid Fe production at ~ 1600° C (minimum requirement). The wide difference in processing temperature facilitates better heat management of the sulfide melt, reduces refractory wear, and allows more flexibility in the process.

Moreover, the faradaic efficiency of the MSE process, as seen from previous studies with copper production show a 90% efficiency, hence the following calculations use a conservative figure of 90%. Thus, including 40% of heat losses in the MSE reactor, the practical energy requirements of MSE are about **52.8 %** less, where molten iron production at 1300° C consumes **1717.38** kWh/ton Fe; producing 1.045-ton of molten iron compared to molten oxide electrolysis at around 3640 kWh/ ton liquid Fe. **Figure 3.6** shown below depicts the energy requirements of various steelmaking processes for comparison.

[vii] Per ton Fe (1.045-ton molten iron) calculation only to compare with pure Fe production calculation in section 3.1.1 and 3.1.2

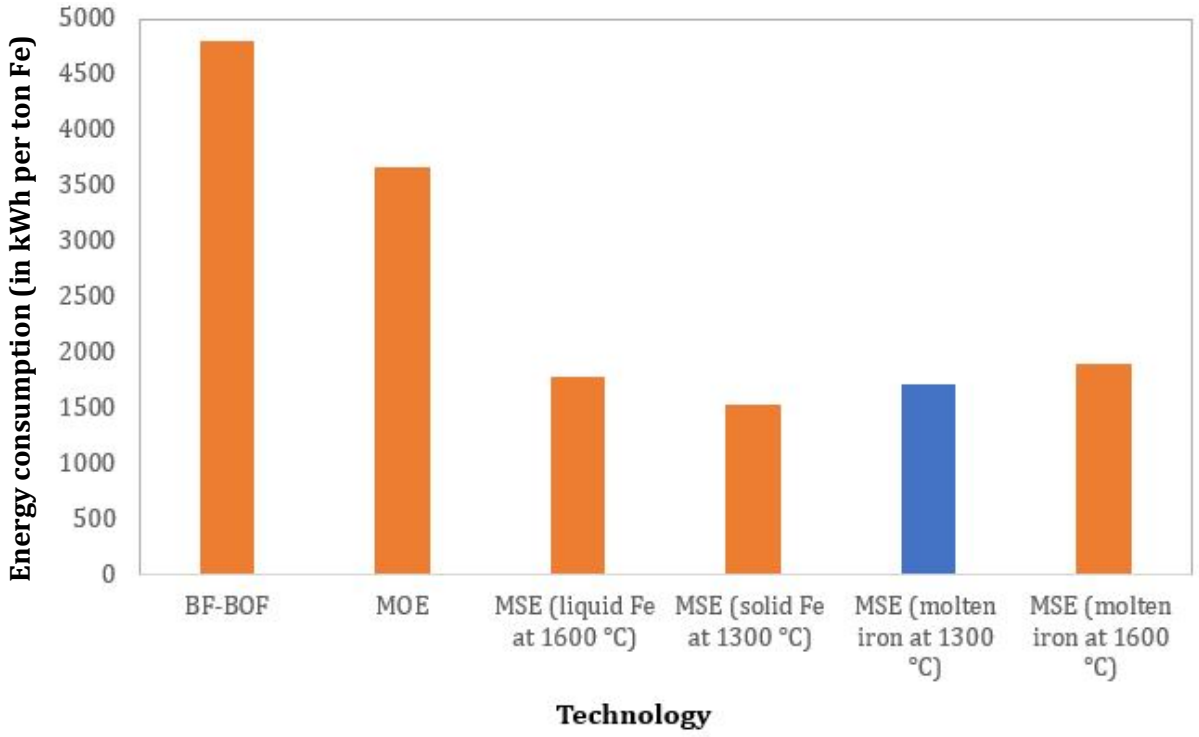

Figure 3.5 Bar chart depicting the energy requirements for steel making via BF-BOF, MOE and MSE processes

3.3 References

(1) Wang, D.; Gmitter, A.; Sadoway, D. Production of Oxygen Gas and Liquid Metal by Electrochemical Decomposition of Molten Iron Oxide. *Journal of The Electrochemical Society* **2011**, *158*. https://doi.org/10.1149/1.3560477.

(2) Allanore, A. Features and Challenges of Molten Oxide Electrolytes for Metal Extraction. *Journal of the Electrochemical Society* **2014**, *162*, E13–E22. https://doi.org/10.1149/2.0451501jes.

(3) Angarita Fonseca, M. P. Electrolytic Extraction of a Metal from Its Metal Compound: Estimates of Optimal Energy Requirements and Their Consequences., 2015. http://hdl.handle.net/1721.1/98004.

(4) Allanore, A.; Yin, L.; Sadoway, D. A New Anode Material for Oxygen Evolution in Molten Oxide Electrolysis. *Nature* **2013**, *497*, 353–356. https://doi.org/10.1038/nature12134.

(5) Daehn, K.; Stinn, C.; Rush, L.; Benderly-Kremen, E.; Wagner, M. E.; Boury, C.; Chmielowiec, B.; Gutierrez, C.; Allanore, A. Liquid Copper and Iron Production from Chalcopyrite, in the Absence of Oxygen. *Metals* **2022**, *12*, 1440. https://doi.org/10.3390/met12091440.

(6) Stinn, C.; Marden, L.; Benderly-Kremen, E.; Gilstrap, W.; Allanore, A. Bauxite Processing Via Sulfide Chemistry. In *Light Metals 2024*; Wagstaff, S., Ed.; Springer Nature Switzerland: Cham, 2024; pp 64–73. https://doi.org/10.1007/978-3-031-50308-5_8.

(7) Rush, L. Integrative Approach to Metal Extraction and Electrification, 2021. https://hdl.handle.net/1721.1/140135.

(8) Babich, A.; Senk, D. 17 - Recent Developments in Blast Furnace Iron-Making Technology. In *Iron Ore*; Lu, L., Ed.; Woodhead Publishing, 2015; pp 505–547. https://doi.org/10.1016/B978-1-78242-156-6.00017-4.

(9) *US20210277531A1 - Selective sulfidation and desulfidation - Google Patents*. https://patents.google.com/patent/US20210277531A1/en (accessed 2024-03-15).

(10) Stinn, C.; Allanore, A. Selective Sulfidation of Metal Compounds. *Nature* **2022**, *602*. https://doi.org/10.1038/s41586-021-04321-5.

(11) Allanore, A.; Stinn, C. R. Selective Sulfidation and Desulfidation. US20210277531A1, September 9, 2021. https://patents.google.com/patent/US20210277531A1/en (accessed 2024-02-23).

(12) Sokhanvaran, S.; Lee, S.-K.; Lambotte, G.; Allanore, A. Electrochemistry of Molten Sulfides: Copper Extraction from BaS-Cu 2 S. *Journal of The Electrochemical Society* **2015**, *163*, D115–D120. https://doi.org/10.1149/2.0821603jes.

(13) Daehn, K.; Benderly-Kremen, E.; Yagi, R.; Stinn, C.; Boury, C.; Rush, L.; Wagner, M. E.; Allanore, A. Scaling up Molten Sulfide Electrolysis for Liquid Copper Production from Chalcopyrite. *Proceedings of the Copper 2022 Conference, Santiago, Chile* **2022**.

(14) Daehn, K.; Allanore, A. Electrolytic Production of Copper from Chalcopyrite. *Current Opinion in Electrochemistry* **2020**, *22*, 110–119. https://doi.org/10.1016/j.coelec.2020.04.011.

(15) Allanore, A. Contribution of Electricity to Materials Processing: Historical and Current Perspectives. *JOM* **2013**, *65* (2), 130–135. https://doi.org/10.1007/s11837-012-0538-3.

(16) Goldbeck; O.K. Iron-Carbon. In *Iron- Binary Phase Diagrams*; 1982.

(17) Banya, S.; Matoba, S. Activity of Carbon and Oxygen in Liquid Iron. **1963**, *3* (1), 21–28.

Note: All enthalpy and Gibbs energy values are used from FactSage.

Chapter 4

Experimental Methods

The previous chapters laid down the theoretical and thermodynamic framework for iron production via molten sulfide electrolysis, starting from an oxide feedstock, primarily hematite, the most abundant oxide iron ore. Mass – energy balance for the two steps involved, namely sulfidation, i.e., preparation of the feedstock by treating the oxide ore with sulfur gas, and the electrolysis process was discussed, while detailing the enthalpy as well as electrical energy requirements of the process. Based on those calculations and comparisons of practical energy requirements with the conventional state-of-the-art BF - BOF technology and molten oxide electrolysis, it can be stated that MSE brings down the energy requirements for steel production significantly (52.8 % less than MOE and 64% less than BF-BOF) in addition to the massive reduction in carbon emissions (~87%). Thus, based on the theoretical and thermodynamic considerations, the process seems to be a promising candidate as an alternative method for producing steel by solely using electricity.

This chapter discusses the experimental methods to confirm the feasibility of the new process methodology proposed. It explains in detail the experimental preparation and setup for the various sets of experiments carried out using lab equipment. A series of solid-gas reactions were conducted to demonstrate the sulfidation of iron oxide to iron (II) sulfide and results of these experiments were interpreted to identify the working parameters (e.g., minimum temperature required, critical gas flow rate, bed height and porosity, etc.). The electrolysis experiments were conducted in a Thermal Imaging furnace and the experimental preparation, including fabrication of the electrodes, electrolyte synthesis is mentioned in detail here. This is then followed by the procedure for conducting MSE experiments while measuring the faradaic efficiency of the process by simple mass loss calculations. Additionally, the parameters affecting the faradaic efficiency are identified and some of them are studied as a part of this work, namely effect of current density and factors affecting the impedance of the system. A lot of experimental samples were generated in both the sulfidation and MSE experiments, and these required characterizing them to analyze and interpret the results. Thus, towards the end of the chapter, the various characterization tools used are discussed.

4.1 Feedstock preparation

4.1.1 Pre-treatment of the ore - Sulfidation

The process of preparing the feedstock for the MSE cells, by conducting a solid - gas reaction of an oxide material with sulfur gas, is termed as the sulfidation reaction[1–3]. This is because iron ore mined for steel production is in the form of oxides in the earth's crust. The most widely used oxide-based iron ore is hematite[4,5], which contains up to 65% Fe (~98% Fe_2O_3 - rich grade of iron ore). This mined oxide ore cannot be directly fed into the MSE cells,

as oxides are not soluble in sulfides. In order to be processed in the MSE cells, the oxide needs to be converted to sulfide. The reaction governing the pretreatment of the ore is as follows:

$$4\,Fe_2O_3\,(s) + 7\,S_2(g) \rightarrow 8\,FeS\,(s) + 6\,SO_2(g) \qquad (4.1)$$

To demonstrate the process of preparing the feedstock for the MSE cells, sulfidation reactions were carried out using pure lab grade Fe_2O_3 (99.85+ % metal basis, Alfa Aesar). The pure iron (III) oxide was heated in a sulfur-rich atmosphere[2,3], in a Split Mellen vertical tube furnace (Mellen, PS400-120-20CLT-C2778-R-OT). This methodology can be found in detail in the work by other authors[1–3], with relevant details for sulfidation of iron (III) oxide discussed in this section.

5 grams of pure lab grade Fe_2O_3 (99.85+ % metal basis, Alfa Aesar) were crushed using an agate mortar and pestle. It was subsequently sieved using sieving meshes to obtain a particle size between 90 microns and 106 microns. This particle size distribution was chosen to emulate the size distribution of the feed used in the blast - furnace. This crushed iron (III) oxide powder was filled in an in-house machined alumina crucible (50 mm OD, 41 mm ID, 34 mm depth, machinable alumina) up to a bed height of 5 mm. The custom-made alumina crucible, shown in **Figure 4.1**, had approximately 100 evenly spaced holes drilled at the bottom (1.5 mm OD) as well as at the sides (6.3 mm OD) for the sulfur gas to react across the entire bed height. To prevent the loss of Fe_2O_3 from the bottom during loading the sample, a kimwipe is placed at the bottom of the crucible.

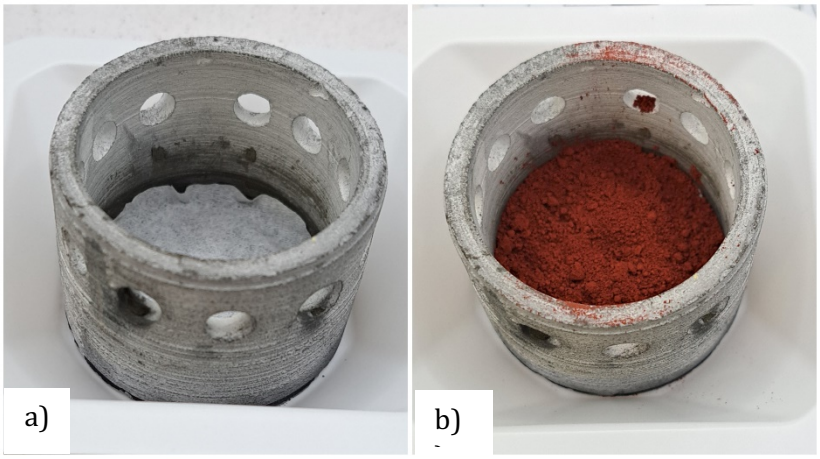

Figure 4.1 Alumina crucible with a (a) kimwipe (b) Fe_2O_3 powder used for sulfidation

The machined alumina crucible was soaked in with deionized water and dried at 200° C in a vacuum oven overnight before use. An alumina crucible was chosen compared to a graphite crucible to avoid any interaction of the oxide with carbon, to prevent carbothermic reduction of the oxide at the high temperature of operation. Additionally, the graphite crucible was not preferred to avoid any carbo-thermically driven sulfur reflux (CDSR) reactions[2,6], to give an accurate measure of the partial pressure of S_2 to SO_2 in the reactor.

Using an alumina support tube (29 cm length, 5.08cm OD, 4.445 cm ID), the iron (III) oxide containing crucible was positioned in the hot zone of a vertical tube furnace in an alumina tube (600 mm length, 25mm OD, 21mm ID, Advalue). Approximately 100 grams of elemental sulfur powder (99.5%, sublimed, Acros Organics) were carefully melted using a heat gun in a quartz crucible (28 mm OD, 101.6 mm depth). This crucible (shown in **Figure 4.2**) containing solidified and dense sulfur was loaded through the bottom of the furnace. Throughout the sulfidation, argon (Airgas, ultra-high purity) was flowed at a constant rate of 1500 sccm through the chamber, behaving as a carrier gas for S_2 and SO_2 (g). The **critical gas flow rate** was calculated by performing mass - balance calculations as described in the methodology in Stinn and Allanore (2021)[3].

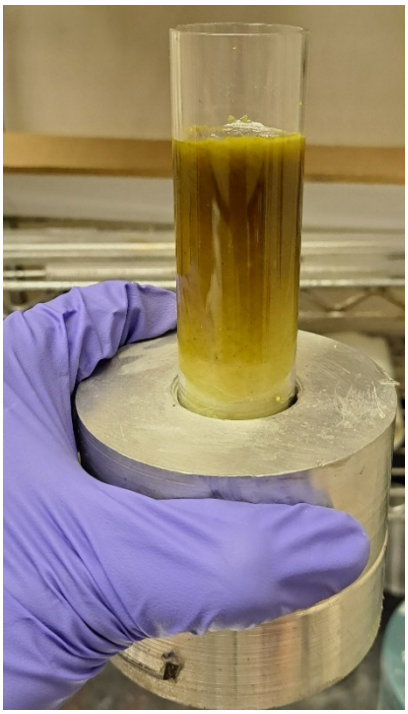

Figure 4.2 Sulfur crucible used for sulfidation

At the set temperature (reaction temperature), to ensure the sulfur partial pressure in the chamber is maintained at absolute pressure of 0.1 atm, the sulfur containing crucible was raised at 0.5 cm per minute using a stainless-steel tube (6.25 mm OD), also used for the Ar inlet, introduced at the bottom of the furnace port. As the reaction progressed, generating more SO_2 (g), the sulfur containing crucible was raised gradually and periodically over a certain calculated length, increasing the partial pressure of S_2 provided to the system.

The thermal profile for the sulfidation was as follows: The furnace was heated to a set temperature of 1000° C at a rate of 3° C /min, was held at this temperature (1000° C) for 45 mins and later cooled down to room temperature at a rate of 3° C /min. The ramp up rates were maintained at 3° C /min to avoid damage to the alumina tubes due to thermal shock. To capture the unreacted solidified sulfur particles in an in-house constructed gravity separator, a 1" diameter quartz tube was used for the outgas line. **Figure 4.3** and **4.4** depicts respectively the actual image and schematic of the vertical tube furnace used for the sulfidation experiments.

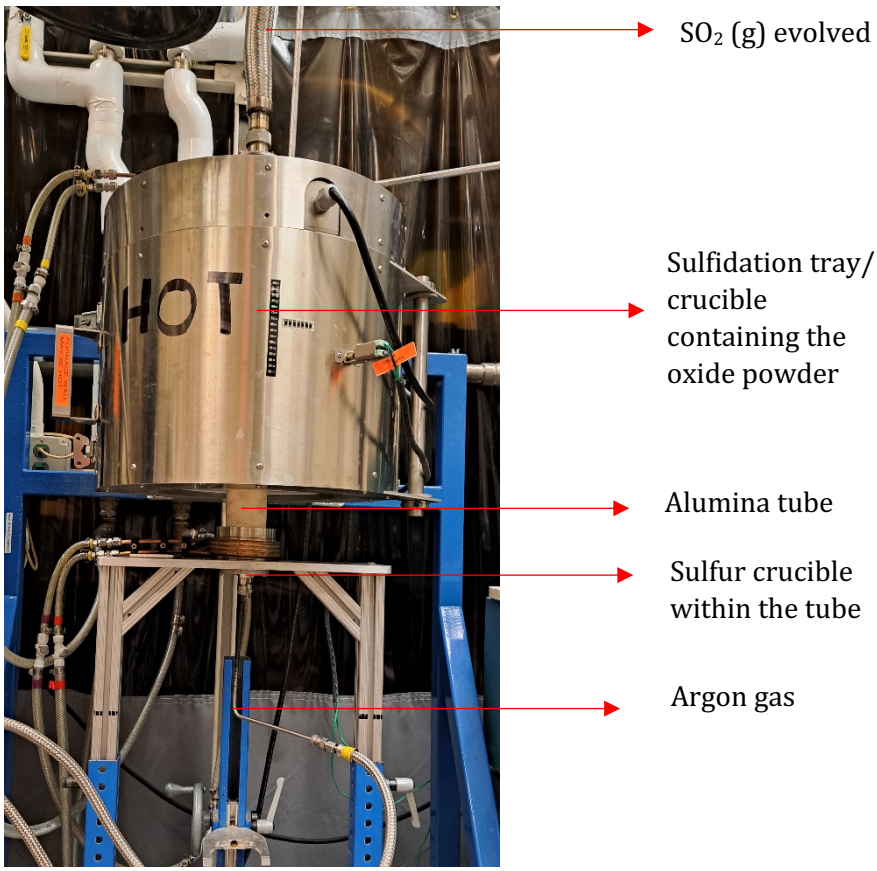

Figure 4.3 Vertical tube furnace used for the sulfidation experiments

1. Furnace
2. Alumina furnace tube
3. Stainless steel fitting
4. O-ring
5. O-ring compression ring
6. O-ring compression screw
7. Ar carrier gas inlet
8. Alumina support tube
9. Alumina support rod / O_2 inlet
10. Stainless steel crucible
11. Liquid sulfur
12. Packed bed reactor
13. Oxide to sulfidize
14. Gas outlet to gravity separator and IR sensor

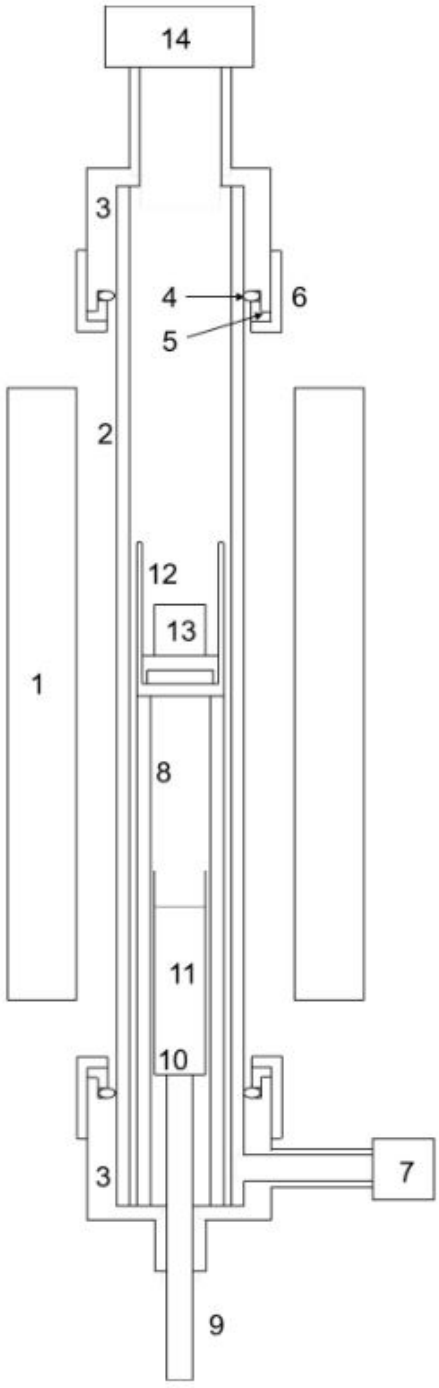

Figure 4.4 Schematic of the packed bed reactor used for sulfidation experiments (from C. Stinn)[7]

4.1.2 Post – sulfidation observations

Once the reactor cools down, the alumina crucible was carefully unloaded. **Figure 4.5** shows the product of the sulfidation reaction. Mass measurements were done to calculate the extent of the reaction (conversion rate) using the difference in mass measurements before and after the reaction, assuming there is no mass loss during loading and unloading. This was done by performing stoichiometric calculations for the expected mass of the product formed upon complete reaction with S_2 (g). After the mass measurement, the sample was immediately stored in a glove box to avoid the sulfidised product from getting oxidized by the environment. The powder bed (or pellet) was divided into approximately 4 equal parts and a cross-section across the bed was visually observed to check if the reactant was sulfidised completely up to the reactor bed core. In case it had not, further analysis at higher magnification was required to investigate the cause for incomplete reaction (see **section 5.1.2** for details)

Figure 4.5 Product of the sulfidation reaction

One part of the sample was mounted on epoxy and polished to be observed under the optical microscope for any distinct features using the cross-polarization mode. In case of incomplete reaction, the reaction front could be observed and studied at higher magnification to determine the cause. The same polished sample was observed under the SEM to visualize the features of the sulfide grains and carry out EDS analysis to account for

the elemental distribution in the sample. Another part of the initial sample was used for XRD analysis to confirm the chemistry of the product.

4.2 Electrochemical experiments – Molten Sulfide Electrolysis

Once the production of the feedstock to be fed into the MSE cells was successfully demonstrated via a sulfidation reaction, electrolysis experiments were performed at a scale of 300 mA (0.2 g electrolyte and a cathodic surface area of 0.176 cm^2), to investigate the electrochemical deposition of iron, as described below.

These experiments were performed in a Thermal Imaging furnace (TIF, TX-12000-I-MIT-VPO-PC, Crystal Systems Corp.). This is a 12kW lamps-based furnace, powered by four 3 kW Xenon lamps. Upon illumination, these with the help of ellipsoidal mirrors create a hot zone of one cubic centimeter volume at the focus. The hot zone can attain temperatures up to 3000° C, in comparison to typical furnaces which are limited to 1500° C. An external quartz tube, inside which the testing sample is placed, is used to maintain different types of atmospheres. This allows melting samples without the use of a container, by suspending an ingot type sample using a probe from the top fitting. Electrodes or thermocouples can be introduced inside the quartz tube from either shaft. Modifications made to the TIF for making electrochemical measurements are described by Nakanishi and Allanore[8]. The TIF has cameras installed on the front and side panels, which allow in-situ visual observations such as bubbling due to gas formation during electrochemical reactions.

To prepare the electrolyte for the 300 mA experiments (described in **section 4.2.1**), pure lab grade chemicals were used with 10 wt.% of iron (II) sulfide dissolved in a supporting electrolyte. The composition of the electrolyte was as follows: 55.8 wt.% BaS, 34.2 wt.% La_2S_3 and 10 wt.% FeS. Since the faradaic efficiency calculations were to be made using mass loss measurements, it was important to decouple the effect of thermal

decomposition/ thermal loss (if any) from the effect of the electrochemical reaction, on the observed mass loss. Hence, thermal decomposition trials were carried out in the TIF to observe the mass loss due to thermal decomposition (see **section 4.2.4**). The details about the equipment and procedure for galvanostatic electrolysis using a graphite anode and cathode (electrode fabrication described in **section 4.2.2**) are described in **section 4.2.5**.

Post-experiment observation and characterization techniques used to analyze the samples are described in **section 4.3**. The samples were analyzed using optical microscopy and SEM-EDS to understand the microstructure of the electrolytic deposition and obtain the elemental composition of the electrolyte at various locations, respectively. Further analysis, such as ICP-MS [I] and WDS [II] (*details mentioned in references section*) were conducted to give more accurate information about the light element composition in the electrolyte sample, specifically to investigate sulfur depletion after electrolysis.

The procedure to prepare the iron (II) sulfide feedstock iron (III) oxide for the MSE cells is described in **section 4.1.1**. However, for the 300 mA electrochemical experiments carried out, pure lab grade iron (II) sulfide was used.

4.2.1 Electrolyte synthesis

Previously, electrolytic deposition of Cu and Fe was demonstrated[9,10] by using a supporting electrolyte of composition 55.8 wt.% BaS (99.7% metals basis, Alfa Aesar), 34.2 wt.% La_2S_3 (99.0% metals basis, Alfa Aesar), (binary system characterized by Boury and Allanore)[11] with 10 wt.% sulfidized chalcopyrite, $CuFeS_2$. This was based on work by Stinn et al., who demonstrated the high solubility of copper sulfide in barium sulfide[12]. Sokhanvaran et al.[13] demonstrated that the supporting electrolyte supported ionic transport. The high decomposition potential of BaS and La_2S_3 as compared to FeS, allows the selective decomposition of FeS into Fe depositing at the cathode and S_2 gas evolved at the anode, upon electrolysis.

To alleviate the electronic conductivity in the supporting electrolyte for the MSE of FeS, lab grade iron (II) sulfide (99.9 % metal basis, Alfa Aesar) was dissolved at 10 wt.%, while keeping the remaining composition unchanged at 55.8 wt.% BaS, 34.2 wt.% La_2S_3. However, this proportion could be improved once a relationship of the electrolyte conductivity with composition and temperature and the mechanisms governing electrochemical decomposition are established. The constituent sulfides were ground using a mortar and pestle, see **Figure 4.6**, in a controlled atmosphere inside the glove box. 200 mg portions of the electrolyte powder mixture were loaded into 7 mm OD holes machined in graphite circular puck (53 mm OD, graphitestore). These droplets were pre – melted in the Mellen furnace (Mellen, PS400-120-20CLT-C2778-R-OT), at a set temperature of 1350 ◦ C to form a consolidated solid of the powder mixture for ease of handling. The thermal profile of the pre-melting procedure was as follows: the furnace was heated up to 1350◦ C (set temperature) at a rate of 5◦ C /min, held at 1350◦ C for 60 mins and then cooled down to room temperature at a rate of 5◦ C /min. Argon (Airgas, ultra-high purity) was flowed through the chamber at a rate of 450 sccm to maintain a controlled atmosphere within the reactor during the pre-melting. In case of presence of any residual oxygen in the graphite pucker, there are chances of carbothermic reduction occurring during the electrolyte synthesis. To rule out this possibility, characterization studies (optical microscopy and scanning electron microscopy) were carried out to observe if any metallic phase existed in the pre-melt. **Section 5.2.1** shows the SEM image and EDS scan results of the electrolyte after pre – melting. To confirm the elemental composition, the electrolyte was sent for ICP – MS [I] and LECO [III], results of which are provided in **Table 5.3**, in **section 5.2.1**

Figure 4.6 Electrolyte synthesis process in glove box (a) BaS and La_2S_3 powders (b) mixing of these powders with FeS (c) Graphite pucker used to fill the 200 mg electrolyte mix in each drilled hole

4.2.2 Fabrication of the electrodes

Graphite has been found to be stable and inert[9] during electrolysis of molten sulfides at temperatures greater than 1200◦ C . Hence, the electrodes, i.e., cathode and anode were machined using EDM quality graphite rods (fine extruded, 6.3mm OD, 305mm length, graphitestore). The height of the cathode stands (shown **Figure 4.7**) was 12 mm with a hemispherical depression/divet at the top to hold the electrolyte droplet. The cathodic surface area of approximately 0.19 cm^2 (6 mm ID, 0.7 mm depth) was machined using a dremel. The anode, as depicted in **Figure 4.7**, was machined to be tapered at one end into a fine tip using a belt sander. The height of the anode in total was 16 mm, with the tip (1.3 mm OD) being 11 mm long. On the opposite end of the electrodes, holes 3.06 mm ID) were drilled using a drill press and threaded, to be securely held by a molybdenum rod (>99.97%, 3.2mm OD, 600mm length, Ed Fagan) sheathed in an alumina tube when placed in the TIF. Before use, the graphite electrodes were sonicated for 15 mins using ethanol and were air dried.

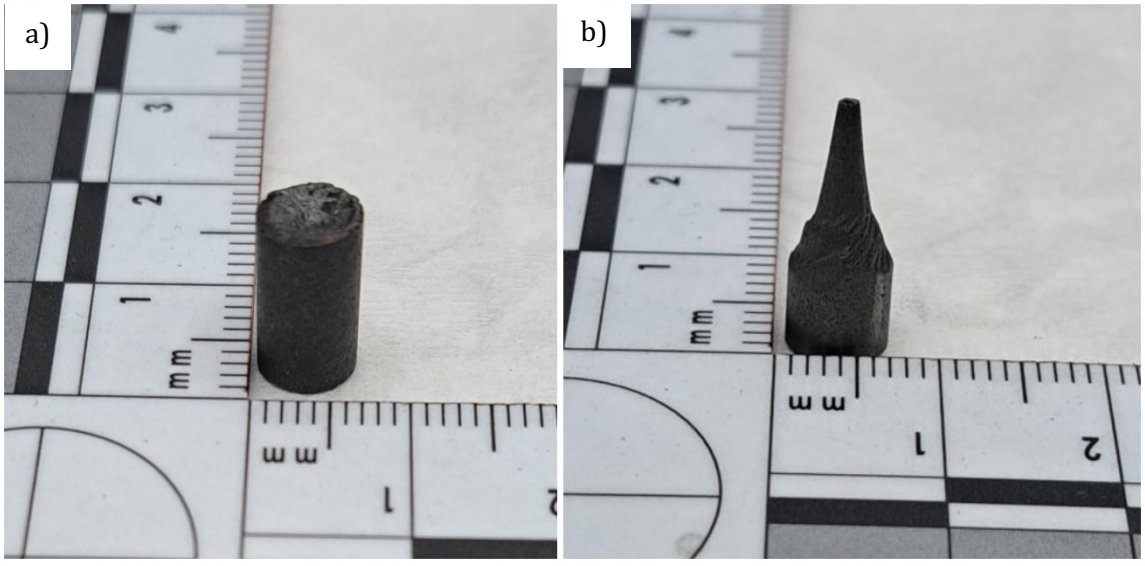

Figure 4.7 Graphite electrodes used for the MSE experiments (a) Cathode (b) Anode

4.2.3 Temperature measurement inside the Thermal Imaging furnace

To ascertain the working temperature inside the TIF, a Type-C thermocouple (made from W-Re alloys, used to measure temperature up to 2315° C) was used. The heat radiated by the Xe lamps in the TIF can only be controlled using the power of the lamps, hence it is important to measure the temperature inside the TIF for a given value of lamp power. At about 4 % power, the temperature as measured by the type-C thermocouple was 1300° C (± 50° C). The temperature inside the TIF is observed to be extremely sensitive to the position of the sample with respect to the hot zone created by the lamps.

4.2.4 Thermal decomposition trials

A systematic study to determine the mass loss due to thermal decomposition was carried out by conducting several thermal decomposition trials in the TIF for varying time durations in the absence of electrolysis. This was performed to decouple the mass loss due to thermal decomposition, if any, from the mass loss due to electrolysis, for similar experimental duration. The electrolyte was heated at 4 % power for 5, 10, 20, 30, 40 and 60 mins to determine a trend in the mass loss with time, if any. The individual masses of the anode, cathode and the electrolyte were carefully measured to milligram precision before and after the experiment. The experiments in the thermal imaging furnace were carried out in a controlled atmosphere with Argon (Airgas, ultra-high purity) flowing at 196 sccm for the entire duration. To avoid any minor oxygen contamination, the gettering furnace was used during the experiments after the set up was kept under vacuum (pressure: 10^{-3} atm) overnight. As a further check, to determine if any metal had formed due to thermal decomposition, a cross-section of the electrolyte subjected to the thermal-decomposition trial was characterized under the optical and scanning electron microscope.

4.2.5 Electrolytic reduction on a graphite cathode

The electrolytic experiments were carried out in same TIF (as described before in **section 4.2**). The electrode probes, made up of molybdenum rods sheathed in an alumina tube (>99.8%, 6.35mm OD, 4mm ID, Coorstek) were introduced from the top and bottom ports (sealed using Ultratorr fittings, securely holding the anode and cathode respectively. **Figure 4.8** depicts a schematic of the 2-electrode experimental set up used in the TIF for MSE experiments. Before the entire assembly was sheltered in a controlled atmosphere inside a quartz tube (customized, Technical Glass Products, Inc.) sealed using Viton O-rings, the cathode, anode, and electrolyte were individually weighed to milligram precision. Any loss of mass from the cathode or anode would indicate presence of oxygen inside the reactor, as mass loss was attributed to carbon getting burnt away as carbon dioxide. The atmosphere inside the tube was maintained under argon as described in the thermal-decomposition trials section.

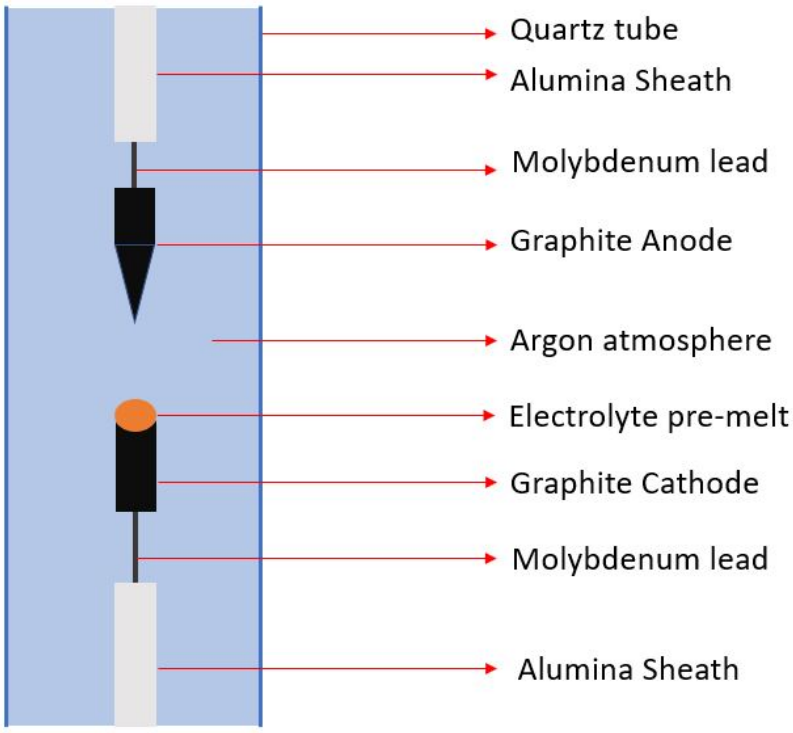

Figure 4.8 Schematic of the experimental set up in the Thermal Imaging furnace used for MSE experiments

To precisely position the electrodes in the hot zone of the furnace, up to 0.1 mm precision, monitored using a camera (EOS Rebel T5i DSLR, Canon Inc.), the probes were controlled by stepper motors. Once oxygen was scrubbed off from the system using the gettering furnace housing a Ti charge, and a constant flow of argon gas was ensured, the lamps were switched on and were powered to 4% power. The electrolyte was heated for about 2-3 mins till a stable molten droplet was formed, by rotating the bottom probe consisting of the cathode constantly at a rate of 10 rpm. To complete the circuit, the rotation was stopped, and the anode tip was moved down to contact the molten droplet, as shown in **Figure 4.9**. Galvanostatic electrolysis at a cathodic current density of 0.85 A/cm^2 and 1.7 A/cm^2 (anodic current density 10.64 A/cm^2) were carried out. A current of 0.15 A and 0.3 A was applied for varying time lengths of 20, 40 ,60, 90 and 120 seconds using the Gamry Reference 3000 potentiostat, to account for the faradaic efficiency. Results of the above experiments are shown in **Table 5.5** in the results section, see **section 5.2.3.2**. The current values were chosen such that the applied current density was similar to the aluminum industry standards (around 1 A/cm^2), and double of that to test if the system was stable at higher current density conditions. Additionally, galvanostatic measurements were also carried out to identify the current range where the decomposition potential was achieved.

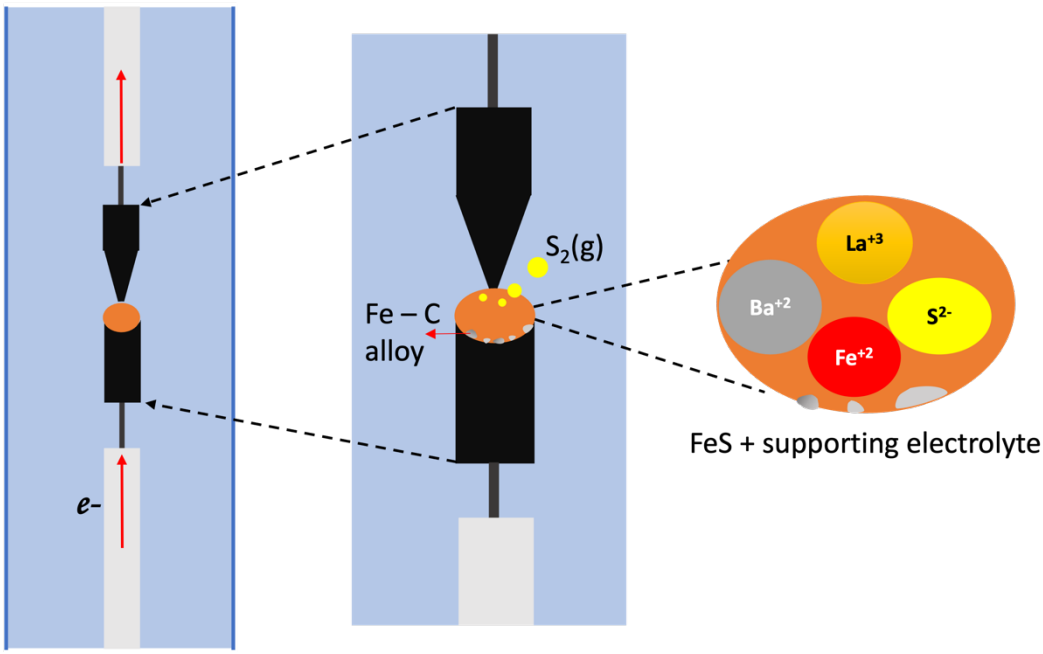

Figure 4.9 In-situ demonstration of the MSE experiment

Once the experiment was done (usual duration 5-6 mins), the lamps were switched off to quench the sample at a rate greater than 100° C /sec.

Apart from the electrolysis experiments, a systematic study of the factors affecting the impedance of the system was conducted. The following factors were studied: variation of the impedance with distance between the electrodes and the potential applied. For all the above studies, the counter electrode was used as a reference electrode (2-electrode set up) to record the cell voltages. Results of these are presented in **section 5.2.3.1.**

Shown below in **Figure 4.10** is an image depicting the partial setup of the cathode holding the electrolyte.

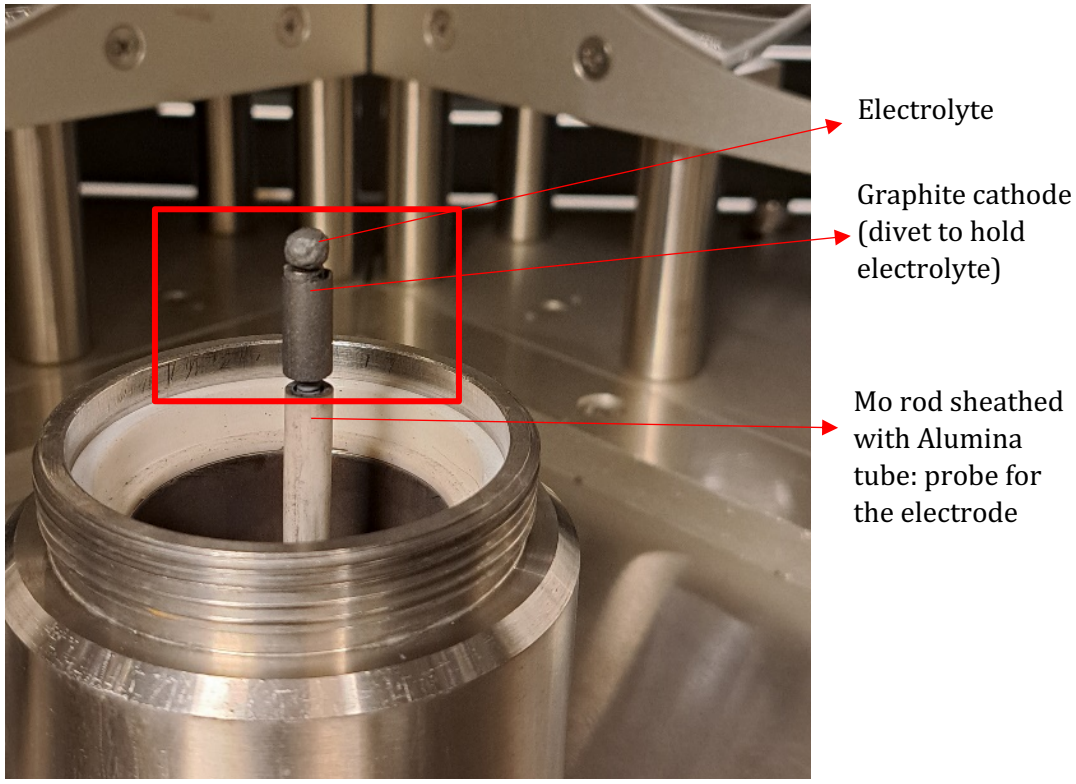

Figure 4.10 Partial setup of the graphite cathode (fixed to a Molybdenum rod sheathed with an alumina tube) holding the electrolyte.

4.3 post-experiment observations and characterization

The sample was carefully taken out from the furnace, 30 mins after the lamps were switched off. To prevent the sample from getting contaminated in the ambient atmosphere, mass calculations of the cathode, anode, and electrolyte were done immediately before the sample was mounted in epoxy resin for polishing for further characterization studies. It was then stored in the glove box in an inert atmosphere.

4.3.1 Mass loss calculations

Each of the assembly parts were weighed to milligram precision to observe the mass change in the anode, cathode, and electrolyte. While the mass loss of the electrodes was insignificant, the values of change in mass of the electrolyte are a direct correlation to the amount of sulfur released during the electrolysis experiments. As described earlier, since BaS and La_2S_3 have remarkably high decomposition potentials, the only constituent undergoing decomposition is FeS. Also, at the operating temperature, none of the components volatilize from the electrolyte[11] to incur a mass loss. From these values, the anodic faradaic efficiency of the electrolysis experiment can be calculated using the following formula:

$$\eta = \frac{(mass\ loss\ of\ the\ electrolyte)\times Z\times F}{Current(A)\times time(in\ secs)\times Mass\ S_2} \times 100 \qquad (4.2)$$

Mass loss of the electrolyte is in grams, Z is the number of electrons exchanged, F is the Faraday's constant: 96485 C/e^-, current is in A, time in seconds and $Mass\ S_2$ is the molar mass of sulfur gas S_2.

The results of the mass loss of the electrolyte for each of the electrolysis experiments carried out along with the calculated faradaic (anodic) efficiency are shown in the results section, see **Table 5.5** and **Figure 5.16** in **section 5.2.3.2.**

4.3.2 Optical microscopy

For microscopic observations, the electrolyte sample was mounted in epoxy and then polished down to 1 micron to observe its cross-section under the microscope. Leica LMDM reflected light scope with a Zeiss Axiocam 306 camera and Zeiss Zen imaging software was used for the microscopy. During polishing, the mounted sample was first ground using grit size 180 and 240 to reach half through the electrolyte. It was then polished using polishing pads (silicon carbide as the grinding media) of grit size 400, 600, 1000 and 1200 with mineral oil as the solvent, followed by a diamond polish of 6 micron and 1 micron to get a mirror-like finish.

The sample was observed under the optical microscope to see if any metal deposition had occurred. To observe the microstructure of the Fe deposited and carbide inclusions (if any), the electrolyte sample was etched in 3% *Nital* (Nitric acid - HNO_3 mixed with ethanol in a volume ratio of 3:100) for about 3 secs. This was done to reveal certain structural characteristics of the Fe deposit and get a qualitative estimate of the carbon content by comparing it with the microstructure of cast iron, high and low carbon steels.

Optical micrographs depicting metallic deposition are shown in **section 5.2.3.3, Figure 5.17.**

4.3.3 Scanning electron microscopy

To confirm the elemental composition of the metallic deposition and observe depletion of iron from the electrolyte, the electrolyte sample was analyzed under the scanning electron microscope and subjected to EDS. The JEOL JSM – 6610 LV SEM, a facility at MIT MRL (Materials Research Laboratory) was utilized for this purpose. The results of the EDS analysis scans are shown in **section 5.2.3.3**. To study depletion of iron in the electrolyte, compositional analysis was done at several points at various locations in the electrolyte, such

as the part in contact with the cathode (electrolyte bottom), center of the electrolyte and top part. The residual Ba/ La ratio was calculated at these points to draw conclusions about the minimum amount of Fe which must be always present in the electrolyte to ensure deposition. This conclusion would provide insight into the feeding rate of FeS in the electrolyte in a semi-continuous process. Line scans were done at specific locations of the electrolyte to observe Fe depletion. Element intensity maps were also generated to get a visual representation of the distribution of the elements within the electrolyte along with their qualitative relative concentrations at various locations (see **Section 5.2.3.3, Figure 5.21)**

4.3.4 XRD

X-Ray diffraction analysis was done on powder samples generated from sulfidation experiments. The Rigaku PANalytical X'Pert Pro X-Ray Powder diffraction instrument with a Cu source, available at MIT MRL was used for the powder diffraction experiments. The data generated over a 40 min scan was quantified and analyzed using the Highscore Plus software to fit the profile. This gave us precise information about the phases present in the powder by using the data about their peak position and intensity.

4.3.5 ICP-MS

To get a qualitative measure of the total elemental composition in the electrolyte, the electrolyte sample (200 mg) was sent to Lehigh Testing Laboratories for ICP – MS analysis [1]. The test measured the following elements with 0.01 wt.% precision: Ba, La, Fe and S. To compare the difference in the composition (especially that of sulfur) between samples subjected to various experimental conditions: ICP -MS was done on the pre-melt and on a sample, which was subjected to electrolysis, to compare and confirm the mass loss being due to sulfur.

4.3.6 LECO

Since an EDS analysis does not provide an accurate measure of the light elements in the electrolyte, to quantitatively measure the amount of carbon and oxygen (expected to be present as trace elements with not more than 1 wt.%), a LECO (Light element carbon and oxygen) test was done. The sample was combusted to measure the amount of carbon and oxygen by analyzing the composition of the gases evolved. The pre-melt was sent for analysis to account for any carbon (from the graphite pucker) or oxygen contamination before electrolysis is performed. Results of the same are presented in **section 5.2.3.3**. The LECO test was performed by Applied Technical Services (ATS Lab) in Georgia [III].

4.3.7 WDS

WDS measurements have higher spectral resolution than EDS as only one element is measured at a time, unlike X-Ray lines from all elements being measured simultaneously[14]. This is advantageous especially when the concentration of the constituent elements is low. Thus, one electrolyte sample was sent for WDS analysis to get the exact composition of the distinct phases identified around the Fe deposit and observe any Fe depletion in the electrolyte. Most importantly, it was performed to analyze the sulfur content within the Fe deposit, since sulfur is expected to be a trace element in the Fe produced as a result of MSE. Higher concentrations of sulfur greater than 0.05% are not desirable since it leads to hot shortness[15,16] in steel. Carbon content within the Fe deposit was however not measured due to the sample being coated with carbon particles to deem it conductive for WDS analysis [II].

4.4 Summary

This chapter discussed the experimental techniques used to verify and confirm the theoretical conclusions of the process methodology hypothesized as an emission-free alternative to producing molten iron electrolytically. It begins with a discussion of the experimental set-up and method for the initial pre-treatment of the iron oxide, which comes under the flag of feedstock preparation. This includes a detailed experimental procedure of the sulfidation experiment, followed by the post-experimental observations.

Subsequently, the chapter delves into discussing the reduction technique used for converting sulfide to metal, namely MSE. This includes the following:

1. A comprehensive experimental approach of the MSE experiments conducted to confirm feasibility of MSE for iron production by calculating the faradaic efficiency
    a. This section is subdivided into multiple sub-sections dealing with information related to electrolyte synthesis, electrode fabrication and the actual MSE experiments.
2. Identifying and studying the effect of the following factors: Current density and charge passed
3. Identifying and investigating the factors affecting the impedance of the system

Finally, the chapter discusses the various characterization tools and techniques used to analyze and interpret the experimental observations to draw important conclusions, which are deliberated in the following chapters.

4.5 References

(1) Allanore, A.; Stinn, C. R. Selective Sulfidation and Desulfidation. US20210277531A1, September 9, 2021. https://patents.google.com/patent/US20210277531A1/en (accessed 2024-02-23).

(2) Stinn, C. Pyrometallurgical Oxide-Sulfide Anion Exchange for Improved Material Separation and Metal Production, 2023. https://hdl.handle.net/1721.1/151594.

(3) *US20210277531A1 - Selective sulfidation and desulfidation - Google Patents*. https://patents.google.com/patent/US20210277531A1/en (accessed 2024-03-15).

(4) World Steel Association. Fact Sheet | Raw Materials in the Steel Industry, 2023. https://worldsteel.org/wp-content/uploads/Fact-sheet-raw-materials-2023.pdf.

(5) *Iron Ore - an overview | ScienceDirect Topics*. https://www.sciencedirect.com/topics/materials-science/iron-ore (accessed 2024-03-15).

(6) Stinn, C.; Allanore, A. Selective Sulfidation of Metal Compounds. *Nature* **2022**, *602*. https://doi.org/10.1038/s41586-021-04321-5.

(7) *Selective sulfidation of metal compounds | Nature*. https://www.nature.com/articles/s41586-021-04321-5 (accessed 2024-03-15).

(8) Nakanishi, B. R.; Allanore, A. Electrochemical Study of a Pendant Molten Alumina Droplet and Its Application for Thermodynamic Property Measurements of Al-Ir. *J. Electrochem. Soc.* **2017**, *164* (13), E460–E471. https://doi.org/10.1149/2.1091713jes.

(9) Daehn, K.; Stinn, C.; Rush, L.; Benderly-Kremen, E.; Wagner, M. E.; Boury, C.; Chmielowiec, B.; Gutierrez, C.; Allanore, A. Liquid Copper and Iron Production from Chalcopyrite, in the Absence of Oxygen. *Metals* **2022**, *12*, 1440. https://doi.org/10.3390/met12091440.

(10) Stinn, C.; Gutierrez, C.; Daehn, K.; Allanore, A. Sulfidation for Copper Mineral Processing and Impurity Management. *Copper 2022* **2022**.

(11) Boury, C.; Allanore, A. Liquid State Properties and Solidification Features of the Pseudo Binary BaS-La2S3. *Sci Rep* **2021**, *11* (1), 18189. https://doi.org/10.1038/s41598-021-93576-z.

(12) Stinn, C.; Nose, K.; Okabe, T.; Allanore, A. Experimentally Determined Phase Diagram for the Barium Sulfide-Copper(I) Sulfide System Above 873 K (600 °C). *Metallurgical and Materials Transactions B, Process Metallurgy and Materials Processing Science* **2017**, *48* (6). https://doi.org/10.1007/S11663-017-1107-5.

(13) Sokhanvaran, S.; Lee, S.-K.; Lambotte, G.; Allanore, A. Electrochemistry of Molten Sulfides: Copper Extraction from BaS-Cu 2 S. *Journal of The Electrochemical Society* **2015**, *163*, D115–D120. https://doi.org/10.1149/2.0821603jes.

(14) *Why is spectral resolution so important when analysing using WDS? - Nanoanalysis*. Oxford Instruments. https://nano.oxinst.com/library/past-blogs/spectral-resolution-wds (accessed 2024-03-15).

(15) Rudyuk, S. I.; Fel'dman, É. I.; Chernov, E. I.; Korobeinik, V. F. Effect of Sulfur and Phosphorus on the Properties of Steel 18B. *Met Sci Heat Treat* **1974**, *16* (12), 1056–1059. https://doi.org/10.1007/BF00664052.

(16) Myasoedov, S.; Filatov, S.; Пантелеев, В.; Listopadov, V.; Zagainov, S. Analysis of Possible Ways to Reduce Sulfur Content in Pig Iron. *Izvestiya. Ferrous Metallurgy* **2021**, *63*, 878–882. https://doi.org/10.17073/0368-0797-2020-11-12-878-882.

Details of the external services used for material analysis

I. ICP: Lehigh Testing Laboratories, 308 West Basin Road, New Castle, DE 19720
II. WDS: Electron Microprobe facility, Department of Earth, Atmospheric and Planetary sciences, Massachusetts Institute of Technology, Cambridge, MA 02139
III. LECO: Applied Technical Services (ATS Lab), 1049 Triad Court, Marietta, GA 30062

Chapter 5

Results and Discussion

The previous chapter described the experimental methods used to verify the feasibility of the sulfidation and the molten sulfide electrolysis process. This included an in-depth description of the experimental set up for both processes including the characterization tools used to analyze the samples. This chapter will discuss the important observations and results of the experiments carried out, while drawing conclusions about the thermodynamic and lab-scale feasibility of the novel sulfide pathway for molten iron production. This would include an elaborate discussion of results of the feedstock preparation through the sulfidation process, analysis of the characterization studies carried on the sulfidized product, analysis of the electrolyte synthesized and observations from the electrolysis experiments.

5.1 Sulfidation

An overall reaction for the sulfidation process can be written as follows:

$$4\ Fe_2O_3\ (s) + 7\ S_2(g) \rightarrow 8\ FeS\ (s) + 6\ SO_2(g) \tag{5.1}$$

From past sulfidation experimental evidence and preliminary experiments it was observed that the sulfidation process follows the shrinking core reaction mechanism[1], reacting from the outer surface to the inner core. This conclusion was arrived at, since some experiments revealed an unreacted core of the powder bed, due to kinetic and mass transport limitations when using a too large bed height. In other cases, the reacted iron sulfide particles sintered, preventing the sulfur gas from reaching the core, leaving it unreacted. At times, Fe_3O_4 was observed in the unreacted core. This could be attributed to the reaction having not approached completion, as Fe_3O_4 serves as the intermediate in the conversion from iron (III) oxide to sulfide. This may be due to a drop in the local partial pressure of SO_2 once the oxide at the bed surface gets converted to sulfide, thereby slowing down further sulfidation reaction of the additional oxide to sulfide. Another possibility could be due to transport limitations for sulfur penetration to the core. This is because, in the case where sulfur cannot react with the iron oxide, it reacts with FeS to form pyrite, which may eventually decompose and react with iron (III) oxide to form Fe_3O_4 in the following reaction:

$$FeS\ (s) + \frac{1}{2}S_2(g) \rightarrow FeS_2 \tag{5.2}$$

$$FeS_2(s) + 16\ Fe_2O_3(s) \rightarrow\ 11\ Fe_3O_4(s) + 2\ SO_2(g) \tag{5.3}$$

Hence, the sulfidation reaction parameters (temperature, gas flow rate, particle size distribution and reaction bed height) were validated through trial and error to ensure complete conversion of the oxide. See **Appendix 1** for reference.

5.1.1 Mass Change calculations

The stoichiometric calculation for the expected final mass of the above reaction is depicted below:

Calculation: $Moles\ of\ Fe_2O_3 = \frac{Given\ mass}{Molar\ mass} = \frac{7.51\ gm}{159.69\ gm/mol} = 0.047\ mol$

$$Moles\ of\ FeS\ (acc.to\ stoichiometry) = 2 \times 0.047 = 0.094\ mol$$

$$Expected\ mass\ of\ FeS = 0.094\ mol \times \frac{87.91 gm}{mol} = \mathbf{8.268\ gm}$$

The experimental initial and final masses were 7.51 grams and 8.25 grams, respectively, implying a conversion of 99.78%.

5.1.2. Optical and Scanning Electron microscopy

The optical microscopy images of the sulfidized product at magnifications of 10X, 20X, 50X are shown below in **Figure 5.1**. The sulfide particles are observed to be shiny and porous under the optical microscope as compared to the oxides (Fe_2O_3 or Fe_3O_4; see **Appendix 1** for reference), which are dull and dense. These micrographs are clear evidence of sintering to have occurred during the process, restricting further mass transport of S_2 gas inward or SO_2 outward. Since the bed height was limited in this case, it resulted in complete conversion of the oxide to sulfide or else a reaction front could be observed with some part of the core staying unreacted or partially reacted (see **Appendix 1** for reference). The reasons for incomplete conversion are expected to be among the following:

1. Most prominent cause of incomplete reaction is mass-transport limitation due to grain sintering[1], which restricts the S_2 (g) from transporting to the center of the reactor bed, thus preventing further reaction due to absence of the gas reactant.

2. Low porosity in the reactor bed, slowing down the diffusion of S_2 gas to the reaction front.
3. Not high enough temperature: slow kinetics of the chemical reaction between sulfur gas and the oxide phase
4. Larger grain size affecting the intra-grain diffusion of $S_2(g)$[1]
5. Ineffective gas flow rate: The gas flow rate should not be too high or low, as this disturbs the $P_{S_2(g)}/P_{So_2(g)}$ required for the reaction reactor to take place.

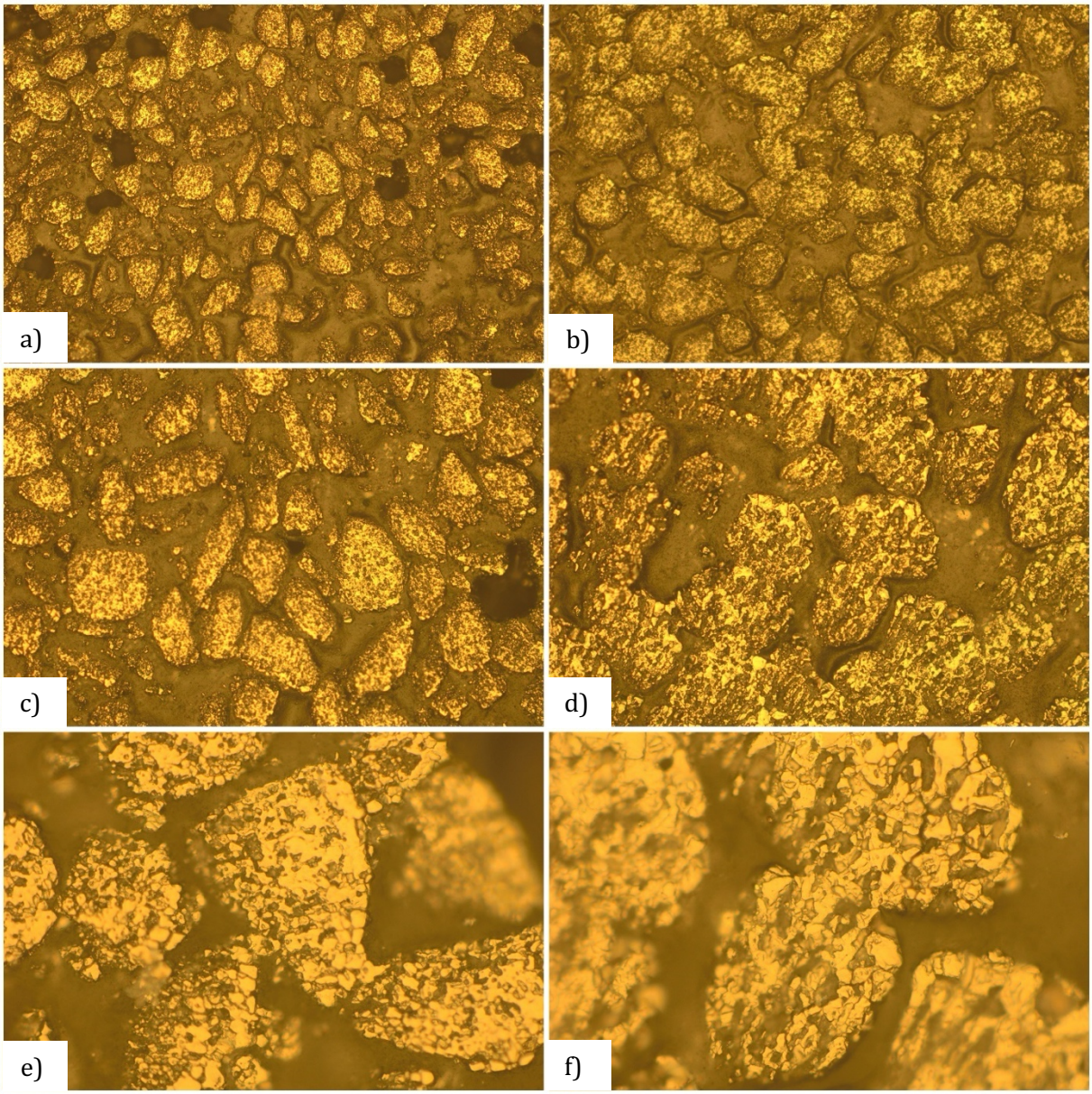

Figure 5.1 Optical micrographs of product of sulfidation of Fe_2O_3: (a, b): 10 X; (c, d): 20 X; (e, f): 50 X

The scanning electron micrographs of the sulfidized samples along with their EDS results are presented in **Figure 5.2** and **Table 5.1**. From the atomic concentrations of iron and sulfur, as obtained from the EDS results, the stoichiometry of the product compound formed upon sulfidation can be estimated. Iron sulfide is known to exist as various off-stoichiometric compounds, which could be either sulfur rich or sulfur deficient depending on the process conditions, in particular the $P_{S_2(g)}/P_{So_2(g)}$. The stoichiometry of the compounds is important to verify, as it may affect the efficiency of the molten sulfide electrolysis process. In this case, the stoichiometry of the product is estimated to be around $Fe_{0.9}S$.

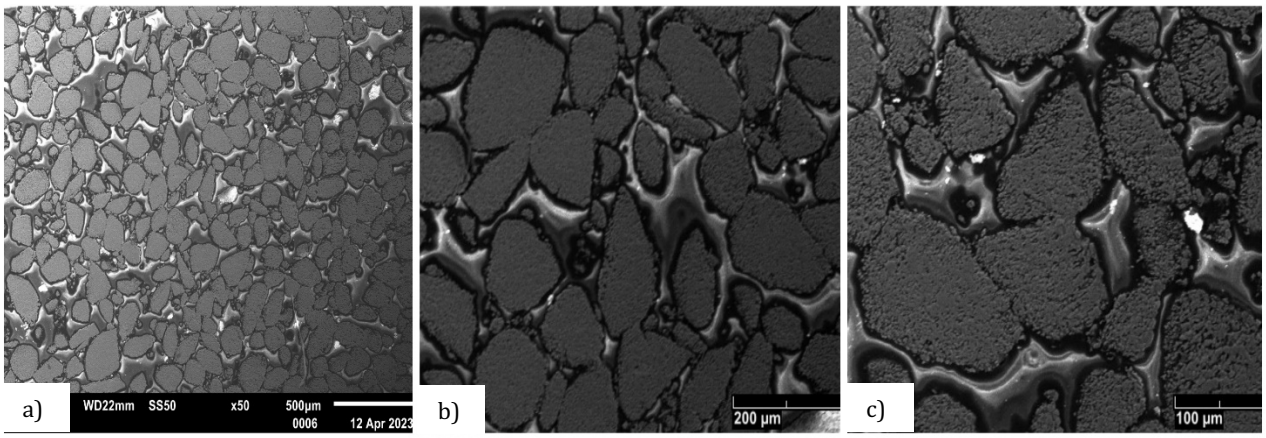

Figure 5.2: SEM micrographs of product of sulfidation of Fe_2O_3: (a): 50 X; (b): 100 X; (c): 200 X

Element	Concentration (wt.%)
Fe	57.99
S	37.54
O	4.47[viii]

Table 5.1: Approximate compositional analysis of the product after EDS analysis

The XRD or ICP are needed to provide a more accurate chemical signature of the compound formed upon sulfidation. In cases, where the reaction does not reach to

[viii] Shows up because of epoxy

completion, there is a phase separation observed between the oxide and sulfide phases depicting the immiscibility of the two phases (see **Appendix 1**), signifying ease of separation using simple and inexpensive physical separation techniques such as froth floatation.

5.1.3 XRD

As mentioned in the earlier section (see **section 4.3.4**), the product was analyzed for its phase composition using XRD. The peaks as seen in the XRD results corresponded to FeS (iron (II) sulfide) with insignificant traces of any residual oxides. The figure below (**Figure 5.3**) shows the peaks as observed on X-ray diffraction.

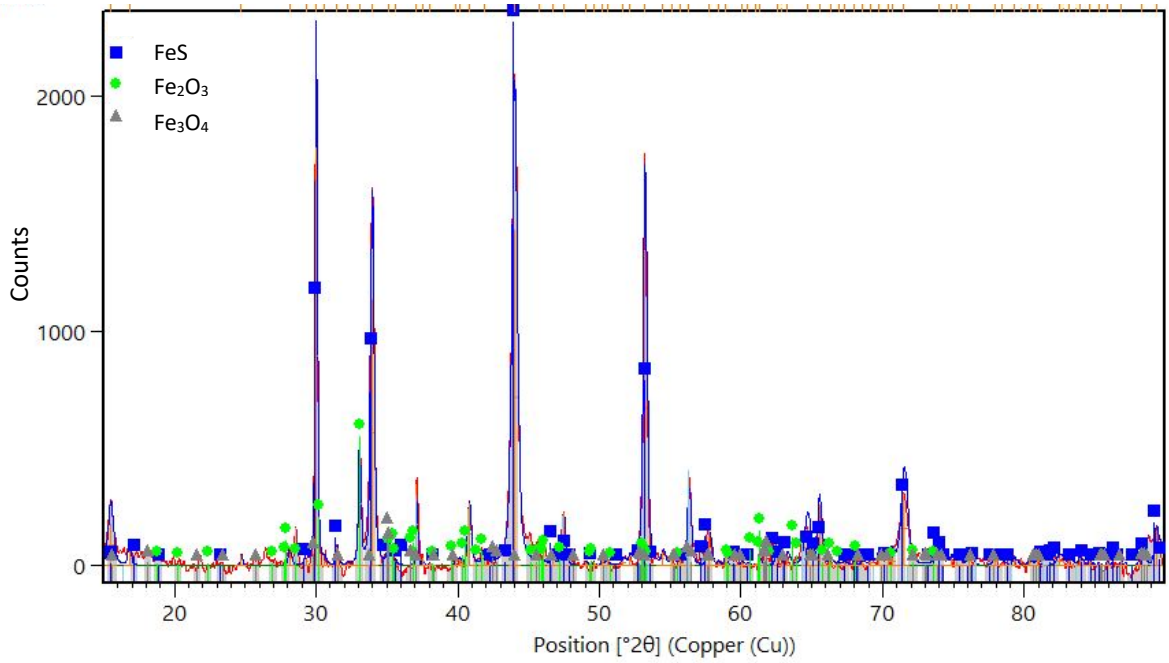

Figure 5.3: XRD scan of the product upon sulfidation of iron (III) oxide

5.2 Electrolytic reduction for iron production

5.2.1 Electrolyte synthesis

Based on experimental evidence and literature studies, the percentage of FeS to be dissolved in the supporting electrolyte is governed by the following factors:

1. Dependence of conductivity of the electrolyte[2] and the current density on the concentration of FeS in the supporting electrolyte: too high an electronic conductivity is not desirable but the process needs high ionic conductivity to ensure low ohmic drop
2. Variation of the melting point of the supporting electrolyte with the concentration of FeS in the electrolyte: the electrolyte needs to be molten state, and since the desired product is molten iron (melts at 1147◦ C, with 4.3 wt.% carbon), the melting point of the electrolyte should be in the range of 1200 ◦ C (+ 100 ◦ C as superheat to ensure flowability)
3. Ideally, if a high percentage of FeS shall be soluble, it is advantageous to operate with a high FeS content assuming the previous 2 conditions are satisfied: this allows for a larger amount of molten iron to be processed per electrolysis cell at any time.

The electrolyte used for the electrochemical experiments was pre-melted in the furnace as described in **section 4.2.1**, resulting in solid droplets of about 200 mg, around 180 mm^3. To account for any mass loss during the pre-melting process and/or oxygen contamination, weight measurements were carried before and after the pre-melt procedure. **Table 5.4** (see **section 5.2.2**) shows the mass loss recorded for each electrolyte droplet. A consistent mass loss of less than 1 mg[ix]. This insignificant mass loss indicates the absence of oxygen contamination that would have led to sulfates or oxysulfide. The pre-melt was analyzed using $LECO^{III}$ to confirm the carbon or oxygen content (if any) resulting from

[ix] could result from an error in measurement from the precision level of the scale

contamination from the graphite pucker or furnace atmosphere respectively, the results of which are shown in **Table 5.3**.

Shown below in **Figures 5.4, 5.5** and **5.6** are the optical and SEM micrographs of the electrolyte after pre-melting. No compound formation was observed in the pre-melt during SEM characterization. At least 2 phases can be observed – Ba rich phase (dark colored) and a La rich phase (light colored)[3]. The approximate composition of these phases (as recorded after EDS analysis) is shown in **Table 5.2**.

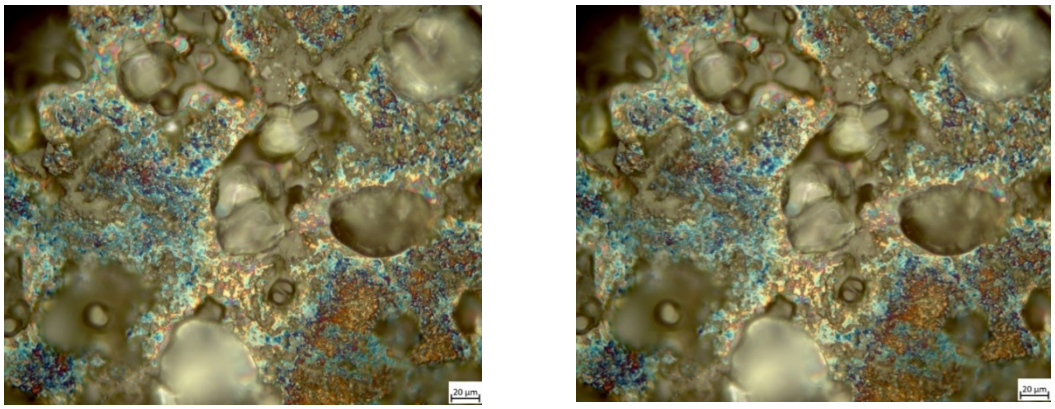

Figure 5.4: Optical micrographs of the cross-section of the electrolyte sample before electrolysis (pre-melt) depicting different colors for the 2 main phases Ba rich and La rich identified

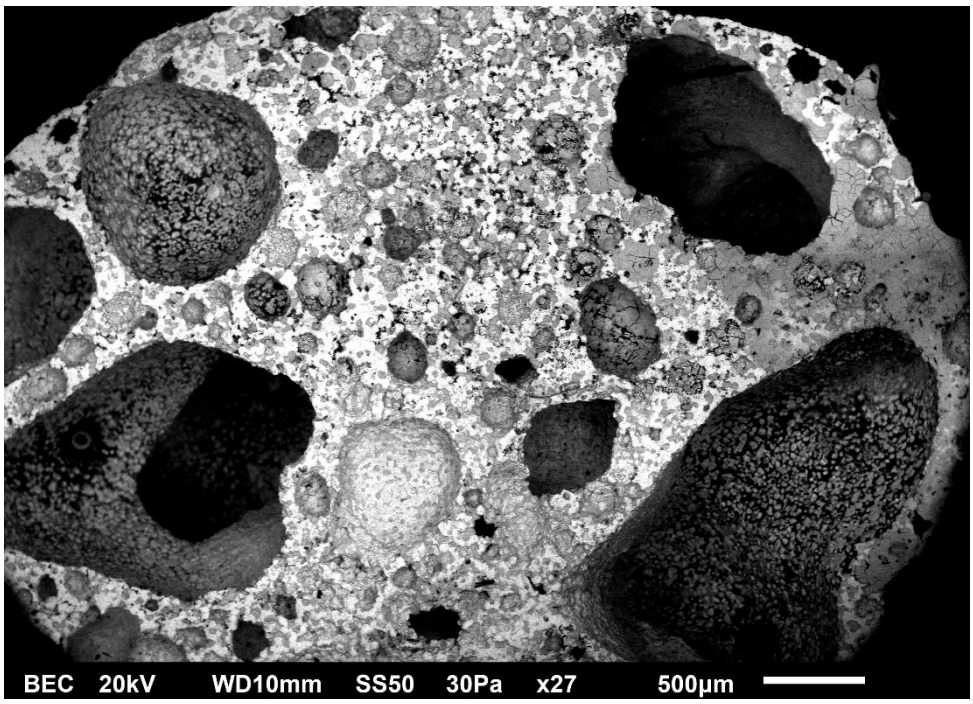

Figure 5.5: SEM micrographs of the cross-section of the electrolyte sample after pre-melt

Phase	Ba	La	Fe	S
Dark colored	54.61 wt.%	25.44 wt.%	4.21 wt.%	15.75 wt.%
Light colored	34.56 wt.%	39.18 wt.%	5.59 wt.%	20.67 wt.%

Table 5.2: Approximate phase composition of the observed phases in the electrolyte pre-melt

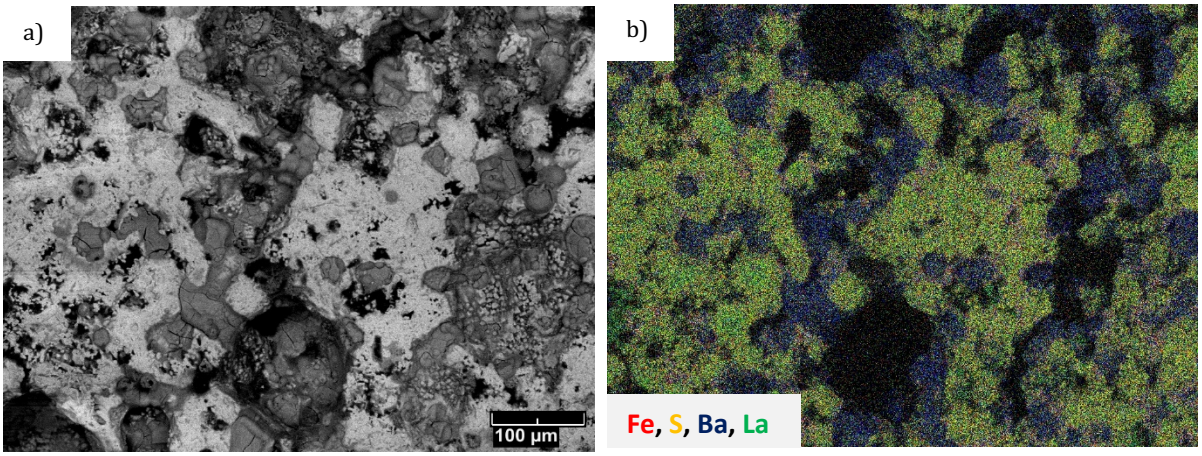

Figure 5.6: (a) SEM micrograph and (b) element intensity overlay of the part of the pre-melt cross-section depicting the 2 phases: Ba rich and La rich

To get an exact composition of Fe, S, C and O in the pre-melt, the electrolyte was sent for ICP-MS and LECO, results of which are shown below:

Fe (ICP)	S (ICP)[x]	C (LECO)	O (LECO)
6.64 wt.%	15.65 wt.%	0.03 wt.%	0.038 wt.%

Table 5.3: Results of the ICP-MS [I] and LECO analysis [III] of the electrolyte pre-melt

There is no significant oxygen or carbon contamination in the electrolyte sample, thus eliminating any possibility of oxysulfide formation or carbothermic reactions.

[x] Since the sulfur content was higher and not in ppm level, measuring it using ICP was more accurate

5.2.2 Thermal decomposition trials

The thermal-only trials were conducted on the electrolyte samples as described in section 4.2.4. to decouple the mass loss due to thermal effect (vapor pressure or spontaneous reactions) versus those from actual electrolysis. The results of the trials are shown below in **Table 5.4** and plotted with time in **Figure 5.7**:

Mass before pre-melt (g)	Pre-melt at 1350˚C (g)	Loss -1 (g)	Duration of droplet thermal treatment (mins)	Mass after thermal treatment (g)	Loss -2 (g)
0.2002	0.1997	0.0005	5	0.199	0.0007
0.1984	0.1974	0.001	10	0.1958	0.0016
0.1986	0.1981	0.0005	20	0.1971	0.001
0.1985	0.1979	0.0006	30	0.1968	0.0011
0.1998	0.199	0.0008	40	0.1986	0.0004
0.1984[xi]	0.1956	0.0028	50	0.1946	0.001
0.1995	0.1988	0.0007	60	0.1973	0.0015

Table 5.4: Results of the mass loss measurements in pre-melt synthesis and following thermal trials

[xi] some powder mixture spilled on the graphite pucker flat surface instead of the depressions designated to be filled, resulting in lower mass value filled inside the holes

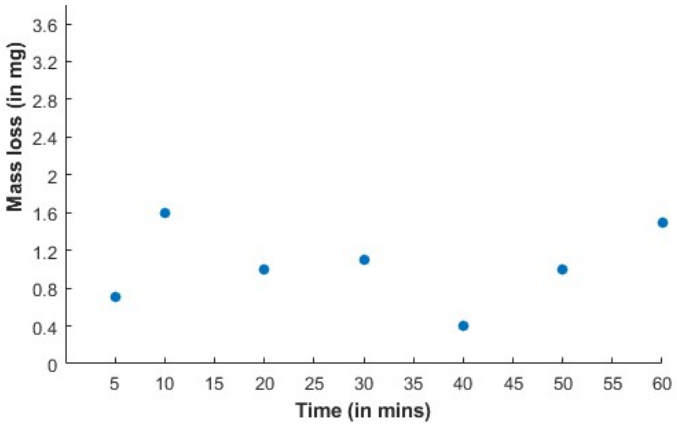

Figure 5.7: Plot depicting the mass loss measurements in pre-melt synthesis and following thermal trials

As verified in the last column of **Table 5.4** the mass loss is minimal, indicating all the mass loss measured during application of electrical inputs are electrochemical, as well as the remarkable thermal stability of the electrolyte. No significant mass loss of the electrodes was observed in the thermal only trials, confirming the following:

1. Negligible oxygen contamination in the furnace atmosphere, which would have resulted in mass loss of the graphite electrodes due to reaction with oxygen resulting in CO/CO_2
2. Negligible solubility of carbon in the electrolyte solution

These results are in alignment with the mass loss of the electrolyte samples from the pre-melt stage. After being held at a temperature of 1350 °C for 60 mins in the Mellen furnace, each of the pre-melt also consistently shows virtually no mass loss at about 1 mg or 0.5%.

No metallic deposition was observed when the electrolyte cross-section was examined under the optical microscope and SEM. The absence of any metallic deposit formation when no electrochemical signals were applied, suggests the thermodynamic stability of each of the constituents of the electrolyte in the molten state under the operating conditions including temperature and electrode assembly. This confirmed no carbothermic reduction (in case of minor oxygen contamination) nor any thermal reduction having occurred. **Figure 5.8** depicts the optical and scanning electron micrographs of the electrolyte subjected to thermal decomposition.

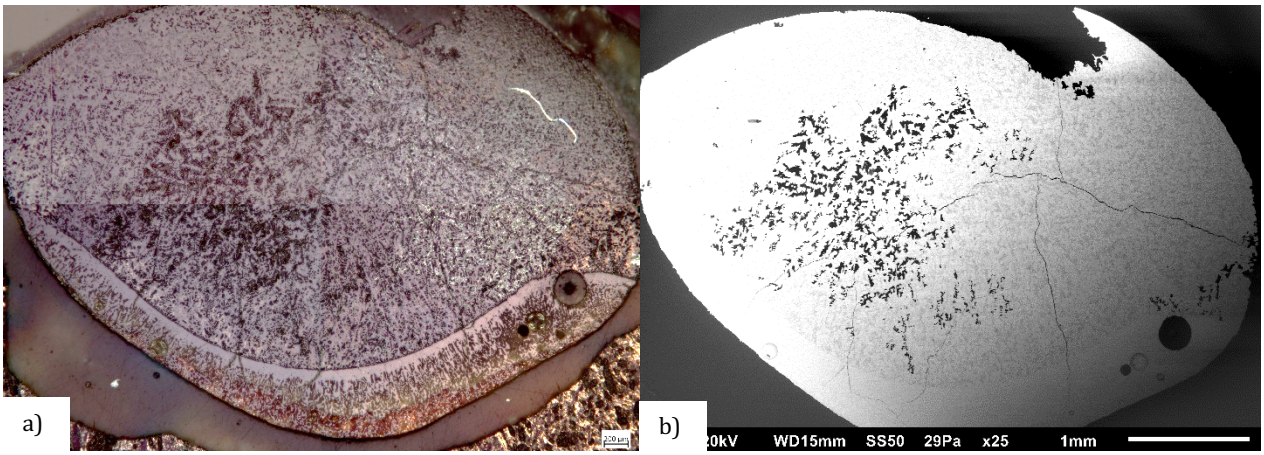

Figure 5.8 (a) Optical and (b) SEM micrograph of electrolyte sample subjected to thermal decomposition test

5.2.3 Electrolytic reduction on a graphite cathode

Electrolytic reduction was performed at varying current densities of 1.7 A/cm^2 and 0.85 A/cm^2 by setting the current at 300 mA or 150 mA, using the droplets of Table 5.4 as starting electrolytes. **Figure 5.9** below depicts gas bubbles observed during electrolysis, plausibly indicating S_2 evolution.

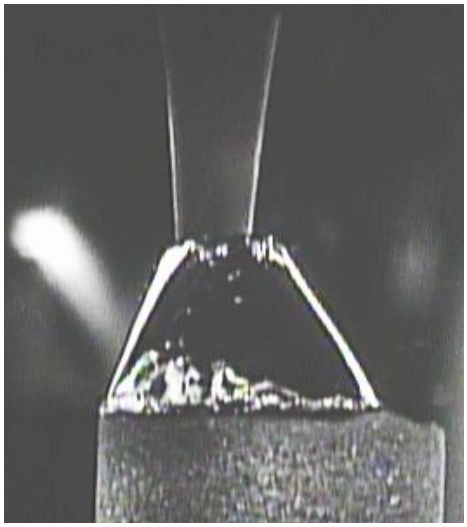

Figure 5.9 Evidence of gas bubbles observed during electrolysis, plausibly indicating S_2 evolution

5.2.3.1 Electrochemical signals

With evidence from the electrochemical signals and optical and scanning electron micrographs showing depletion of Fe in the electrolyte, it can be concluded that the Fe deposition occurring is a result of electrolysis.

The choice of the current to be applied to perform electrolytic decomposition of FeS was arrived at by the following method. Galvanostatic measurements were performed at different currents ranging from 0.0125 A to 0.55 A. The corresponding measured cell voltage variation with time are plotted in **Figure 5.10**. The plot in **Figure 5.10** depicts the actual recorded cell voltage and is not corrected by the IR drop, R being the ohmic resistance measured between the electrodes at OCP using EIS prior to electrolysis. Three ranges of current can be distinguished from the observed trends in cell voltage;

(i) Below 0.1 A, the cell voltage is less than the thermodynamic minimum decomposition potential

(ii) Between 0.1 A and 0.4 A, the cell voltage is between the thermodynamic minimum and 0.9 V [decomposition potential range including the IR drop and over potential]

(iii) Above 0.4 A, the cell voltage is greater than 1 V.

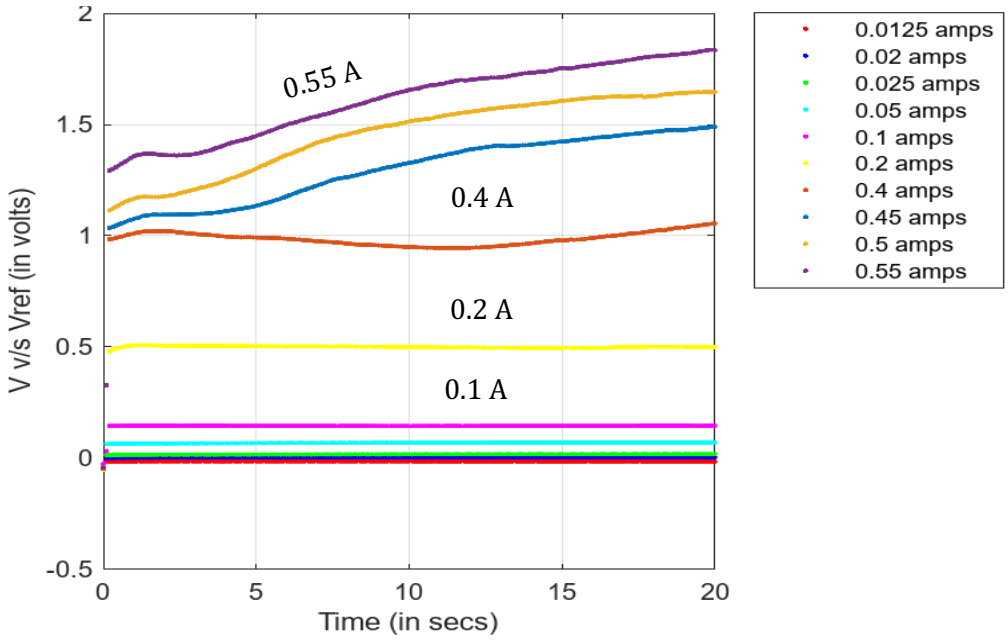

Figure 5.10: Galvanostatic measurements carried out measuring variation of Voltage v/s V ref with time at different current values.

Thus, these measurements served as a good reference for deciding the range of current to be applied to perform electrolysis, (0.1 A – 0.4 A). Thus, 2 values of 0.15 A and 0.3 A were chosen by considering the resulting current density, to study as they yielded cell voltages in the range of the minimum thermodynamic decomposition potential.

Accounting for the overpotential was out of scope of this work due to the absence of a reference electrode. Hence, for the sake of simplicity, the effect of overpotential was ignored. However, this assumption is reasonable due to the following reasons:

1. High concentration of the reactant ions in the electrolyte, the activity ratio between the electrode surface and the bulk is assumed to be about one. Additionally, the minimal amount of time the current is passed, is insufficient to fully deplete the region next to the electrode leading in a concentration gradient. This leads to the overpotential due to mass transfer of the ionic species to be negligible as compared to the product gas.

2. Since the operating temperature is greater than 1300° C, it can be assumed that the electrolysis is not limited kinetically. Hence, the contribution of the charge overpotential can also be ignored.

Chronopotentiometry scans (constant current of 0.3 A and 0.150 A) are shown below in **Figure 5.11** and **5.12** for experiments done at different current values for various durations. All cell voltages depicted in the plots are the actual recorded cell voltages and are not corrected by the IR drop. The voltage v/s time plots show the deposition voltage for Fe to be around 0.4 - 0.5 V, close to the thermodynamic minimum. The cell voltage is observed to increase as the time increases. The following are plausible reasons for the observed phenomena:

1. As the reaction progresses, it becomes thermodynamically challenging for the subsequent removal of the sulfur due to the remaining Fe ions binding more strongly with the remaining sulfur[4].
2. Accumulation of S_2 gas bubbles around the anode tip, which might be the cause for increased resistance in the system.

3. As the electrochemical reaction proceeds leading to deposition of Fe at the cathode, it must be providing an alternate low-resistance path for the electrons to flow. Thus, it plausibly increases the ionic resistance due to generation of a low electronic resistance path. This system could then be proposed as a parallel resistor circuit with two resistance paths, ionic resistance and electronic resistance.
4. Depletion of the feedstock FeS from the system as the reaction proceeds leads to a change in the composition of the electrolyte. It was experimentally observed that after performing the electrolysis for long durations or higher current values (0.5 A), the electrolyte begins to solidify, while maintaining the same furnace power. Thus, since the flow of ions gets highly restricted in a viscous or solid electrolyte, it leads to an increase in the ionic resistance. Thus, if the above stated hypothesis is true, a continuous feeding of the feedstock to maintain the composition and a periodic removal of the generated products (Fe from the cathode and S_2 from the anode) is expected to sustain a constant cell voltage. However further investigation is needed to get a deeper insight into the system's response to the applied current and the mechanism of electrolytic activity.

Other observations included negligible variations of the voltage at lower current densities as compared to the higher current density. However, the plausible causes for the voltage fluctuations at higher current density to be higher could most likely be due to the formation, growth, and separation of the gas bubble from the anode[2,5]. These are depicted by arrows in **Figure 5.11** and **5.12**.

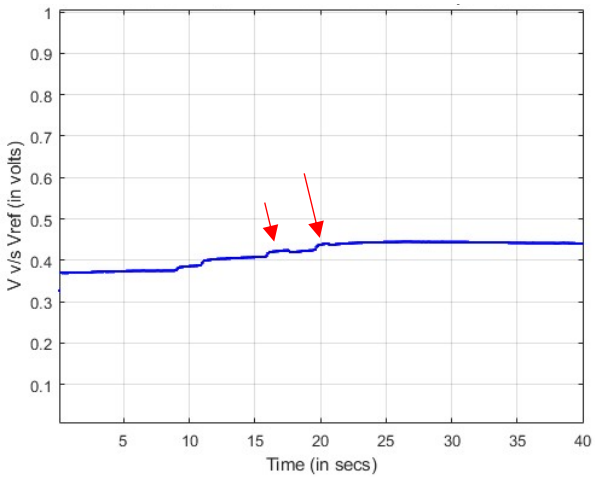

Figure 5.11: Variation of Voltage (V) v/s V ref with time – Chronopotentiometry curve for 0.15 A

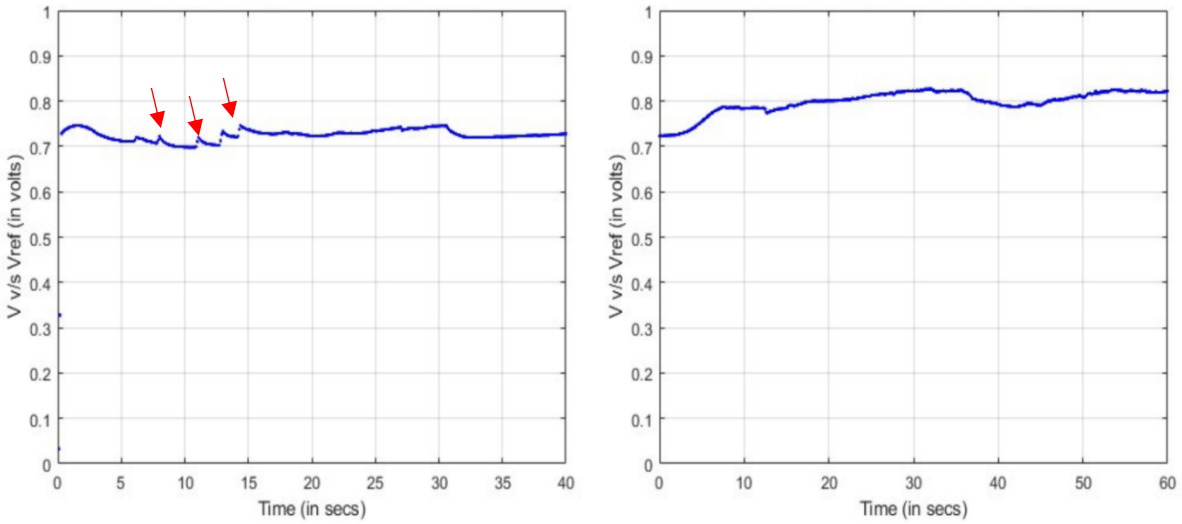

Figure 5.12: Variation of Voltage (V) v/s V ref with time – Chronopotentiometry curves for 0.3 A current

In some plots shown above, some sudden discontinuities are observed in the plot of potential as a function of time. They coincide with the slight adjustments of the anode height, resulting in a minute change of distance between the electrodes. Since the resulting change in voltage was significant, further studies about the variation of the impedance with distance between the electrodes and potential were carried out separately in the same operating conditions. Ideally, in an industrial electrolysis cell, due to the deposition of the metal product (since the liquid metal is not continuously, but periodically tapped), the distance between the electrodes decreases with time. Thus, the IR drop (ohmic overpotential) reduces, affecting the heat generated in the cell. To maintain the interstitial distance between the electrodes, the anode position can be constantly adjusted in the vertical direction by moving it upwards or away from the cathode, such as practiced for vertical carbon anodes in aluminum electrowinning. Moreover, the hot metal can be tapped more frequently as it is less sensitive to oxygen as compared to aluminum.

5.2.3.1.1 Factors affecting the impedance of the system

Figure 5.13 represents the variation of the impedance with the anode vertical position: the distances between the electrodes were controlled by moving the probe attached to the anode, up and down with a precision of 0.1 mm, controlled using stepper motors. As the distance between the electrodes increases, it is observed that the impedance also increases.

Based on the results as shown above, it can be concluded that the impedance of the system is extremely sensitive to the distance between the electrodes. This dependence is a feature of the electrolyte's resistivity and the experimental cell design, including the geometry of anode and cathode.

With the appropriate boundary conditions for current conservation, the electric currents physics model was evaluated to calculate the resistance of the system for the varying distance between the electrodes. The **Figure 5.14** shown below compares the values as calculated using the COMSOL model (see **Appendix 4** for details) and those experimentally obtained. A good agreement between the two values is observed along with a similar trend between the experimentally obtained values and those calculated using COMSOL. The little deviation could be attributed to the following factors:

1. Variation in the electrochemically active area of the anode: The anode used for experiments was not as perfectly machined as compared to the geometrical design used for the COMSOL model.
2. Isothermal conditions assumed in the model; highly likely in the TIF (limited hot zone)

These values were used to estimate the resistivity of the electrolyte, which approximately equates to **3.44 ohm-cm.** Prior work on Cu production via molten sulfide electrolysis of chalcopyrite involved similar studies resulting in the resistivity for $CuFeS_2$-BaS-La_2S_3 being **1.5 ohm-cm**. The comparatively lower resistivity can very likely be attributed to the presence of Cu_2S in the system.

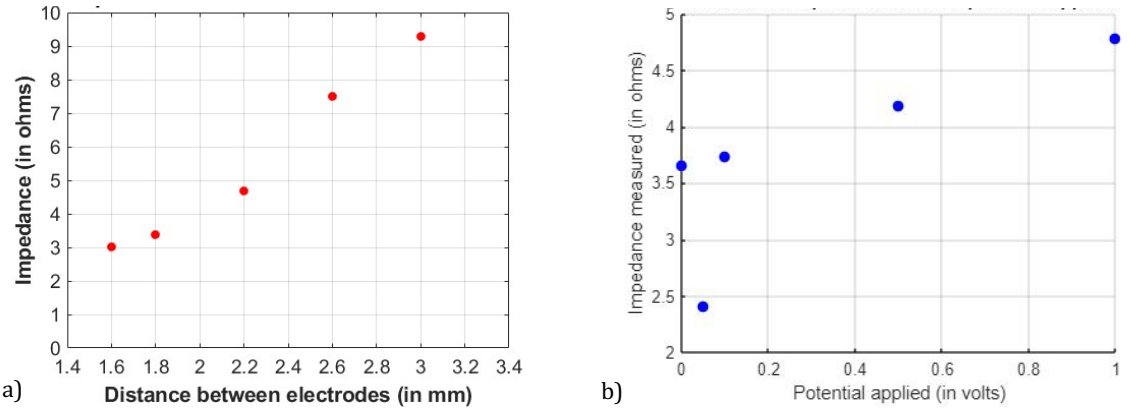

Figure 5.13: Variation of impedance with (a) distance between the electrodes (b) applied potential (in volts)

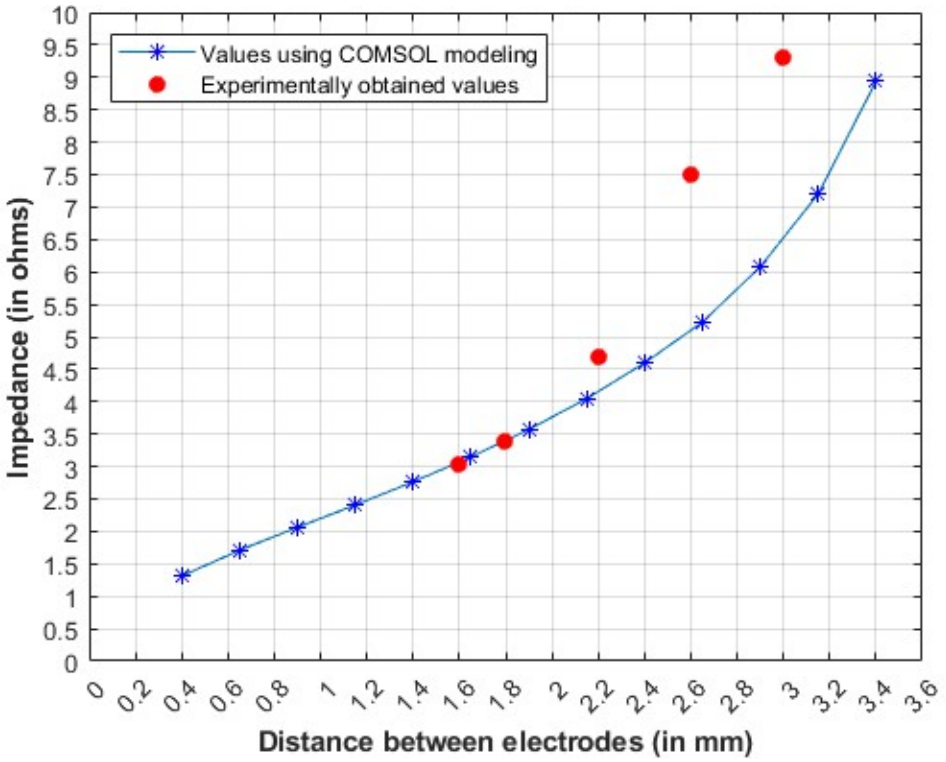

Figure 5.14 Plot comparing the experimentally obtained resistance values and those calculated using COMSOL

5.2.3.2 Mass loss and visual observations

Based on a visual observation of the quartz tube post experiment (see **Figure 5.15**), it can be confirmed that the electrolysis process resulted in sulfur gas produced at the anode.

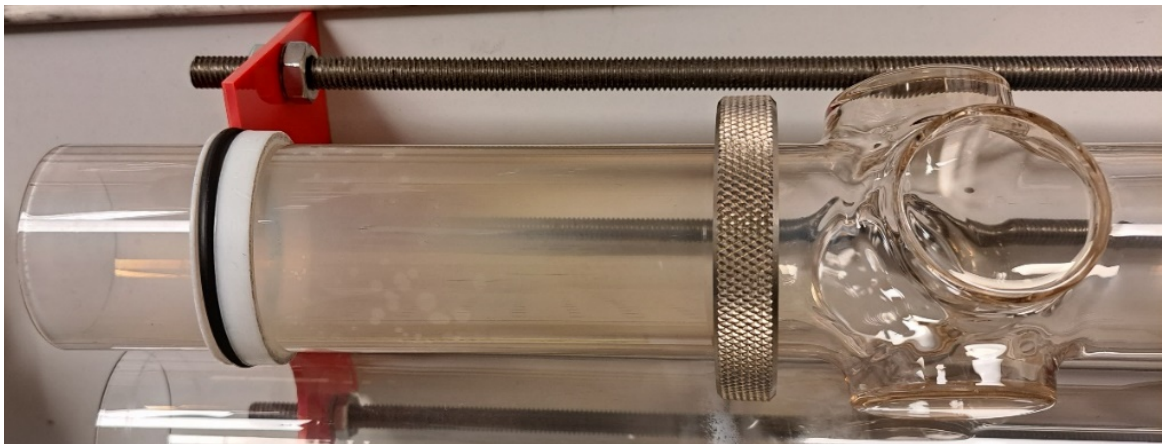

Figure 5.15: The top part of the quartz tube showing a yellowish tinge, serving as evidence of S_2 evolution (also confirmed by typical sulfur gas odor), presumably some of which condensed on the tube surface

After removing the quartz tube from the furnace, the top part of the tube showed a yellowish tinge, suggesting the S_2 gas that left the electrolyte condensed on the sides of the tube. This is due to the sides of the tube being cooler than the boiling point of S_2 (boils at 444.6 ◦ C). Moreover, there was also a residual odor of sulfur from the tube, serving as evidence of S_2 evolution.

The faradaic efficiency (anodic) was calculated based on the mass loss of the electrolyte as described in **section 4.3.1**. This is because all mass loss was attributed to the loss of sulfur from the system due to electrolysis, with corresponding metal production at the cathode observed by microscopy. In the range of the recorded cell voltage, only FeS is expected to electrolytically decompose while BaS and La_2S_3 remain, their decomposition voltages being comparatively higher than for FeS (see Ellingham-like diagram in **chapter 2, Figure 2.2** [6,7]). To confirm this and observe the elemental composition of the metallic deposits, optical and SEM microscopy was conducted after electrolysis, as discussed in **section 5.2.3.3**.

In cases where metal recovery is possible, the cathodic efficiency can be calculated in the same way as described in **section 4.3.1**, where the solidified metal mass recovered at the cathode is compared with the amount of Fe as predicted by Faraday's law for reduction of Fe^{+2}. Since metal recovery was not feasible at such small scales[2,7], only anodic efficiencies were calculated. **Table 5.5** below summarizes the results of the various electrolysis experiments depicting the mass change measurements and faradaic efficiency recorded.

Exp. No	Current (A) - duration (sec)	Initial mass (g)	Final mass (g)	Mass loss (g)	Faradaic efficiency (%)
01	0.3 – 20	0.197	0.196	0.001	100.3*
02	0.3 – 40	0.1969	0.1951	0.0018	90.3
03	0.3 – 60	0.1976	0.1947	0.0029	97.0
04	0.3 – 80	0.1971	0.1949	0.0022	55.2
04(ii)	0.3 – 2×40	0.1995	0.1955	0.004	100.3*
05	0.3 – 90	0.1964	0.1944	0.002	44.6
06	0.15 – 60	0.1975	0.1962	0.0013	86.9
07	0.15 – 90	0.1993	0.1956	0.0037	82.5
08	0.15 – 120	0.195	0.1931	0.0019	63.5

Table 5.5: Results of the electrolysis experiments carried out depicting the mass change measurements and faradaic efficiency

It is important to note that the estimated faradaic efficiency calculated above is contingent on the ability to completely recover the products or accurately measure the mass losses. As observed from the thermal decomposition studies, since the mass loss of the electrolyte was negligible due to thermal effect, in the above calculations, the thermal mass loss was not accounted for. The resulting mass loss is considered entirely due to the effect of electrolysis. The estimated efficiency is also observed to be dependent on the configuration of the electrolytic cell, such as the following:

* Estimated faradaic efficiency depends on the accuracy of the mass measurements. Hindrance in the recovery of the electrolyte happens if it sticks to the cathode, while scrapping off can pick up some material from the cathode

1. **Anode design:** The efficiency is reduced when the design of the anode is not optimal. For instance, when the anode tip is sharp and narrow, corresponding to a high anodic current density, the gas evolution is high initially, but the electrochemically active anodic area is quickly getting covered by the gas, inhibiting any further electrochemical activity. The cell configuration for an optimized efficiency would be one that balances the requirement of current density at the electrodes to carry out the necessary reaction as well as allows the release of gas to avoid blocking of the anode (reducing the active area) due to gas evolution.

2. **Distance between the anode and cathode:** This is a feature of the resulting resistance of the electrolyte system, that subsequently affects the ohmic drop, and the dynamics of bubbles evolution, which has a large influence on the interpretation. It was observed that the higher the distance between the electrodes in the electrolyte, the higher the resistance (as was also observed by L. Rush[4]). Notably three different types of observations were made upon electrolysis experiments and their plausible reasons are included below:

(i) When the electrode gap is small, the cell voltage recorded is close to the minimum thermodynamic potential for FeS deposition. However, no evidence of *electrochemical activity*[xiii] was observed. This correspond to a gap where the anode tip is below the center of the electrolyte droplet, very close to the cathode.

(ii) When the anode tip is inserted near the center of the electrolyte droplet, i.e., the distance between the electrodes is of the order of the radius of the electrolyte droplet, the cell voltage was transient. It remained close to the thermodynamic minimum for part of the experiment duration while continuously increasing. Hence, electrochemical activity would have occurred only for the experiment's duration when the increasing cell voltage went beyond the thermodynamic minimum, thus accounting for the ohmic (IR) drop or other sources of overpotential. Thus, this could be one of the reasons for the reduced faradaic efficiency in some cases. For instance, in an electrolysis experiment for 40 secs, in case the cell voltage remained equal to the thermodynamic minimum for about 10 secs. As it continued to increase, it went beyond the minimum only in the latter 30 secs, during which we can assume

[xiii] (gas bubbling, Fe deposits; oxidation or reduction henceforth referred to as *electrochemical activity*)

electrochemical activity to have occurred for only 30 secs as opposed to 40 secs. Thus, this plausibly translates to the reduced faradaic efficiency calculated for the entire 40 secs.

(iii) Only when the distance between the electrodes was greater than the radius of the droplet (i.e., the anode was inserted up to the center of the droplet), was the faradaic efficiency calculated close or above 90% for each experiment. In this case, the recorded cell voltage was significantly higher than the thermodynamic minimum, 0.7 to 0.8 V.

This suggests that the IR drop, controlled by the electrode gap, is linked to the recorded cell voltage. The higher the electrode gap, the higher is the IR drop and hence the cell voltage. One plausible hypothesis for the reduced faradaic efficiency at lower distance between the electrodes, could be due to accumulation of S_2 bubbles around the anode tip, resulting in ceasing any further electrochemical activity till the bubbles have sufficient time to escape. Hence, even though the recorded cell voltage was close – though greater - than the thermodynamic minimum, there is very high chance of the initially released S_2 bubbles to be accumulating around the anode. The electrode gap being too small, there are multiple plausible explanations can be proposed:

1. Bubbles cover the anode and cease further electrochemical activity till they get sufficient time to escape. Moreover, since the size of the S_2 gas molecules is large, there is an inherent mass transport limitation, i.e. higher resistance to transport through the electrolyte. Ideally, in such a scenario, it is expected that electrochemical activity would resume once the anode is cleared off the bubbles, however since the duration of the experiment is short, we do not observe this taking place. Evidence supporting this hypothesis is presented later. In the case of 0.15 A (lower current density), the effect of distance between the electrodes observed was less as compared to 0.3 A (higher current density). The plausible explanation for this observation could be the higher reaction rate in the case of higher current density leading to more vigorous bubbling and hence gas accumulation around the anode. So, controlling the electrode distance was a very sensitive parameter affecting the faradaic efficiency in this case. Even a little increase in the distance allowed the S_2 molecules to escape, and thus proportionally increasing the distance between the electrodes up to a certain

limit, a trade-off with the increasing IR drop, led to higher faradaic efficiency. However, in the case of lower current density, this sensitivity to the electrode distance was comparatively less.

2. Back reaction of the released S_2 molecules with the Fe deposited to form FeS, as a result of the electrolyte around the anode being solubilized by sulfur. This would result in a lower to no net electrochemical activity observed. Although, the S_2 gas encountering the reduced metal can be prevented by a better cell design.

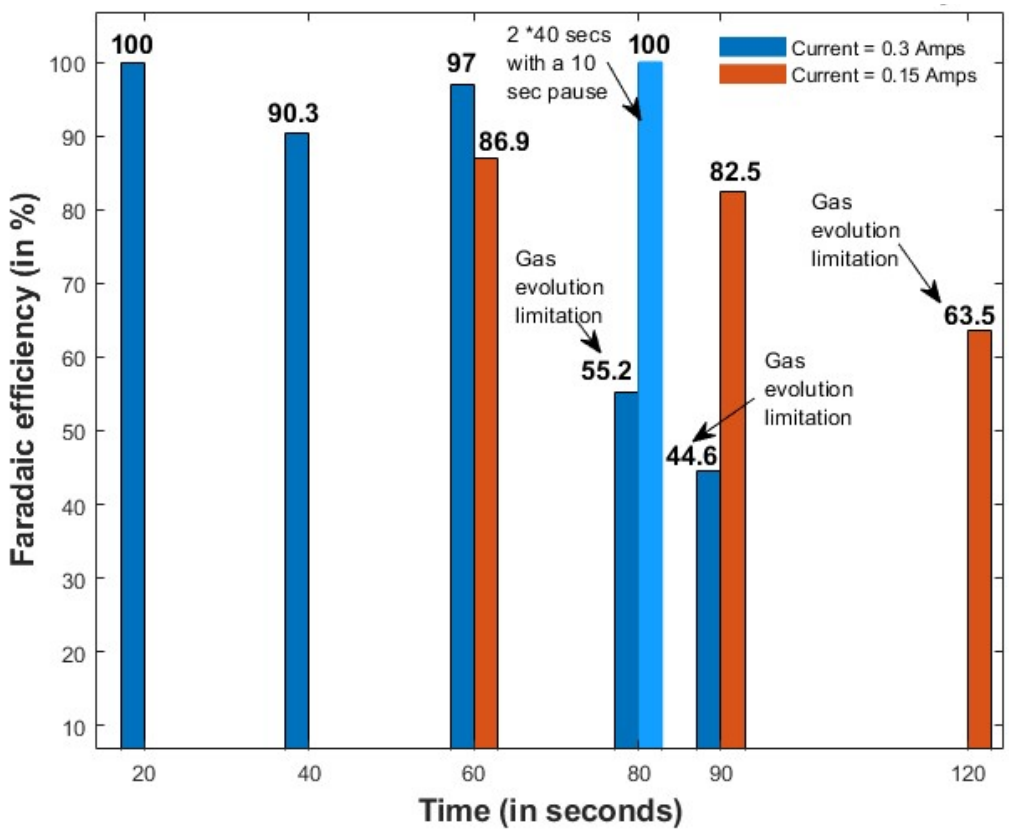

Figure 5.16 (a): Chart depicting effect of time and current on the faradaic efficiency calculated for the electrolysis experiments

According to the experimental observations, if the resulting potential is close to the thermodynamic minimum for FeS decomposition, the efficiency is observed to be negligible due to the possibility of the above stated hypotheses. Only when the recorded cell potential is higher than the decomposition potential, the resulting efficiency is close to 90% or above. The chart in **Figure 5.16** captures the effect of the time and current density on the experiment's faradaic efficiency.

As observed from the chart above, the efficiencies recorded for a current of 0.15 A are slightly less as compared to experiments where a current of 0.3 A was passed. This is because a higher polarization is induced with a higher current density, leading to an increased driving force for any chemical reaction to occur. The rate of reaction was qualitatively observed to be higher in 0.3 A as compared to 0.15 A. The video recording in-situ electrolysis showed bubble formation earlier as well as more vigorous in the former as compared to the lower current density case.

There is an interesting feature that was observed while studying the effect of current density in the electrolysis experiments. For experiments in which a current of 0.3 A was passed, the efficiency dropped to almost half after 60 seconds of electrolysis. As seen in the chart above (see **Fig. 5.16 (a)**), for all times less than 60 seconds, the efficiency recorded is 90% and above, except for those experiments with an electrolysis duration greater than 60 seconds (80 seconds and 90 seconds). From a visual observation in-situ electrolysis (recorded using the camera), a vigorous bubbling was observed at the anode during the time the current was passed, indicating a reduction in the electrochemically active area due to the gas bubbles blocking the anodic surface area till sufficient time was allowed for the gas bubbles to escape. Additionally, due to diffusion of the ionic species from the bulk electrolyte to the electrodes and later of the S_2 gas away from the anode, there is a likelihood of a spatial gradient in the electrolyte composition.

This hypothesis was tested in a separate experiment where the electrolysis duration was done in 2 steps with a 10 sec inactive period between them. This was done for the system to reach equilibrium once the S_2 gas bubbles escaped away from the cathode, allowing to remove bubbles surrounding the anode each time the current was passed. Electrolysis during a total of 80 secs resulted in an efficiency of 44.6%. With a sequence of 40 secs with current, a 10 secs gap, and 40 additional seconds passing current – totaling 80 secs of electrolysis time, resulted in an efficiency of 100%. This most likely shows the effect of the gas bubbles around the anode, and the importance of the cell configurational design to support efficient gas removal. This was also the reason experiments with lower current density were performed for longer electrolysis duration. To simplify the comparison, the current density was halved to study its effect for double the electrolysis time. According to

the theory discussed above, the effect of the gas evolution limitation in a lower current density case is expected to occur at higher electrolysis duration. For instance, the gas evolution limitation was observed at experiment duration greater than 60 secs in the case of 0.3 A of current. Hence, for the same amount of gas to be released, this limitation is expected to occur at double the time (i.e., 120 secs) when operating at half the initial current density value (i.e., 0.15 A). As seen in the chart, the efficiency for time of 120 secs (0.15 A), indeed drops down as compared to 60 secs or 90 secs. Thus, the experimental results observed were in high coherence to the theory discussed.

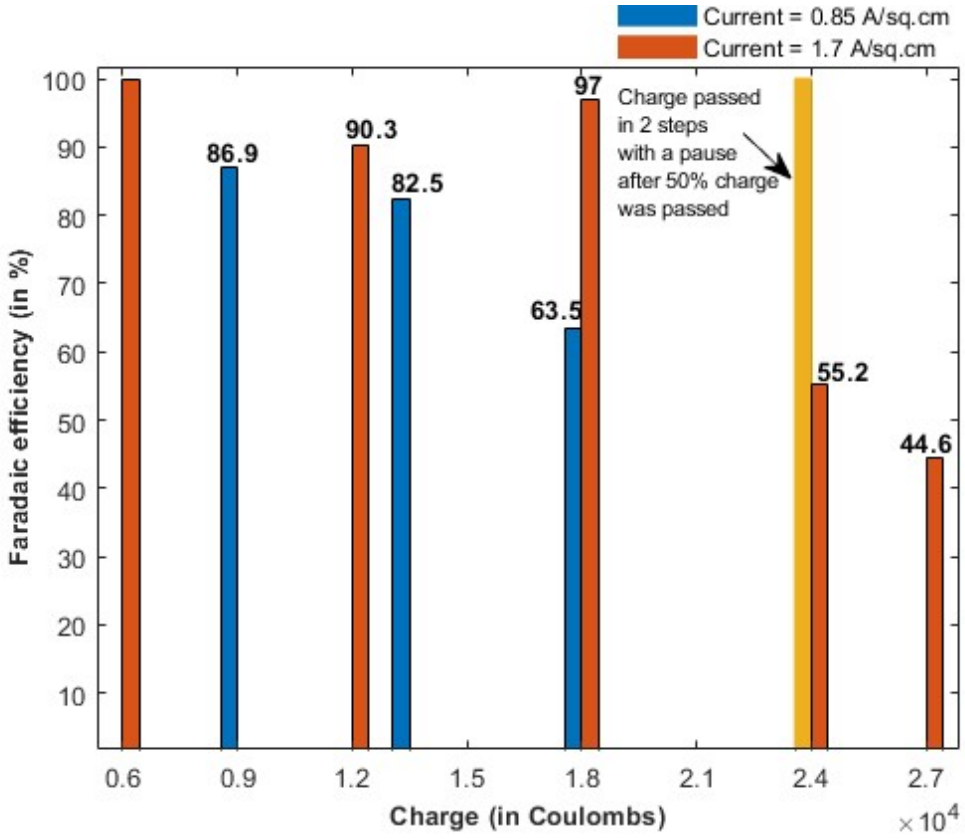

Figure 5.16 (b): Chart depicting effect of current density on the faradaic efficiency

When recast as a plot of faradaic efficiency versus charge, as shown in **Figure 5.16(b),** it becomes clear that this is not a limitation of the process by itself, but of the cell design. For a similar charge (e.g., 18000 C), higher efficiency is recorded at higher current density, clearly indicating that the process is tolerant to high reaction rates. The same can be concluded based on the point corresponding to 24000 C, though the same current density is maintained, just by changing the method of operating the cell, high efficiency was observed.

With these results, it can be concluded that the efficiency is highly dependent on the cell configuration, which itself dictates the mass transfer conditions for the anodic and cathode reaction. While the effect of time on the efficiency observed is critical, it is a feature of this specific set-up and is expected to be managed during the design of industrial scale cells. During the inactive period, the lamps were still powered at the same intensity, to avoid the electrolyte from losing heat and solidifying, thus assuming the operating conditions remained unchanged between the 2 current passage cycles. However, this cannot be replicated in an industrial setup since the cell is engineered to be self-heated by the flow of current through the resistive electrolyte. Switching off the current in between would result in a sudden temperature drop in the electrolyte, resulting in either a change in the operating conditions when the flow of current is re-established (lower temperature, higher viscosity of the electrolyte), or electrolyte solidification in extreme cases. The experimental study of the effect of time was performed only to show the dependence of the estimated efficiency on the cell design.

Nevertheless, a major takeaway is the high efficiency of the process, resulting from FeS being the sole iron sulfide stable (+2 being the dominant valency for iron in the electrolyte) at high temperature and low partial pressure of oxygen[7]. This is significant as the multi-valency of iron has afflicted previous electrolytic systems dealing with iron[8]. Additionally, the high solubility of the feedstock in the electrolyte, up to 10 wt.%, (as compared to in other electrolysis processes, e.g., Al production) also ensures the high faradaic efficiency, along with establishing a molten electrolyte.

5.2.3.3. Further characterization studies

The optical and SEM micrographs of the electrolyte sample are shown below in **Figure 5.17** Tiny droplets of metal are observed at the bottom, where the electrolyte contacts the graphite cathode, confirming electrolytic reduction of FeS. SEM-EDS analysis does not indicate reduction of BaS or La_2S_3; only FeS is decomposed. Fe metallic deposits are observed with an average size of 20 microns, with a few deposits of up to 50-micron size.

However, due to surface tension effects (usually observed at such small scales) and as a result of solidification, the Fe metallic deposits produced were dispersed at the bottom of the electrolyte, found all along the cathode curvature. Due to this, the metal recovery was hindered[2,7], preventing calculation of the cathodic faradaic efficiency.

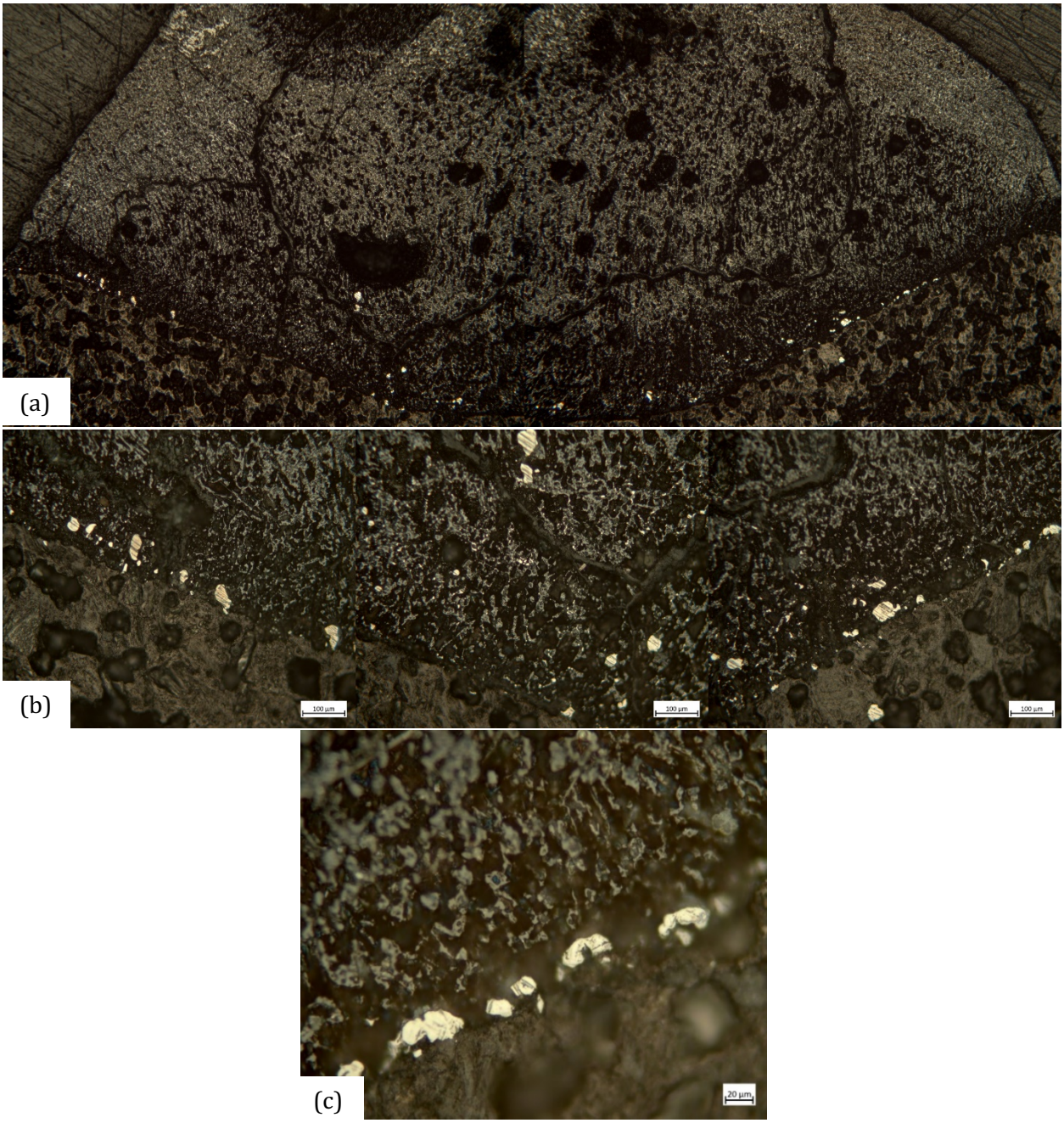

Figure 5.17: Optical micrographs depicting cross-section of the electrolyte on a graphite cathode showing Fe deposition after electrolysis at (a) 2.5X (b) 10X (c) 25X

Some of the metallic deposits are observed at the center of the electrolyte and detached from the cathode most likely floated up when the electrolyte and the metal were in the liquid state and stayed there when the sample was quenched. When observed under the SEM, three regions are identified, with different sulfide composition, though usually a mixture of 2 phases in addition to possibly the Fe metallic phase:

(i) anode is inserted (ii) middle/bulk electrolyte (iii) region near the cathode.

It is important to note here that the phases observed may not necessarily represent the phases present during electrolysis. The phase portioning can also result due to the non-equilibrium cooling and solidification. Though the sample was quenched to retain the phases formed during electrolysis as it is, the graphite cathode holds some heat even after the lamps are switched off, resulting in some phase segregation due to the thermal dissipation. In **Figure 5.18**, the light-colored regions contain La rich phases whereas the Ba rich phases appear dark in the SEM micrograph, confirmed using both EDS and WDS analysis. Performing an EDS analysis over an area, it was observed that the region in contact with the cathode, especially in regions next to the deposit, are depleted in Fe.

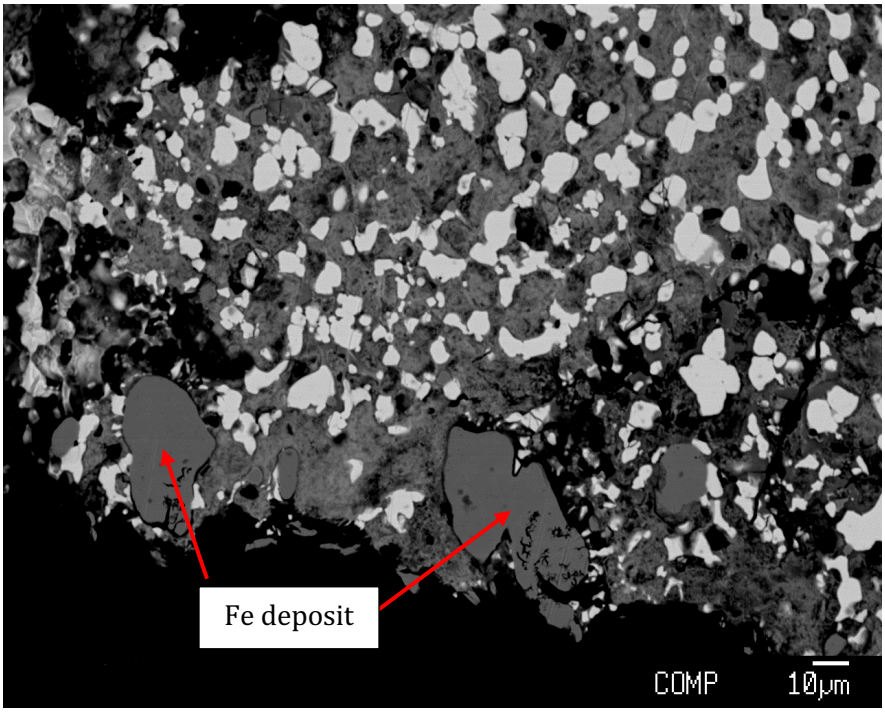

Figure 5.18: WDS-SEM micrograph [II] of the electrolyte sample after electrolysis distinctly showing the light and dark phases and the metallic Fe deposits

Line EDS analysis scans shown in **Figure 5.19** reveal almost no Fe concentration in the sulfides that surrounds Fe deposit. These scans reveal the simultaneous depleted or absence of signal for other elements such as S, Ba and La as we go closer to or within the Fe deposit.

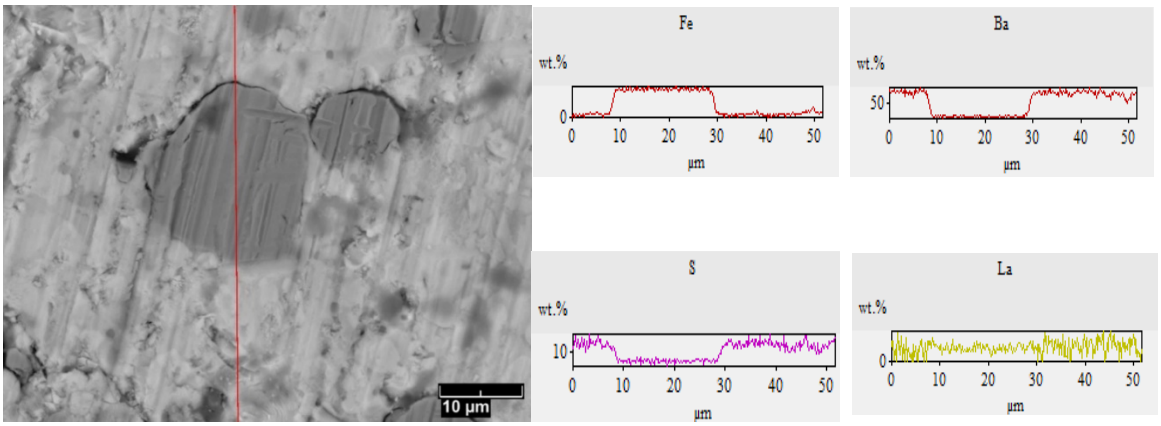

Figure 5.19: Line scans performed during EDS analysis of the electrolyte sample through a Fe deposit

Table 5.6 below shows the relation between the concentration of Fe and the Ba/La in the electrolyte. The values observed are from the SEM-EDS analysis over an area providing the average value in the different regions of the electrolyte – near the anode insertion, bulk of the electrolyte and surface near the cathode respectively.

Fe	Ba/La
6.06 wt.%	1.83
4.89 wt. %	1.77
4.54 wt. %	1.57
3.93 wt.%	1.36
2-3 wt.%	0.83
0.85 -1.77 wt.%	0.6

Table 5.6: Relation between the concentration of Fe and the Ba/La in the electrolyte, similar Ba/La ratios recorded upon WDS analysis [II]

It is observed that, in the solidified sulfide electrolyte, Fe is found in phases that are rich in Ba, i.e., phases rich in Fe were correspondingly rich in Ba also. The Fe concentration

in the electrolyte was studied together with the Ba/La ratio in the phases. The direct proportionality between Fe concentration and the Ba/La was observed in each region, i.e., as the Fe reduced, the Ba/La ratio also decreased. This is interpreted as indication of the role of mass transport during electrolysis.

The Fe depletion which occurs due to electrolysis, leads to the formation of a Ba rich sulfide phase. This compositional inhomogeneity locally affects the electrical and other transport properties for further electrolysis to occur. Since the temperature is controlled at the eutectic range of Ba and La sulfide, the formation of the Ba rich sulfide phase results in a solid precipitate[2], due to increase in melting point as the concentration of BaS increases, thus inhibiting further electrolysis even if there is any remaining FeS. The solidification of the electrolyte was experimentally observed at longer durations of electrolysis or higher current densities (~ 2.83 A/cm^2, 0.5 A), while the furnace power was kept the same. **Figure 5.20** depicts solidification of an electrolyte after 120 secs of passing 0.5 A. It can be hypothesized that these conditions lead to a depletion of FeS in the electrolyte and hence may have led to the composition of the electrolyte drifting from the eutectic point.

This is an artefact of the present experimental setup, which is not designed to be continuous. In a continuous reactor, continuous feeding of the feedstock will ensure the composition of the electrolyte is maintained throughout the electrolysis. However, further work needs to be done to quantitatively determine the minimum level of FeS which needs to be present in the electrolyte at all times to keep the electrolysis functioning continuously.

Figure 5.20: Solidification of the electrolyte as observed after 120 secs of passing 0.5 A

This will help determine the feeding rate of FeS. This work will also require the FeS-BaS-La_2S_3 ternary phase diagram to determine the eutectic composition range, which is out of scope of this work.

Figure 5.21 shows the element intensity map of the bottom region of the electrolyte after electrolysis confirming that the metallic deposits seen in the optical and SEM micrographs (analyzed at the same location) are indeed concentrated in Fe.

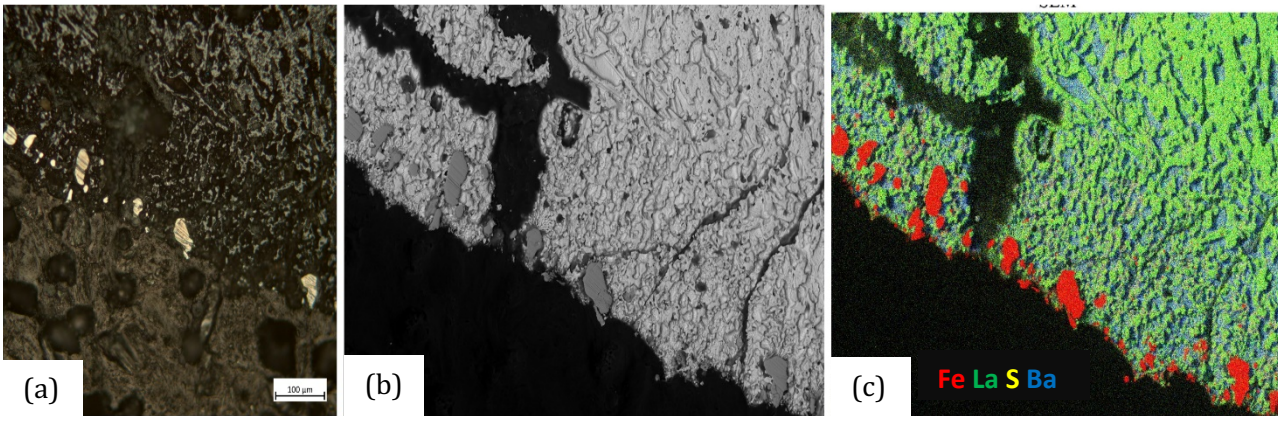

Figure 5.21: (a)Optical micrograph (b) SEM micrograph and (c) element intensity map of the electrolyte sample after electrolysis distinctly showing the metallic Fe deposits

For the S concentration, WDS analysis [II] was conducted, which results are presented in **Table 5.7** The carbon concentration was not estimated using WDS due to practical difficulties. However, since the WDS analysis did not report presence of Ba or La, the carbon concentration can be estimated as 100 – (Fe wt.% +S wt.%).

Element	Weight Concentration
Fe	94.55 wt.%
S	0.05 wt.%

Table 5.7: Results of WDS analysis [II] of the observed metallic deposit

The exact composition of the metallic deposit in terms of C concentration was however difficult to perform due to the size of the deposits and difficulty in recovery.

To get a true qualitative estimate of the carbon, the electrolyte sample was etched to reveal the underlying microstructure and compare it with other Fe-C alloy systems. As seen

in the **Figure 5.22**, a few of the Fe deposits, in contact with a graphite cathode, show the presence of carbide-like inclusions.

From the micrographs depicted in **Figure 5.23**, it is clear that the microstructures revealed after etching, look similar to those of an Fe-C alloy system, specifically the pearlite phase. Observing the shape of the inclusions it can be concluded that they are iron carbides (cementite phase). Since, the ferrite phase was not observed, we can conclude that the metallic deposits are highly likely to be a high-carbon alloy, showing the pearlite phase and cementite (Fe_3C). Each of these deposits were in contact with the graphite cathode, thus the formation of these phases occurred as a result of Fe-C equilibrium when Fe was electrolytically deposited over the graphite cathode. **Figure 5.22** shows the optical micrographs of the metallic Fe deposits after etching with 4% Nital solution.

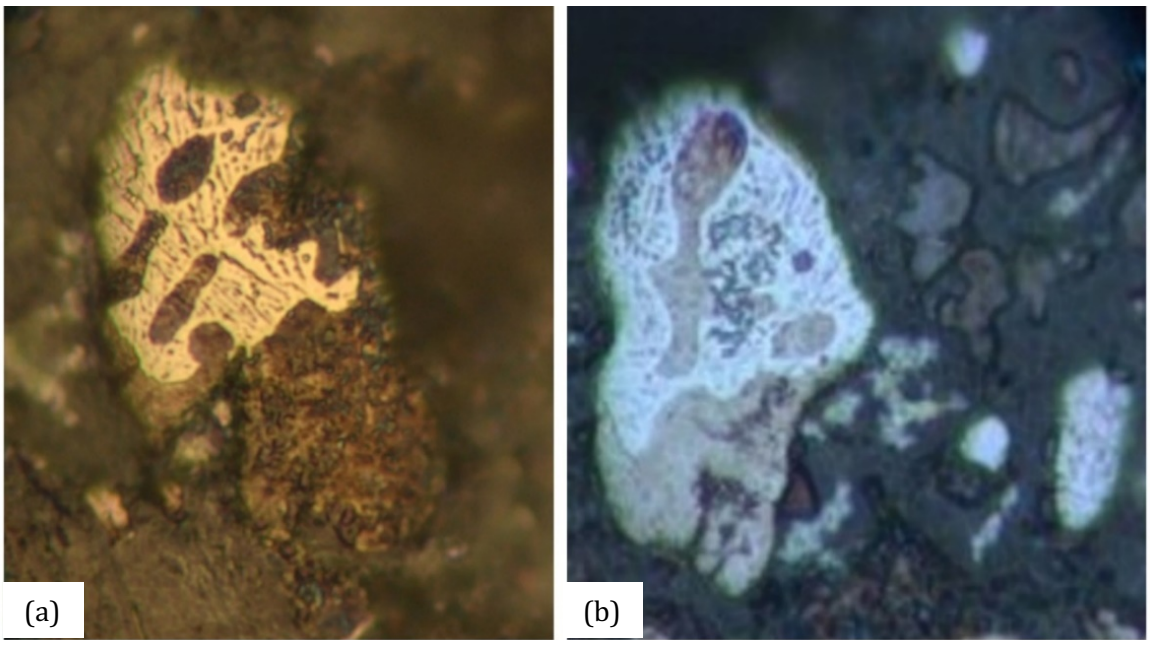

Figure 5.22: Optical micrographs of Fe deposits, after etching the sample with 4% Nital solution (a, b) metallic deposits at 50 X

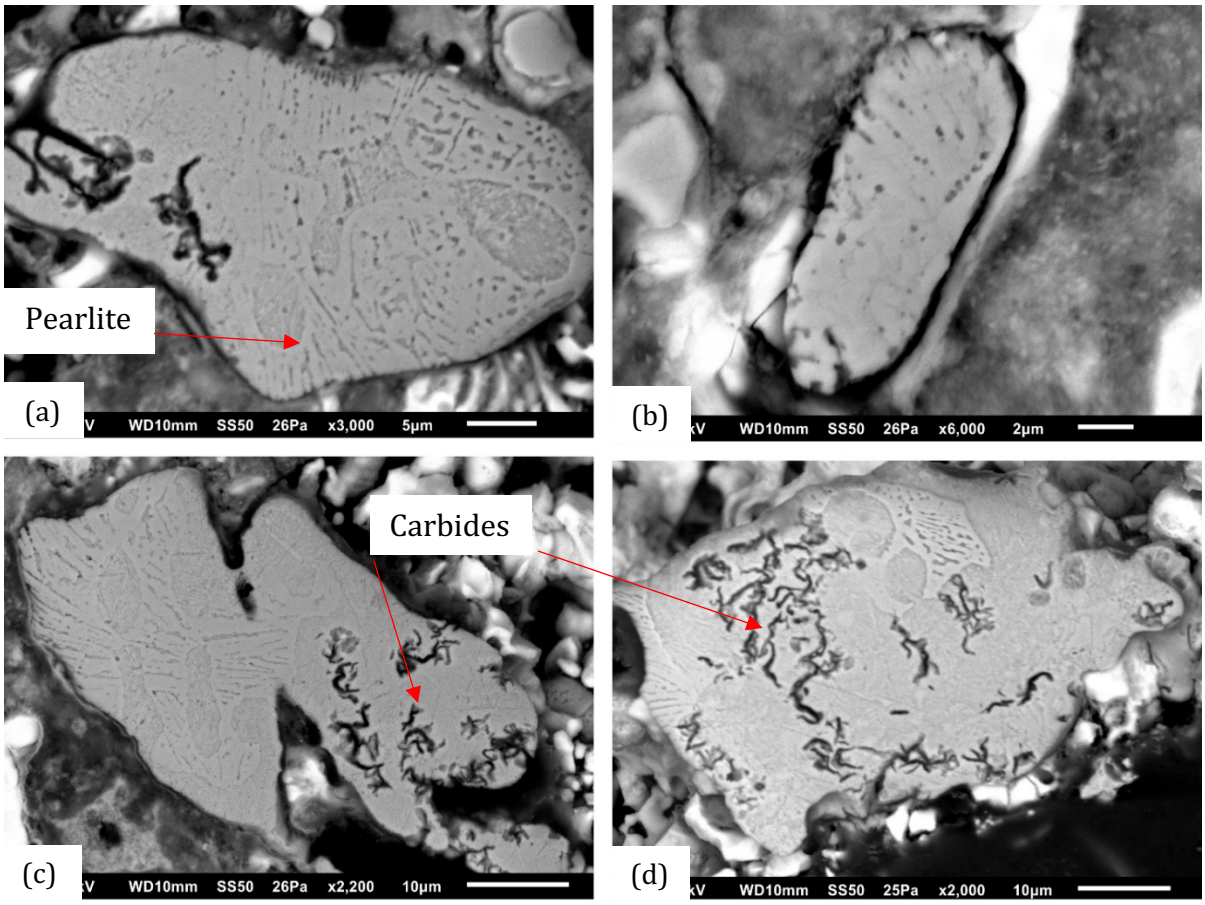

Figure 5.23: SEM micrographs of Fe deposits, after etching the sample with 4% Nital solution, showing carbide inclusions (a) deposit -1 at 3000 X (b) deposit -2 at 6000 X (c) deposit-3 at 2200 X (d) deposit-4 at 2000 X

Table 5.8, shown below, shows the results of the ICP analysis [I] to confirm that the mass loss in the electrolyte aligns with the depletion of sulfur before and after electrolysis. A mass loss of 0.0018 gms was observed corresponding to a difference of 0.9 wt.%. The ICP [I] results are thus in alignment (0.85 wt.%) with the fact that mass loss occurs only due to sulfur loss.

Sample	S content
Before electrolysis	15.65 wt.%
After electrolysis for 40 secs	14.80 wt.%

Table 5.8: Results of ICP [I] analysis comparing the difference in S content before and after electrolysis

5.3 Summary

This chapter discussed the observations and results of the sulfidation, and the electrolysis experiments performed. It includes qualitative and quantitative discussions of the various characterization studies performed namely:

1. Sulfidation experiments:
    a. Mass loss measurements versus stoichiometric calculations were performed, which concluded a 100% conversion from oxide to sulfide
    b. Optical microscopy: Shiny and porous sulfide particles as observed under the optical microscope.
    c. SEM microscopy and EDS: Analyzed the elemental distribution in the sulfide particles, to reveal the slight off-stoichiometry of the compound ($Fe_{0.9}S$)
    d. XRD: Showed negligible amounts of the starting iron (+3) oxide, with major peaks for FeS

2. Molten sulfide electrolysis experiments:
    a. Faradaic efficiency calculations from mass loss measurements: Anodic efficiencies of greater than 95 % were observed by the mass lost from the electrolyte after passing current through it. The mass loss due to sulfur was confirmed using ICP analysis of the samples before and after electrolysis
    b. Visual observations: Concluded the gas evolved during electrolysis to be sulfur due to the observation of a pungent smell and yellow color of the condensate deposited on the quartz tube
    c. Electrochemical signals: Galvanostatic measurements were carried out to find the optimal range of current for the decomposition reaction, followed by constant current tests for varying times and current densities. Further studies were carried out to find the various factors affecting the impedance of the system, to reveal the system's impedance being extremely sensitive to distance between the electrodes and the voltage applied.

d. Optical and SEM microscopy: Analyzed the phase separation and Fe deposits. Sulfur concentration in the Fe deposit was confirmed using WDS analysis. Sample was etched to reveal the microstructure of the metallic deposit to be similar to that of a high carbon Fe alloy, due to presence of pearlite phase with carbide inclusions.

Thus, the above results depict the successful demonstration of the molten sulfide electrolysis to produce Fe with some key insights of the process.

5.4 References

(1) Stinn, C. Pyrometallurgical Oxide-Sulfide Anion Exchange for Improved Material Separation and Metal Production, 2023. https://hdl.handle.net/1721.1/151594.

(2) Sokhanvaran, S.; Lee, S.-K.; Lambotte, G.; Allanore, A. Electrochemistry of Molten Sulfides: Copper Extraction from BaS-Cu 2 S. *Journal of The Electrochemical Society* **2015**, *163*, D115–D120. https://doi.org/10.1149/2.0821603jes.

(3) Boury, C.; Allanore, A. Liquid State Properties and Solidification Features of the Pseudo Binary BaS-La2S3. *Sci Rep* **2021**, *11* (1), 18189. https://doi.org/10.1038/s41598-021-93576-z.

(4) Rush, L. Integrative Approach to Metal Extraction and Electrification, 2021. https://hdl.handle.net/1721.1/140135.

(5) Einarsrud, K.; Eick, I.; Bai, W.; Feng, Y.; Hua, J.; Witt, P. Towards a Coupled Multi-Scale, Multi-Physics Simulation Framework for Aluminium Electrolysis. *Applied Mathematical Modelling* **2016**, *44*. https://doi.org/10.1016/j.apm.2016.11.011.

(6) Sahu, S.; Chmielowiec, B.; Allanore, A. Electrolytic Extraction of Copper, Molybdenum and Rhenium from Molten Sulfide Electrolyte. *Electrochimica Acta* **2017**, *243*. https://doi.org/10.1016/j.electacta.2017.04.071.

(7) Daehn, K.; Stinn, C.; Rush, L.; Benderly-Kremen, E.; Wagner, M. E.; Boury, C.; Chmielowiec, B.; Gutierrez, C.; Allanore, A. Liquid Copper and Iron Production from Chalcopyrite, in the Absence of Oxygen. *Metals* **2022**, *12*, 1440. https://doi.org/10.3390/met12091440.

(8) Allanore, A. Features and Challenges of Molten Oxide Electrolytes for Metal Extraction. *Journal of the Electrochemical Society* **2014**, *162*, E13–E22. https://doi.org/10.1149/2.0451501jes.

Details of the external services used for material analysis:

I. ICP: Lehigh Testing Laboratories, 308 West Basin Road, New Castle, DE 19720
II. WDS: Electron Microprobe facility, Department of Earth, Atmospheric and Planetary sciences, Massachusetts Institute of Technology, Cambridge, MA 02139
III. LECO: Applied Technical Services (ATS Lab), 1049 Triad Court, Marietta, GA 30062

Chapter 6

Conclusion and future work

6.1 Conclusion

Steel has been and will continue to be the highest consumed metallic material globally due to its impeccable properties empowering its wide variety of applications[1,2]. With over 2 orders of magnitude difference in steel production as compared to other metals[3,4], iron and steel making has been very well studied and executed. The state-of-the-art technology of the blast-furnaces and BOFs[5,6], a classic example of productivity and quality, has nearly peaked thermodynamic optimization in terms of energy usage. This means that no further significant reduction in energy requirement is possible through this route. No doubt this technology, based on carbothermic reduction, has enabled massive production volumes satiating the global demand, but is faced with a plethora of economic and environmental challenges[5,7]. The steel industry accounts for **11%** of the global carbon emissions[8]. The use of coke[6], as a fuel and reductant in this process, is responsible for the rising CO_2 emissions from the steel industry as production continues to increase. Over 70% of global steel is produced through the BF-BOF process[6,8], a capital and emission intensive technology. Since decades, the iron

and steel manufacturers have called for decarbonization efforts. However, since the process technology of BF-BOFs is so heavily reliant on carbon chemistry[6], it is nearly impossible to divorce the use of carbon from conventional steel making. Thus, with stricter regulations to abide to the alarming environmental aspects[8–10], there is a key need for developing disruptive art technology, eliminating carbon. A number of alternative 'sustainable' technologies have been proposed and are being developed. The underlying principle of most of them being the use of an alternate reducing agent. Technologies such as Direct Reduced Iron (DRI) production using natural gas (reducing the use of carbon) or H_2 (eliminating carbon) and electrochemical pathways (electrons as the reducing agent) for iron production, e.g., alkaline electrowinning of iron ore[11] or molten oxide electrolysis[12], are being extensively studied and developed into pilot-scale facilities. However, these technologies face multiple techno-economic challenges in scaling up, as there is very little room for operational uncertainty and inefficiency[13]. The inability to match and surpass the stringent economics and scale of production of BF-BOFs[14] and the idea of premature retirement of these existing capital-intensive structures, restricts their widespread adoption.

Analyzing the carbon emissions at each step in the BF-BOF steel making route, one is quick to realize that the major burden of emissions occurs before the BOF. The coke ovens and BF account for ~88 % (of the 1.8-ton CO_2/ ton steel) of the total carbon emissions, with the BOF accounting for a minor amount of 0.2-ton CO_2/ ton steel (lower than an EAF). In fact, the important thing to note is that the highest value creation occurs in the BOF[15], by converting iron to steel (commodity product in demand), with unmatchable productivity and refining quality, before it is sent for continuous casting. Moreover, the presence of carbon in its feedstock (pig iron contains ~4 –5 % C) facilitates its autothermal operation, by the heat released by the oxidation of carbon and other impurities during refining[15]. The massive amounts of spontaneous heat generated also allows recycling of scrap (constitutes 30% of the feedstock)[15]. Thus, replacement of this classic autothermal reactor enabling sustainable value addition is highly disadvantageous to the steel industry.

One of the major challenges in the alternative routes suggested is that each of them results in pure iron production. Not only do they limit the utilization of the BOF to its complete potential but demand very high temperature processing conditions, beyond the

melting point of pure iron. Additionally, due to the absence of carbon, there is a minimal residual solubility of 3000 ppm of oxygen in the pure liquid iron[16], requiring further refining. Thus, there is a need for developing technologies which enable the production of molten iron to integrate it with the present BOFs to achieve their unsurpassed standards of refining and productivity. Based on the decreasing cost of electricity[14,17] and the foreseen availability of huge amount of clean electricity, thanks to the clean energy transition[18], it is advantageous to use an electrochemical route for steel production[14]. With high benchmarks set by the Al industry for producing all of the primary Al in use electrolytically, and evidence that electricity use can reduce energy consumption in metals production, electrolytic routes are gaining importance. Thus, this work proposes a novel electrolytic approach based on sulfide chemistry, molten sulfide electrolysis.

The approach involves electrolysis of FeS to produce sulfur at the anode and molten iron at the cathode. A graphite cathode enables molten iron production, making it a suitable feedstock for the BOF. The sulfur gas released at the anode is captured and condensed. FeS could be sourced from natural reserves of pyrite and chalcopyrite ($CuFeS_2$). The oil and gas industry is also a major producer of FeS, which usually occurs as an impurity in the source rocks for oil and natural gas. Value can be created from waste by utilizing this FeS directly. However, since ages, our primary source of iron has been iron oxide ores, usually hematite. Thus, to blend in the use of oxide ores in MSE, the approach involves a pre-treatment step of heating the iron oxide ore with sulfur gas, selectively sulfidising iron oxide to FeS while keeping the other impurities as oxides, facilitating easy physical separation (e.g., froth floatation) of the sulfide concentrate from the gangue. The sulfur gas released in the MSE can fulfill part of the sulfidation treatment requirements. Along with FeS formation, SO_2 gas is released. The non-ferrous industry has demonstrated efficient handling of the SO_2 gas by capturing it for sulfuric acid production[19], which can be used to generate electricity. Thus, this process forms a closed loop with no direct carbon emissions. The by-products released can be used to fulfill the internal demands of the process without any waste generation.

Depending on the size of the reactor, the MSE cell is expected to be self-heated due to the generation of heat within the electrolyte. This occurs because of the Joule effect, due to the inherent resistance of the electrolyte. The molten iron would be periodically tapped out

of the MSE reactor, while feeding the reactor with FeS, to maintain the composition of the electrolyte, thus operating in a semi-continuous manner. The cap of allowable electricity consumption for any alternative electrolytic process to match the present economics of steel production is about 3900 kWh/ ton steel[14]. A preliminary thermodynamic analysis shows that the energy consumption for the process, 1717 kWh/ ton Fe[xiv], not only lies within the maximum allowable range but is nearly 64% less than that of conventional steel making, and 52.8% less than molten oxide electrolysis[17]. Moreover, the low operating temperature range of around 1300◦ C, allows for better heat management and a refractory lifeline. Thus, the flowsheet for the proposed process is shown below in **Figure 6.1**

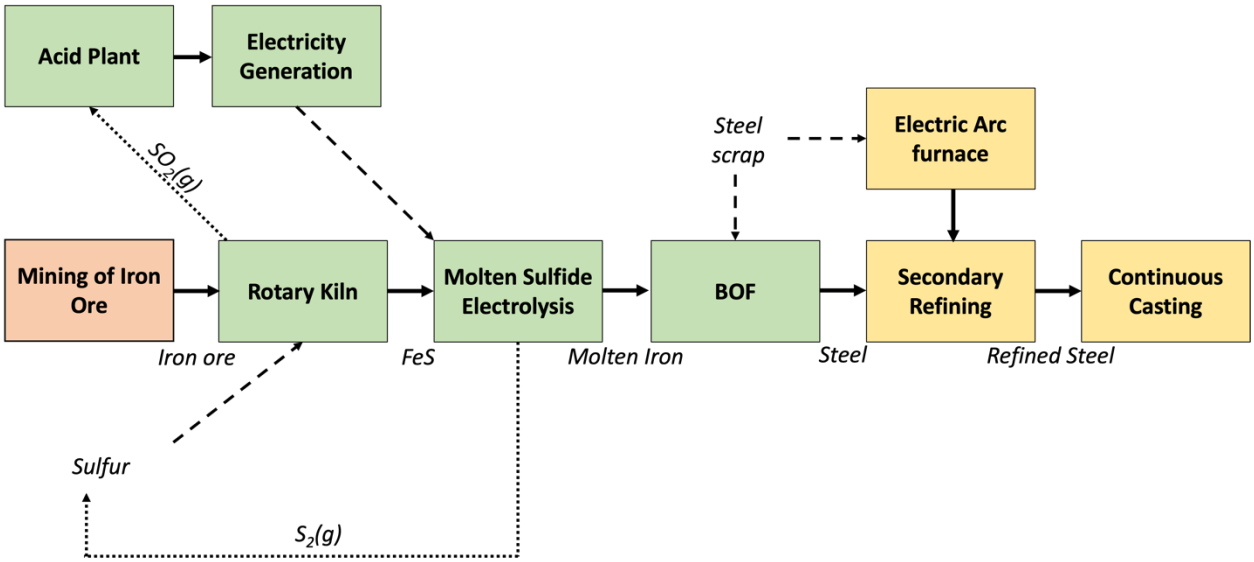

Figure 6.1 Flowsheet for steel production using MSE integrated with present steel making infrastructure

Adopting MSE for iron production can serve multiple advantages: elimination of direct carbon emissions, low energy consumption, and the potential to integrate well with the present BOF steel making. In comparison to other electrolytic methods, MSE exhibits a remarkable, greater than 95% anodic efficiency. One of the major reasons for this is the existence of Fe (+2) as the sole valence state as opposed to multiple valence states in oxides (Fe^{+2} and Fe^{+3}). In fact, the energy required for the sulfide reduction drops down by 1/3rd that of oxide reduction. Post sulfidation, the Fe^{+3} in the oxide gets converted to Fe^{+2} in the

[xiv] Per ton Fe (1.045-ton molten iron) calculation only to compare with pure Fe production calculation in MOE

sulfide. In this process, the reduction corresponding to **one** electron per Fe atom occurs in an exothermic spontaneous process.

Furthermore, the high solubility of FeS (10 wt.%) in the supporting electrolyte, high current density and generation of liquid product make it advantageous as compared to aqueous techniques allowing for higher space-time yield and productivity.

Thus, MSE offers many benefits compared to other electrochemical techniques. The process thus allows molten iron production at small scale facilities where excess pyrite is available or by treating the oxide ores with sulfur. Integrating the MSE cells into the existing steel making facilities allows benefitting from the unsurpassed productivity and refining capabilities of the BOF and continuous casting.

MSE relies on sulfur and other constituents of the supporting electrolyte (Ba and La). It is therefore important to ensure the sufficient availability of these elements to support the present scale of steel production. Speaking about sulfur, at present there are 600 million tons of world sediment sulfur reserves with more than 50% of the reserves in Iraq (Mishraq fields)[20]. Additionally, global reserves of sulfur in natural gas, crude oil, petroleum (recovered from oil refining), tar sands and metal sulfides including elemental sulfur in volcanic deposits totals about 5 billion tons[21], with the USA accounting for 20% of the world's total. This would also allow us to utilize the waste by-product (sour gas) of the oil and gas industry. Additionally, since the processing of petroleum or sulfide ores are not restricted to the location of the reserves, the sulfur production from these reserves can be spread globally. As of 2021, the global annual production of elemental sulfur[xv] was 80 million tons at a price of \$90/ ton (in 2020: \$25/ton)[21].

Evaluating the availability of the constituents of the supporting electrolyte BaS and La_2S_3: The process of sulfidation can be used to produce BaS and La_2S_3 from $BaSO_4$ (barite mineral) and La_2O_3 (23 wt.% of Bastnaesite mineral). In the event of using natural iron sulfide feedstocks, the sulfur generated in the MSE process could be used in the preparation of the supporting electrolyte. As of 2021, 7.3 million Mt of $BaSO_4$ [22] and 280,000 Mt of La_2O_3[23]

[xv] The sulfur production in China includes elemental sulfur recovered as a byproduct from natural gas and petroleum, sulfur content of sulfuric acid from pyrite and that generated as a by-product.

were produced annually. At lab scale, the production of kg scale of these compounds has already been demonstrated[24,25]. With over 740 million tons of identified resources of barite globally (2 billion tons in all categories), sold at $180/ton[22] and 120,000,000 Mt of Rare-earth oxide equivalent reserves[23], these elements face low supply risk as they are not vulnerable to any supply restriction, nor do they have any environmental implications in its production. Although, it has been assumed that the supporting electrolyte is entirely reused, a more detailed analysis is needed to realize how much (if any) of these constituents is 'lost' per ton of molten iron produced.

Thus, concluding by briefly summarizing the work described in each chapter.

Chapter 1 entails the importance of iron and steel and the current conventional route while highlighting its advantages and environmental challenges. It motivates the need for alternative sustainable steel making technologies using electricity to follow the strict regulations to handle the alarming levels of CO_2 emissions.

Chapter 2 reviews the literature about the existing alternatives for iron making while analyzing the pros and cons of each technology. It then sets the foundation for MSE, explaining the novel sulfide approach and how it has the potential to overcome those challenges.

Chapter 3 lays out the thermodynamic feasibility of the process through a detailed mass-energy balance. Energy balances for both pure liquid Fe as well as molten iron production at 1300° C and 1600° C to comparatively analyze the energy requirements for different final products. This concluded molten iron production at 1300° C was the most feasible in energy usage and technology integration.

In *chapter 4*, the experimental methodology is explained in detail for both the sulfidation treatment and the MSE trials.

And finally, *chapter 5* analyses the observations and discusses the results of successful demonstration of a high-carbon Fe alloy with an anodic efficiency greater than 95%.

6.2 Future Work

Based on the thermodynamic and experimental analysis of the results, MSE certainly proves to be a promising candidate for sustainable steel production. However, there is scope for future work to be done to enable its industrial feasibility and adoption.

Though the process demonstrated a successful electrolytic decomposition of FeS, the detailed mechanism involved in the electrochemical decomposition is yet to be studied. Thus, a comprehensive study of the relationship between the electrolyte conductivity and current efficiency needs to be done, both from a physical and chemical basis. This would enable to understand the effect of changing the proportion of the feedstock and optimizing the electrolyte composition to minimize electronic conductivity as well as maximize productivity. This would also include studying the physicochemical properties of the supporting electrolyte to get a better insight into the parameters controlling the mechanism. The use of a **reference electrode** is crucial to study individually the electrochemical activity at the anode and the cathode. This will also help in quantifying the overpotentials at the electrodes.

The study of varying electrolyte compositions was limited in this work due to the lack of a ternary phase diagram of BaS-La_2S_3-FeS. With the generation of this phase diagram, more regimes of operation can be explored. Further work would involve studying the effect of impurities and alloying additions (for example carbon) on the electrolytic product formed and efficiency. Additionally, there is scope in filling the current gap in the lack of thermodynamic data on the system (e.g. interaction parameters between the electrolyte species), to account for the solution effects.

The off-stoichiometry of the cell feedstock can be a factor influencing the cathodic efficiency. Thus, the feedstock preparation needs to be studied with respect to controlling the off-stoichiometry. Measures to increase the robustness of the system to varying feedstocks, such as off-stoichiometric FeS compounds, needs to be studied.

To get a better indication of the quality of the product formed, a scale-up version of these experiments needs to be done, to better study the following features:

1. Minimum size of the reactor and current required to ensure a self-heated cell
2. Use of a molten iron cathode
3. Measuring both the cathodic and anodic current efficiencies
4. Quality of the product in terms of carbon and sulfur content (in larger size samples)

Additionally, studying the kinetics of the sulfidation reaction and electrolysis was out of scope of this present work, but needs to be studied in detail in the future, e.g., a detailed thermodynamic model accounting for the diffusion effects. This will be needed to determine the required kinetic parameters in the scale-up version to ensure full conversion to sulfide and study the associated overpotentials in the MSE cell.

Future avenues also exist in the study of the effect of impurities in the feedstock in terms of the following:

1. Leveraging the reaction thermodynamics and kinetics to selectively sulfidise iron oxide from low-grade ores. Previous work by Marden and Stinn et al. have demonstrated the selective sulfidation of iron oxide from bauxite (other components included silicates, aluminates and titanium oxides)[26], however more work is needed to study how other impurities like silica, phosphorus, etc. can be managed.
2. Possibility of removing contaminants from scrap by sulfidation, especially potential to handle Cu impurities in steel scrap[24,27]

Based on the work of L. Rush et.al[28], it was concluded that with respect to cost and energy savings, MSE for Cu production was better than traditional copper smelting. Also, it was found that the heat generated in the system due to the ohmic drop, could be used to melt excess gangue and hence make use of low-grade ores. A similar detailed analysis of the Fe system is needed and hence holds scope for future work.

Based on the high current densities and low cell voltages recorded, MSE fits within the process space for economically producing commodity Fe. At a considerably basic and preliminary stage, based on the work of Stinn et. al, it can be demonstrated that high

temperature, high current density reactors tend to minimize cell capital costs[29]. However, a full-economic evaluation including the capital costs of an MSE facility entails opportunity for future work.

6.3 References

(1) Steel. *Wikipedia*; 2024.

(2) Media, C. N.; cnmAdmin2030. *6 Reasons Steel is One of the Most Used Metals Today*. Industry Today - Leader in Manufacturing & Industry News. https://industrytoday.com/6-reasons-steel-is-one-of-the-most-used-metals-today/ (accessed 2024-03-15).

(3) *World Steel in Figures 2022*. worldsteel.org. https://worldsteel.org/steel-topics/statistics/world-steel-in-figures-2022/ (accessed 2024-02-23).

(4) *This is how much metal we mine every year | World Economic Forum*. https://www.weforum.org/agenda/2021/10/all-tonnes-metals-ores-mined-in-one-year/ (accessed 2024-03-15).

(5) World Steel Association. Energy Use in the Steel Industry, 2021. https://worldsteel.org/wp-content/uploads/Fact-sheet-energy-in-the-steel-industry-2021-1.pdf.

(6) World Steel Association. Fact Sheet | Raw Materials in the Steel Industry, 2023. https://worldsteel.org/wp-content/uploads/Fact-sheet-raw-materials-2023.pdf.

(7) *Climate change policy paper - worldsteel.org*. https://worldsteel.org/publications/policy-papers/climate-change-policy-paper/ (accessed 2024-03-15).

(8) *Iron and Steel Technology Roadmap – Analysis*. IEA. https://www.iea.org/reports/iron-and-steel-technology-roadmap (accessed 2024-03-15).

(9) *Net Zero by 2050 – Analysis*. IEA. https://www.iea.org/reports/net-zero-by-2050 (accessed 2024-03-15).

(10) *The Paris Agreement | UNFCCC*. https://unfccc.int/process-and-meetings/the-paris-agreement (accessed 2024-03-15).

(11) Allanore, A.; Lavelaine, H.; Valentin, G.; Birat, J. P.; Lapicque, F. Electrodeposition of Metal Iron from Dissolved Species in Alkaline Media. *J. Electrochem. Soc.* **2007**, *154* (12), E187. https://doi.org/10.1149/1.2790285.

(12) Wang, D.; Gmitter, A.; Sadoway, D. Production of Oxygen Gas and Liquid Metal by Electrochemical Decomposition of Molten Iron Oxide. *Journal of The Electrochemical Society* **2011**, *158*. https://doi.org/10.1149/1.3560477.

(13) Allanore, A. Features and Challenges of Molten Oxide Electrolytes for Metal Extraction. *Journal of the Electrochemical Society* **2014**, *162*, E13–E22. https://doi.org/10.1149/2.0451501jes.

(14) Allanore, A. Electrochemical Engineering for Commodity Metals Extraction. *Electrochem. Soc. Interface* **2017**, *26* (2), 63. https://doi.org/10.1149/2.F05172if.

(15) *Basic Oxygen Furnace Steelmaking*. https://www.steel-technology.com/articles/oxygenfurnace (accessed 2024-03-15).

(16) Allanore, A.; Yin, L.; Sadoway, D. A New Anode Material for Oxygen Evolution in Molten Oxide Electrolysis. *Nature* **2013**, *497*, 353–356. https://doi.org/10.1038/nature12134.

(17) Allanore, A. Contribution of Electricity to Materials Processing: Historical and Current Perspectives. *JOM* **2013**, *65* (2), 130–135. https://doi.org/10.1007/s11837-012-0538-3.

(18) *Climate-Smart Mining: Minerals for Climate Action*. World Bank. https://www.worldbank.org/en/topic/extractiveindustries/brief/climate-smart-mining-minerals-for-climate-action (accessed 2024-03-15).

(19) Landolt, C. A.; Dutton, A.; Edwards, J. D.; McDonald, R. N. SO2 Abatement, Energy Conservation, and Productivity at Copper Cliff. *JOM* **1992**, *44* (9), 50–55. https://doi.org/10.1007/BF03222328.

(20) *Iraq has more than half of the world's sulfur reserves, Official - Shafaq News*. https://shafaq.com/en/Economy/Iraq-has-more-than-half-of-the-world-s-sulfur-reserves-Official (accessed 2024-03-18).

(21) Apodaca, L. E. Sulfur; Minerals Commodity Summaries; U.S. Geological Survey: Reston, VA, USA, 2022. https://pubs.usgs.gov/periodicals/mcs2022/mcs2022-sulfur.pdf.

(22) McRae, M. Barite, Minerals Commodity Summaries; U.S. Geological Survey, Reston, VA, USA, 2022. https://pubs.usgs.gov/periodicals/mcs2022/mcs2022-barite.pdf.

(23) Cordier, D. Rare Earths; Minerals Commodity Summaries; U.S. Geological Survey: Reston, VA, USA, 2022. https://pubs.usgs.gov/periodicals/mcs2022/mcs2022-rare-earths.pdf.

(24) Daehn, K.; Stinn, C.; Rush, L.; Benderly-Kremen, E.; Wagner, M. E.; Boury, C.; Chmielowiec, B.; Gutierrez, C.; Allanore, A. Liquid Copper and Iron Production from Chalcopyrite, in the Absence of Oxygen. *Metals* **2022**, *12*, 1440. https://doi.org/10.3390/met12091440.

(25) Daehn, K.; Benderly-Kremen, E.; Yagi, R.; Stinn, C.; Boury, C.; Rush, L.; Wagner, M. E.; Allanore, A. Scaling up Molten Sulfide Electrolysis for Liquid Copper Production from Chalcopyrite. *Proceedings of the Copper 2022 Conference, Santiago, Chile* **2022**.

(26) Stinn, C.; Marden, L.; Benderly-Kremen, E.; Gilstrap, W.; Allanore, A. Bauxite Processing Via Sulfide Chemistry. In *Light Metals 2024*; Wagstaff, S., Ed.; Springer Nature Switzerland: Cham, 2024; pp 64–73. https://doi.org/10.1007/978-3-031-50308-5_8.

(27) Daehn, K. E.; Serrenho, A. C.; Allwood, J. Finding the Most Efficient Way to Remove Residual Copper from Steel Scrap. *Metall Mater Trans B* **2019**, *50* (3), 1225–1240. https://doi.org/10.1007/s11663-019-01537-9.

(28) Rush, L. Integrative Approach to Metal Extraction and Electrification, 2021. https://hdl.handle.net/1721.1/140135.

(29) Stinn, C.; Allanore, A. Estimating the Capital Costs of Electrowinning Processes. *Electrochem. Soc. Interface* **2020**, *29* (2), 44. https://doi.org/10.1149/2.F06202IF.

Appendix 1

Preliminary sulfidation experiment

A 1.1 Methodology

The sulfidation of pure Fe_2O_3 was performed in the same way as described in chapter 4, **section 4.1**. The oxide powder was filled in a graphite crucible (packed bed reactor conditions). The following were the operating conditions:

- ✓ Temperature: 900 °C
- ✓ Particle size: 106 -150 microns
- ✓ Bed height of the reactant: ~ 1cm
- ✓ Duration at reaction temperature: 1 hour (60 mins)

A 1.2 Observations and results

Upon completion of the experiment, it was observed that complete conversion had not occurred. Upon dividing the pellet in 4 approximately equal halves for analysis (magnetic test, Optical & SEM, XRD), the cross section clearly showed 2 phases: a shiny phase at the outer surface of the pellet, identified as the sulfide phase, and the other at the core, which looked dark black. After carefully separating the powders from one divided part, magnetic testing was done. The black powder at the core of the bed was magnetic in nature whereas the shiny grey powder at the surface was non-magnetic. Thermodynamic analysis using the predominance diagrams shows that Fe_3O_4 is an intermediate in the sulfidation of Fe_2O_3 to FeS. Hence, this compound was most likely expected to be magnetite (Fe_3O_4).

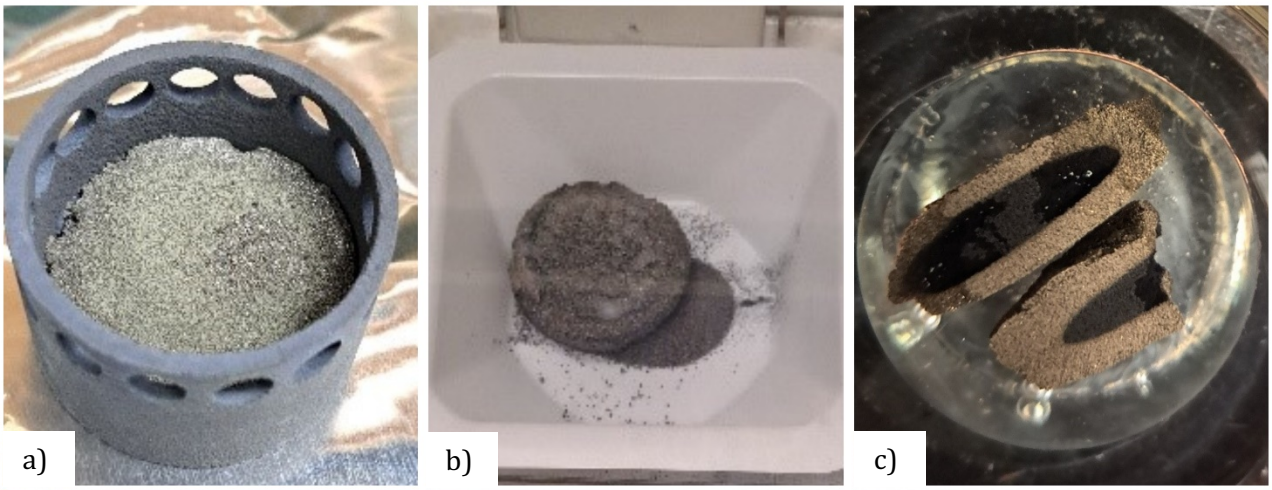

Figure A 1.1 (a) Reaction product in the crucible (b) Reaction product as a pellet (c) Cross-section showing 2 phases

Based on the mass calculations and comparison with stoichiometric calculations (as shown in **section 5.1.1**, chapter 5), only a 27.5 wt.% conversion of the oxide to sulfide to occurred, remaining was a partial conversion to magnetite. To investigate the reasons, the reaction product was mounted in epoxy and polished to be observed under the optical microscope and SEM. Optical micrographs are shown in **Figure A 1.2**.

The polished sample was also observed under the SEM and EDS analysis was performed over it. The SEM micrograph at 50 X magnification is shown below in **Figure A 1.3**. An element intensity map (see **Figure A 1.4**) clearly shows the reaction front separating the oxide and sulfide phases. The reason for the incomplete reaction was as slightly lower temperature leading to slower kinetics of the reactions. The reaction kinetics were further affected due to sintering of the particles on the surface (sulfide particle) which created mass transport issues for the sulfur to penetrate to the core and react.

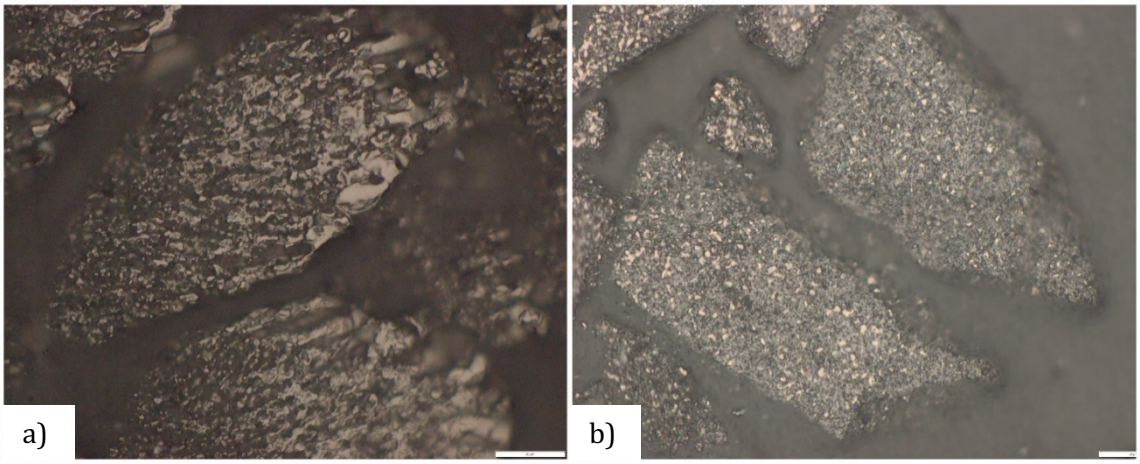

Figure A 1.2 Optical micrographs at 50 X (a) Shiny particle or FeS (b) Dull black particle (magnetite)

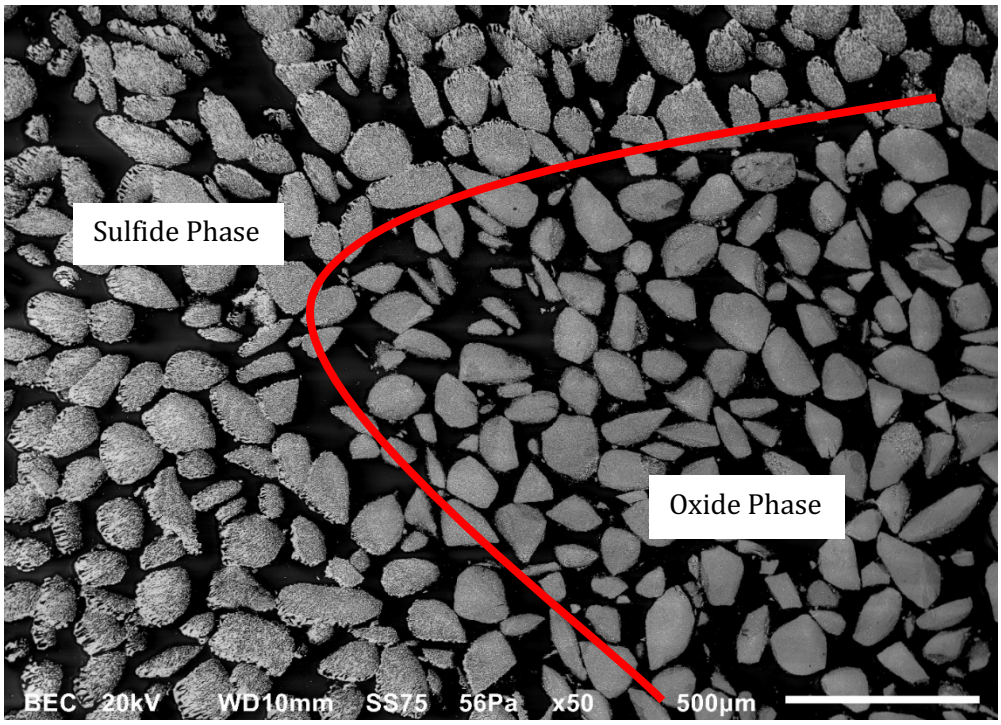

Figure A 1.3 SEM Backscattered image at 50 X clearly showing the reaction front drawn in red

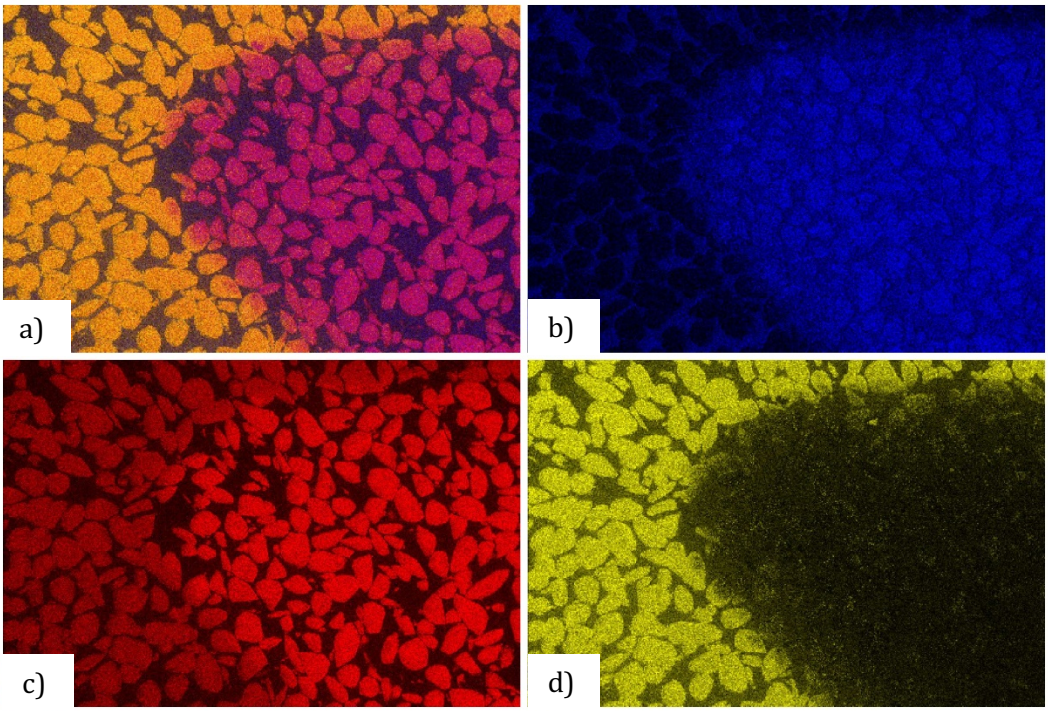

Figure A 1.4 Element Intensity Map demarcating the oxide and sulfide regions (a) Full SEM image with the following color code: Fe, S, O (b) Oxygen (c) Fe (d) Sulfur

The composition of the phases was further confirmed by XRD analysis as shown in **Figure A 1.5**. The product consisted mostly of FeS and Fe_3O_4, with some minute residual quantities of Fe_2O_3.

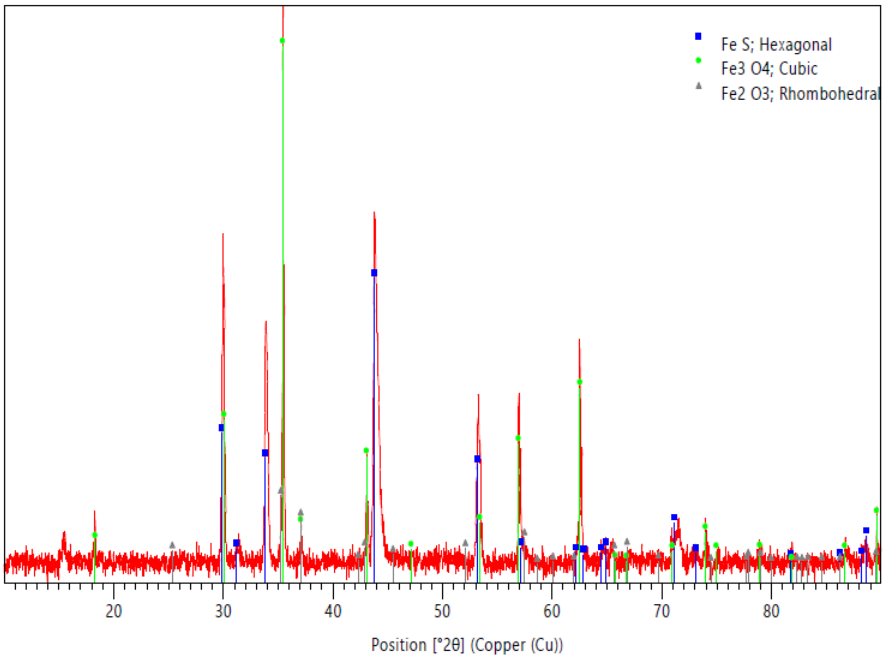

Figure A 1.5 XRD analysis of the reaction product

Appendix 2

Alternate reduction methods - Vacuum thermal decomposition treatments

A 2.1 Methodology

Another possible method of reduction of sulfide to produce metal was also attempted, Vacuum Thermal Treatment (VTT). This reduction technique involved a spontaneous thermal decomposition of the iron sulfide to metal in a vacuum atmosphere (10^{-3} atm). The governing reaction is as follows:

$$FeS\ (l) + x\ C\ (from\ the\ graphite\ crucible) \rightarrow Fe - x\%\ C\ (l) + \frac{1}{2}S_2(g) \quad \text{(A 2.1)}$$

At atmospheric pressure (1 atm), FeS spontaneously reduces to Fe metal at an extremely high temperature (~2890°C). With a reduced pressure environment however, the

temperature at which the thermal decomposition is lower, and comes in the range of the melting point of Fe. Thus, at a vacuum of 10^{-3} atm, FeS thermally decomposes at a temperature closer to 1700°C. With increasing activity of carbon in the Fe melt, the temperature of thermal decomposition comes further down to less than 1650°C.

Thus, to confirm this theoretical background, the vacuum thermal treatment was performed at a temperature of 1500°C and a vacuum of 10^{-3} atm. The experimental setup included a graphite crucible weighting 23.703 g, loaded with 5 g of pure lab grade FeS, surrounded by a graphite susceptor. The graphite susceptor is used to avoid direct coupling with the sample or crucible. This is because during thermal decomposition, the composition of the material inside the crucible will change as the reaction progresses, resulting in a change in the heating profile. Thus, to maintain homogeneity in temperature, a susceptor is used to prevent changes in the sample material composition from affecting the heating of the remaining material. A type-B (Pt-Rh alloy) thermocouple was used to measure the temperature in-situ. The thermocouple was inserted from the bottom part of the furnace.

Figure A 2.1 Experimental setup of a vacuum thermal decomposition

The assembly of the crucible and the susceptor was raised to the hot zone (area around the heating coil) using a 2-inch diameter alumina support tube. Once the assembly

was arranged and the system was set under vacuum, the furnace was turned on. Dark glasses were used to observe the inside of the crucible in-situ experiment.

Unlike the Mellen tube furnace, the heating profile is steeper in the induction furnace. The reaction temperature/peak temperature was reached in 15 mins, the sample was held at this temperature for 30 mins and then quenched.

A.2.2 Post experiment observations

Once the sample was quenched and the tube was recovered, a sulfur deposit was observed on the walls of the quartz tube as shown in **Figure A 2.2 (a)**. Additionally, $S_2(g)$ odor was detected when the tube was removed. Inside the crucible, a metallic solid pellet (see **Figure A 2.2 (b)**) was observed along with some small nodules which visually appeared as metallic in nature.

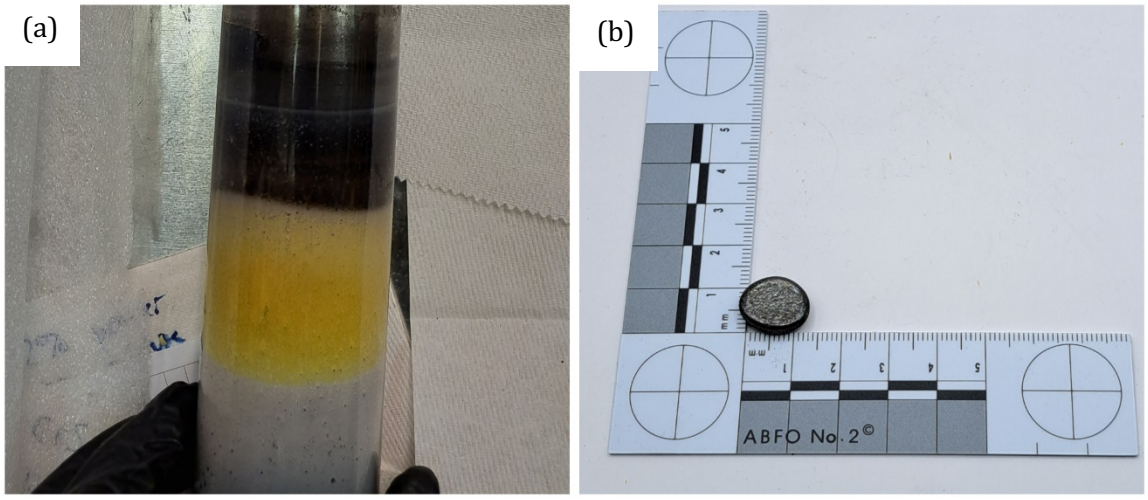

Figure A 2.2 (a) Image of sulfur condensate on the quartz tube (b)Metallic pellet formed as a result of VTT

To observe a cross-section (shown in **Figure A 2.3**), the solid pellet was sectioned using an in-house wire EDM. During the sectioning, one of the pieces started cracking, especially when water was being used during the wire EDM cutting process. This may be due

to the sulfur inclusions which upon reacting with water lead to the release of H_2S (g), causing the observed cracks.

Figure A 2.3 Cross-section of the metallic pellet formed depicting (a) cracks on the surface mostly due to gas escaping (b)Fe-FeS phases on the cross-section

One of the sectioned pieces was mounted in epoxy and polished to be observed under the SEM (see **Figure A 2.4**). The elemental composition was ascertained using the EDS analysis. Volumetrically 2 phases were observed: Phase 1 was 95 – 98% Fe with S inclusions (< 40% by volume) and phase 2 was FeS with Fe dendrites observed.

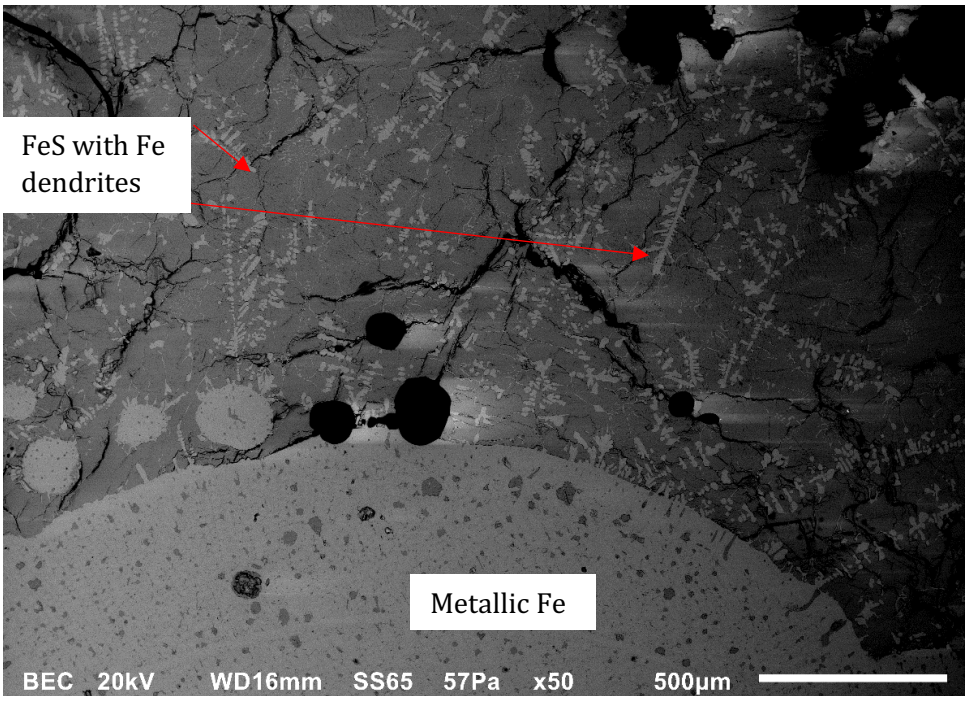

Figure A 2.4 SEM micrograph of the cross-section of the pellet depicting the phase boundary between metallic Fe and FeS

It was concluded that due to temperature and the time of the reaction (time the furnace was maintained at the peak temperature) being insufficient (slightly lower) for thermal decomposition, the reaction did not reach completion.

Hence, a second experiment was performed at a higher temperature of 1700°C and the sample was held at the reaction temperature for 30 mins. Nearly complete conversion of the sulfide to the metal occurred. The metallic pellet obtained is shown in **Figure A 2.5.** Results of the optical microscopy are shown below in **Figure A 2.6**.

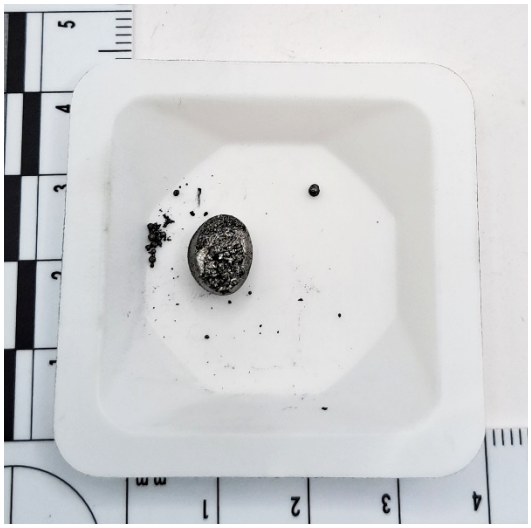

Figure A 2.5 Fe -C alloy metallic pellet produced as a result of the second VTT experiment

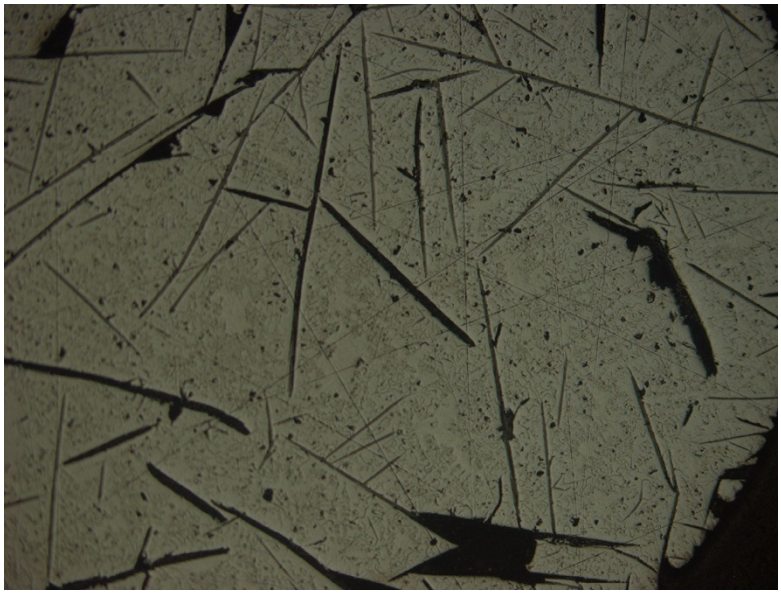

Figure A 2.6 Optical Micrograph of the Fe -C alloy metallic pellet produced as a result of the second VTT experiment

Although, the vacuum thermal treatments are a possible alternative and the success of this approach is demonstrated in the reduction of the sulfide to form a Fe-C alloy, it is not a cost-effective approach, especially for not-special purpose steels (e.g. molten iron production for further steel making). Vacuum treatments practiced in industry today are expensive, adding to the operating costs and hence are only practiced for ultra-refined steels or ultra-high-quality steels (with very low carbon and other special alloys). For a comparison, cost of hot-rolled coil is $700 /ton, whereas that for interstitial-free steel (only includes an extra step of vacuum degassing) is $1000 /ton. Due to the stringent compositional requirements, these alloys are usually sold at very high prices due to the capital expenses incurred to achieve those compositions. Hence, molten sulfide electrolysis was seen to as a cost-effective approach, comparatively low temperature 1350 °C, as opposed to the at least 1700°C in VTTs.

Appendix 3

Initial molten sulfide electrolysis experiment

A 3.1 Methodology

The molten sulfide electrolysis experiments were performed as described in **section 4. 2**, **chapter 4**. Initial conditions of operations included very high power of the lamps resulting in partial thermal decomposition of the FeS, resulting in very high mass loss (see **Figure A 3.3**). This mass loss was proportional to the duration of the thermal decomposition experiment, with the highest mass loss of ~ 5 mg occurring at about 40 mins.

A 3.2 Observations and results

A cross-section of the electrolyte sample after a thermal decomposition test was analyzed under the SEM. It revealed a phase segregation occurring at the bottom of the electrolyte in contact with the cathode. A region of Ba rich sulfide, depleted in both Fe and La, was observed at the bottom whereas the central portion (bulk of the electrolyte) was observed to be a mixture of the 3 sulfides. A similar phenomenon occurred upon electrolysis as well, resulting in low faradaic efficiencies, in the range of 50 – 60%. This was attributed to the Ba rich phase segregating at the bottom, preventing further Fe deposition from occurring (see **Figure A 3.1**).

Several trials of the modified compositions (using the electrolyte composition observed in the center as the starting composition assuming it is the stable phase at high temperature) and cathode designs were investigated. From these experiments, it was concluded that the phase segregation that was observed was a result of the heat distribution from the graphite cathode which remained hot (stored heat) for some time after the lamps were switched off. Thus, due the graphite cathode having a fairly high specific heat capacity, even after switching off the lamps, the cross-section did not represent a quenched sample.

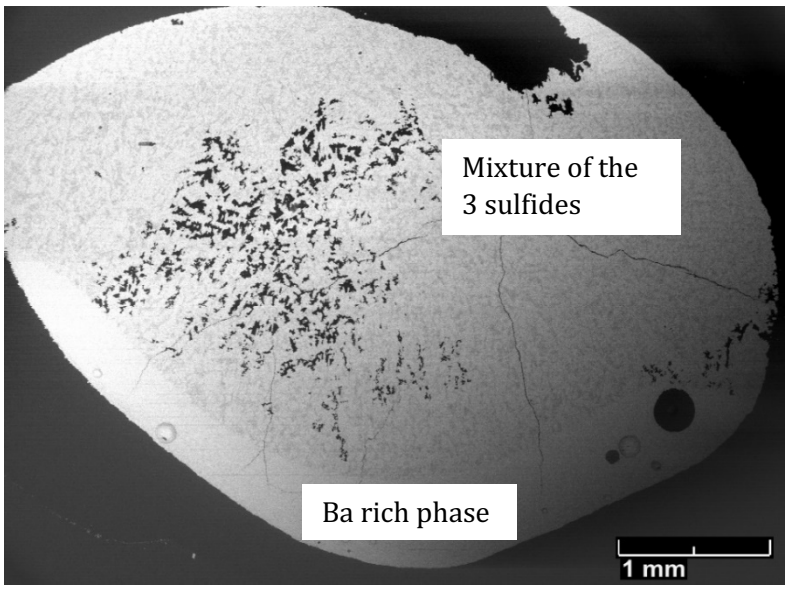

Figure A 3.1 Electrolyte cross-section (SEM) after a thermal decomposition test, showing a phase segregation

Some phase segregation occurred later as a result of the bottom of the electrolyte still being at a high temperature than the surface or the top. This was concluded from the shape of the Ba rich region following the shape of the cathode divet, suggesting a change of cathode design being a solution. **Figure A 3.2** shows the optical micrograph of the electrolyte cross-section showing phase segregation.

The issue with the initial design (deeper divet) was that the graphite prevented complete heat from the lamps from reaching the part of the electrolyte submerged within the cathode, leading to uneven heating of the electrolyte. This was because one part was directly exposed to the lamps getting more heat, the other submerged within getting less heat.

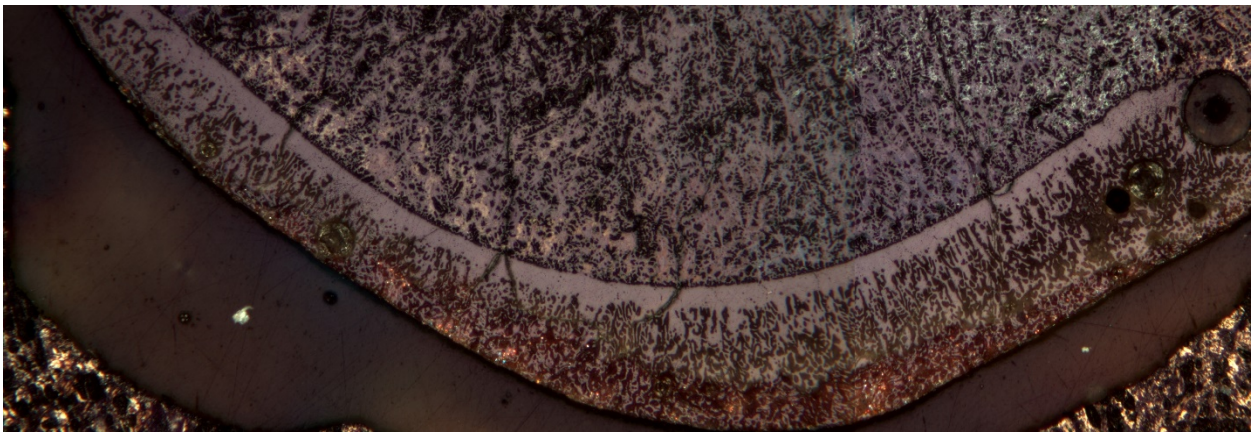

Figure A 3.2 Optical micrograph of electrolyte cross-section (5 X) after a thermal decomposition test, showing a phase segregation

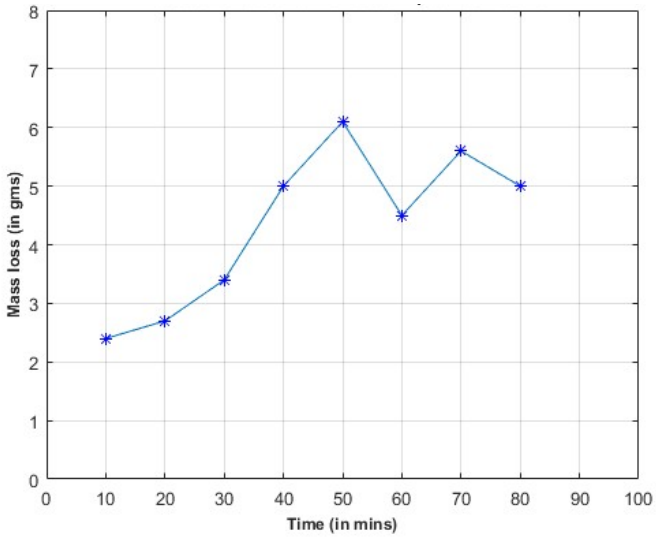

Figure A 3.3 Results of the thermal decomposition test carried out recording mass loss versus time

Similar phase segregation was not observed while making the pre-melts. The reason was uniform heating on all sides of the electrolyte (powder was inside the hole drilled in the pucker). Hence two designs were tested – one deeper divet (no electrolyte surface directly exposed to the lamps – required higher power to melt, also restricted in-situ observation due to the cathode blocking the electrolyte from being viewed. The shallow divet design showed better results and solved the phase segregation issue (see **Figure A 3.4**).

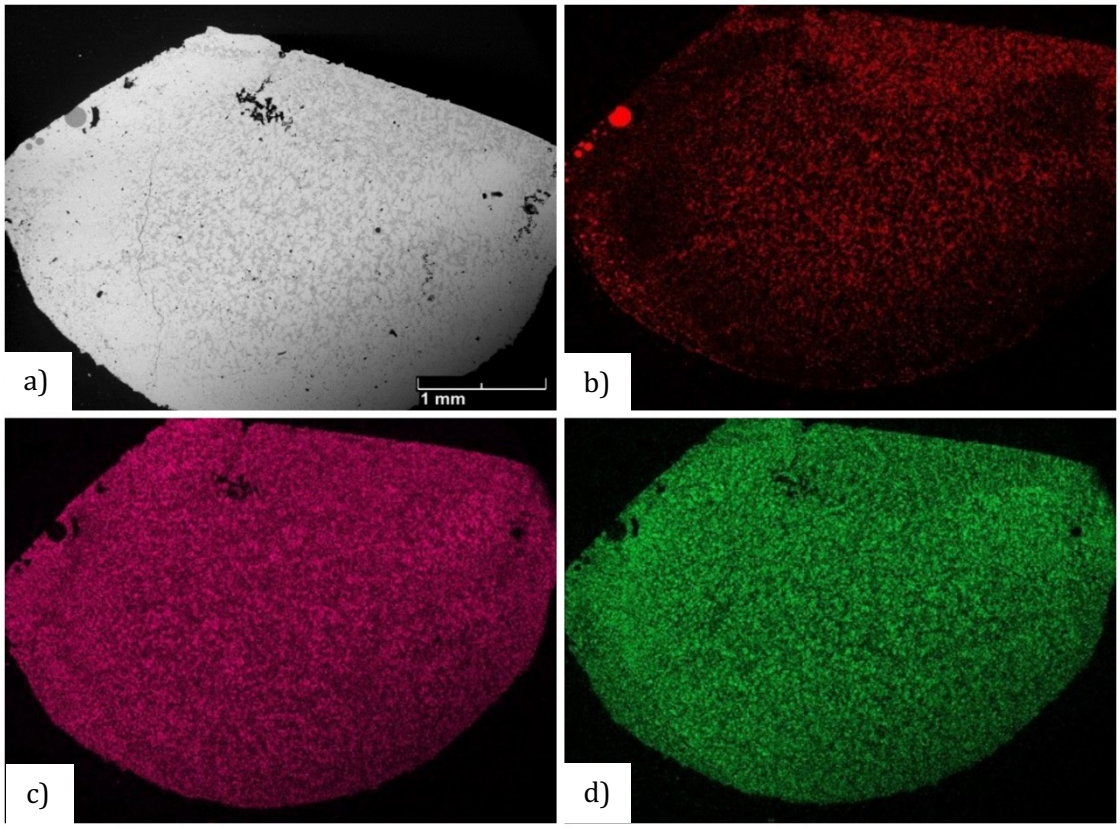

Figure A 3.4 Cross section of the electrolyte after electrolysis, showing a phase segregation as well as Fe deposition (a) SEM image (b) Fe (c) Ba (d) La

The Fe deposits were observed in the Ba rich phase region after electrolysis. The formation of perfect spherical Fe deposits indicated the formation of pure Fe liquid. This suggested the operating temperature to be higher than the melting point of Fe.

Thus, the cathode design was modified to reduce the contact area of the electrolyte and the cathode. This was done by reducing the depth of the divet, allowing the full electrolyte to being exposed to the lamps and avoiding the higher retention of heat by the cathode. Thus, after these modifications, no phase segregation layer was observed, confirming the above

theory. Temperature measurements were done in the thermal imaging furnace to reduce the lamp power and operate in the temperature range of the cast iron production. Moreover, the electrolyte was melting at a lower power (4% as compared to 18% previously) since a higher surface area (almost full electrolyte) was subjected to the radiation from the lamps and was absorbing more energy, eliminating the possibility of thermal decomposition.

Appendix 4

COMSOL Multiphysics Impedance modelling

The experimental electrochemical setup was modelled on COMSOL Multiphysics software using the electric currents physics model. Using this model, the resistance of the system was evaluated and compared to that obtained experimentally (see **section 5.2.3.1.1** for results). The details of the model are presented below.

A 4.1 Methodology

To build a model on COMSOL, a physics interface needs to be applied. For this case, it is the **Electric currents interface.** Ohm's law is used to solve a current conservation equation, where the electric potential is the dependent variable. The current conservation (assuming steady state conditions) uses the continuity equation for the electric potential:

$$\nabla . \boldsymbol{J} = Q_j$$

$$\boldsymbol{J} = \sigma \boldsymbol{E} + \boldsymbol{J_e}$$

$$\boldsymbol{E} = -\nabla V$$

Where σ is the electrical conductivity (S/m), $\boldsymbol{E}$ is the electric field, V is the electric potential, $\boldsymbol{J}$ is the current density, $\boldsymbol{J}_e$is an externally generated current density(A/m^2) and Q_j is an external current source (A/m^3). The important thing to note is that the model assumes isothermal conditions and calculates for a stationary system (variables independent of time).

A. 4.1.1 Boundary Conditions

After defining the boundary conditions as follows:

Initial voltage: 0 V

Ground node: Implements a zero potential at the boundary.

Terminal node: The boundary condition that provides external circuit connections.

I_o = Current applied

The other default added boundary conditions included electric insulation at the boundaries (restricting the flow of electric current into the boundary) and axial symmetry, which ensured the set boundary conditions applied to all boundaries along the symmetric axis.

A.4.1.2 Geometry

After the physics interface was chosen and the boundary conditions were set, a geometry was made emulating the actual electrochemical system.

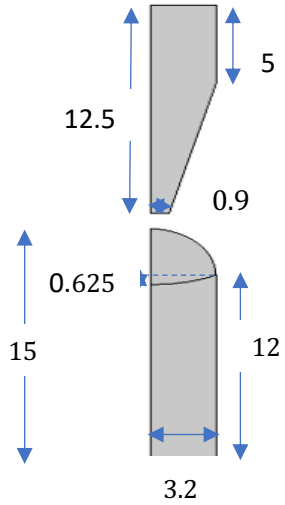

Figure A 4.1 Schematic of the model with dimensions (not to scale)

The geometry was constructed assuming the system to be symmetric about the central axis. **Figure A 4.1** depicts the geometry along with the dimensions in mm.

A.4.1.3 Material Properties

Later, the components constructed on the geometrical model were assigned material properties as follows (shown in **Table A 4.1** and **A 4.2)**:

Electrodes (Anode and cathode): Graphite

Property	Value
Electrical conductivity	100000 S/m
Density	1744 kg/m^3
Thermal conductivity	42.10 W/m. K)

Table A 4.1 Material properties of the graphite electrodes

Electrolyte

Property	Value
Electrical conductivity	29.069 S/m
Density	4.525 kg/m^3
Thermal conductivity	3960.12× 10^{-8} W/ (m.K)
Heat Capacity at constant pressure	40.33 J/(kg.)
Electrolyte conductivity	0 S/m

Table A 4.2 Material properties of the electrolyte

Using an extremely fine element size for the mesh, the model was solved to evaluate the resistance values at varying distances between the electrodes.

A 4.2 Observations and results

A similar trend as observed experimentally was seen through the values calculated using COMSOL. As the distance between the electrodes increased, the resistance values were also observed to increase. As can be seen in the curve in **Figure A 4.2**, the experimental values and those obtained from the model are in good agreement, especially at smaller electrode distances. As the distance increases, a deviation between the values is observed. This can plausibly be justified due to a temperature variation in the experimental setup as the distance between the electrodes is changed. This could occur due to the system shifting slightly away from the hot zone (one cubic centimeter volume at the focus), resulting in a temperature drop, hence experimentally recorded resistance values corresponding to a lower temperature. However, the COMSOL calculated values used isothermal conditions.

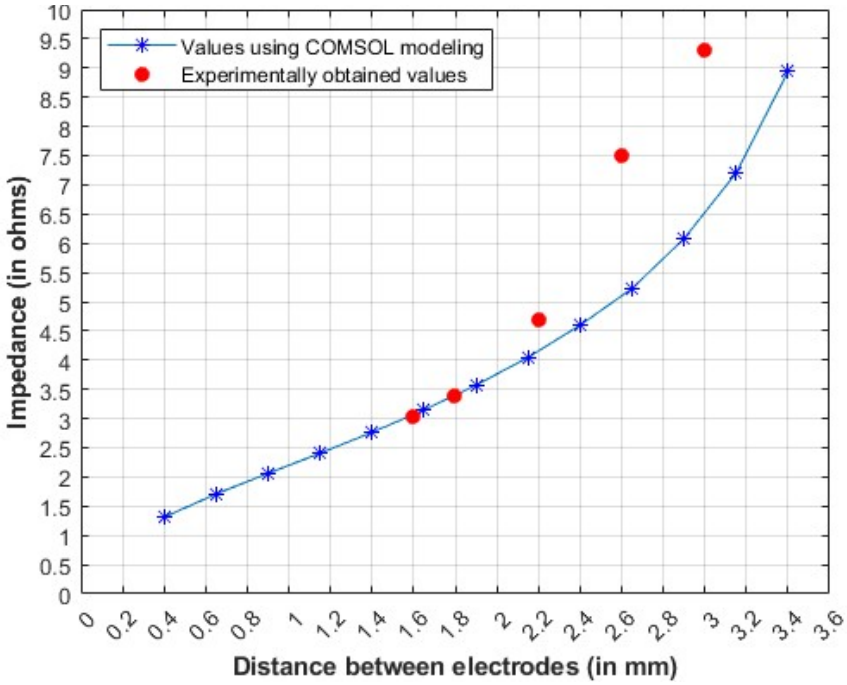

Figure A 4.2 Plot depicting the experimentally obtained resistance values and those obtained using the COMSOL model

©2024 Kimaya P. Suryarao. All Rights Reserved.
The author hereby grants to MIT a nonexclusive, worldwide, irrevocable, royalty-free license to exercise any and all rights under copyright, including to reproduce, preserve, distribute and publicly display copies of the thesis, or release the thesis under an open-access license.